

Functional normalizing flow for statistical inverse problems of partial differential equations

Yang Zhao^a, Haoyu Lu^a, Junxiong Jia^{a,*}, Tao Zhou^b

^a*School of Mathematics and Statistics, Xi'an Jiaotong University, Xi'an, Shaanxi 710049, China*

^b*Academy of Mathematics and Systems Sciences, Chinese Academy of Sciences, Beijing, 100190, China*

Abstract

Inverse problems of partial differential equations are ubiquitous across various scientific disciplines and can be formulated as statistical inference problems using Bayes' theorem. To address large-scale problems, it is crucial to develop discretization-invariant algorithms, which can be achieved by formulating methods directly in infinite-dimensional space. We propose a novel normalizing flow based infinite-dimensional variational inference method (NF-iVI) to extract posterior information efficiently. Specifically, by introducing well-defined transformations, the prior in Bayes' formula is transformed into post-transformed measures that approximate the true posterior. To circumvent the issue of mutually singular probability measures, we formulate general conditions for the employed transformations. As guiding principles, these conditions yield four concrete transformations. Additionally, to minimize computational demands, we have developed a conditional normalizing flow variant, termed CNF-iVI, which is adept at processing measurement data of varying dimensions while requiring minimal computational resources. We apply the proposed algorithms to two typical inverse problems governed by a simple smooth equation and the steady-state Darcy flow equation. Numerical results confirm our theoretical findings, illustrate the efficiency of our algorithms, and verify the discretization-invariant property.

Keywords: inverse problems, infinite-dimensional variational inference, functional normalizing flow, Bayesian analysis for functions, partial differential equations.

1. Introduction

Driven by their widespread applications in seismic exploration, radar imaging, and other fields, inverse problems involving partial differential equations (PDEs) have witnessed significant advancements in recent decades [2, 28]. As computational power continues to grow, researchers are increasingly focused on not only obtaining estimated solutions but also conducting statistical analyses to quantify uncertainties, which is crucial for tasks such as artifact detection [50]. The Bayesian inverse approach offers a robust framework for addressing inverse problems within the context of PDEs by transforming them into statistical inference problems, thereby enabling the analysis of parameter uncertainties [17].

Typically, inverse problems of PDEs are posed in infinite-dimensional spaces [28], which presents challenges for applying well-established finite-dimensional Bayesian inference techniques [5, 27]. To bridge this gap, two predominant strategies have been developed:

*Corresponding author: Junxiong Jia (jjx323@xjtu.edu.cn)

- Discretize-then-Bayesianize: PDEs are initially discretized to approximate the original problem in some finite-dimensional space, and the reduced, approximated problem is then solved using Bayes' method [27].
- Bayesianize-then-discretize: Bayes' formula and algorithms are initially constructed in infinite-dimensional space, and after the infinite-dimensional algorithm is built, some finite-dimensional approximation is carried out [17].

Both approaches offer distinct advantages and disadvantages. The *Discretize-then-Bayesianize* approach allows us to employ all the Bayesian inference methods developed in the statistical literature [12, 27] to solve the inverse problems. However, due to the infinite-dimensional nature of the original problems, two critical challenges arise:

- Model consistency: Finite-dimensional models, such as those representing prior probability measures, exhibit distinct properties compared to their infinite-dimensional counterparts. A notable example is the total variation prior, which has been extensively studied in [16, 32].
- Algorithm applicability: To preserve the intrinsic structure of original infinite-dimensional problems, algorithms initially designed for finite-dimensional spaces must be carefully adapted to the infinite-dimensional setting. This reformulation ensures consistent algorithmic behavior across various discretizations, as demonstrated in [15, 22–24, 44].

To address these challenges, the *Bayesianize-then-discretize* approach has attracted significant attention from researchers in recent years [9, 14, 17].

A primary challenge in Bayesian inference is the efficient extraction of posterior information. From the *Bayesianize-then-discretize* perspective, an infinite-dimensional Markov chain Monte Carlo (MCMC) algorithm known as preconditioned Crank-Nicolson (pCN) has been proposed and analyzed in detail [15, 37]. This algorithm maintains consistent sampling efficiency across different discretizations. In addition to the pCN algorithm, other types of infinite-dimensional sampling algorithms have been proposed, such as the infinite-dimensional sequential Monte Carlo algorithm [4] and the infinite-dimensional importance sampling algorithm [1]. To enhance sampling efficiency, infinite-dimensional MCMC algorithms with gradient and geometric informative proposals have been developed. Examples include the infinite-dimensional Metropolis-adjusted Langevin algorithm [10] and the geometric pCN algorithm [3]. Although these algorithms possess mesh independence properties, they are challenging to apply to large-scale inverse problems of PDEs, such as full waveform inversion [34].

In the finite-dimensional setting, variational inference (VI) methods have been extensively studied in machine learning to mitigate the computational demands of Markov chain Monte Carlo (MCMC) sampling algorithms [49]. For example, a mean-field assumption based VI approach was employed to solve finite-dimensional inverse problems with hyper-parameters in prior and noise distributions [20, 25, 26]. Projected Stein variational gradient descent methods were constructed to solve inverse problems with low-intrinsic dimensions [13], and normalizing flow in Euclidean space have been extensively studied as a means to approximate target posterior distributions by transforming simple distributions [35, 40, 46].

Here, we briefly outline the key distinctions between MCMC sampling and variational inference (see [6] for details). While MCMC methods typically require higher computational resources, they guarantee asymptotically exact samples from the target distribution [42]. In contrast, variational

inference seeks an approximate distribution that is computationally tractable, leading to significant computational gains despite some loss of accuracy compared to MCMC. Variational inference’s compatibility with optimization techniques such as stochastic gradient descent and distributed optimization [31, 41, 48] makes it well-suited for large datasets and rapid model exploration. MCMC excels in scenarios with smaller datasets where precise sampling is prioritized. Another critical factor influencing the choice between MCMC and variational inference is the geometry of the posterior distribution. For instance, mixture models often exhibit multiple modes corresponding to different label permutations. In such cases, Gibbs sampling excels due to its ability to efficiently explore these modes [5]. However, when Gibbs sampling is not feasible, variational inference can outperform general MCMC methods, such as Hamiltonian Monte Carlo, even for smaller datasets [30].

In contrast to the extensive research on finite-dimensional problems, the application of VI methods to infinite-dimensional settings remains relatively unexplored. Generally speaking, there are two main research directions for VI methods in infinite-dimensional settings:

- **Parameterize measures directly:** This involves directly parameterizing the approximate measure and optimizing these parameters to approximate the posterior. For instance, when restricting approximations to Gaussian measures, a novel Robbins-Monro algorithm was developed using a calculus-of-variations perspective [38, 39]. Under the classical mean-field assumption, a general VI framework within separable Hilbert spaces was recently proposed [23, 24, 44].
- **Parameterize transformation:** By parameterizing a transformation, a simple measure can be mapped into a more complex measure to approximate the posterior. Optimization of these transformation parameters drives the approximation process. For example, the infinite-dimensional Stein variational gradient descent introduced in [21] represents a function space particle optimization method with rigorous mathematical underpinnings in separable Hilbert spaces.

In this work, we focus on defining normalizing flow in infinite-dimensional spaces, aligning with the second research direction. Specifically, we derive general transformation forms capable of mapping simple measures to complex distributions within the function space. When constructing the normalizing flows based infinite-dimensional variational inference (NF-iVI) algorithm, it is crucial to ensure that the post-transformed measure is absolutely continuous with respect to the prior measure. Otherwise, the Radon-Nikodym (RN) derivative of the post-transformed measure with respect to the prior measure will become meaningless, which would contradict the entire theoretical framework of the infinite-dimensional variational inference algorithm [23, 39]. Leveraging the properties of Gaussian measures [7], we develop a rigorous theoretical framework for transformations within functional normalizing flow. By formulating specific conditions, our approach guarantees the equivalence between the post-transformed and pre-transformed measures (detailed in Subsection 2.2), ensuring the model’s well-definedness in function space.

In addition, we have devised a strategy to alleviate the computational demands of NF-iVI. Variational inference algorithms require analyzing the Kullback-Leibler (KL) divergence between the approximate and target posterior measures, which involves taking an expectation over the approximate measure. This typically necessitates computationally intensive Monte Carlo estimation. In our algorithm, the derivative of the KL divergence with respect to the parameters of the approximate measure must be calculated at each iteration. This necessitates computing the KL

divergence and its gradient at each iteration, significantly increasing computational cost. While the NF-iVI algorithm offers advantages over traditional methods like pCN, it still presents considerable computational challenges (see Section 4 for details). We observe that for a fixed inverse problem model, distinct measurement data induce distinct posterior distributions, necessitating computationally intensive model retraining for each new set of measurement data. To enhance the computational efficiency of our algorithm when processing new measurement data, we propose to incorporate a conditional component into functional normalizing flow. By introducing measurement data as a conditional input, we enable the model to adapt to different measurement data without requiring extensive retraining. When the conditional network is trained, we can directly obtain an acceptable estimate of the posterior for any measurement data. We refer to this approach **conditional normalizing flows based infinite-dimensional variational inference (CNF-iVI)**. Furthermore, if we want to obtain a more accurate approximation, we can consider further training for specific measurement data based on the pre-trained conditional functional normalizing flow.

In summary, this work mainly contains four contributions:

- We introduce an infinite-dimensional model called functional normalizing flow, which is capable of transforming a simple measure into a complex approximation of the target measure. To ensure the validity of these transformations, we establish a rigorous theoretical framework that guarantees the equivalence between the transformed and pre-transformed measures.
- We introduce two linear flows: functional Householder flow and functional projected transformation flow, and two nonlinear flows: functional planar flow and functional Sylvester flow, as exact examples. Rigorous proofs confirm that all four proposed models satisfy the conditions of the theoretical framework we established for functional normalizing flow.
- We have developed a model called conditional functional normalizing flow by incorporating a conditional component. This component enables the direct entry of measurement data of any length, yielding an acceptable posterior estimate. To achieve greater accuracy, the model can be further refined through targeted training on specific measurement data.
- We have applied NF-iVI and CNF-iVI to typical linear and nonlinear inverse problems, specifically elliptic inverse problems and steady-state Darcy flow inverse permeability estimations, thereby validating their efficiency.

The outline of this paper is as follows: In Section 2, we briefly introduce the theoretical framework and algorithmic process of NF-iVI. In Subsection 2.1, we present the infinite-dimensional Bayesian theory proposed in [38, 39] and provide a brief overview of infinite-dimensional variational inference algorithms. In Subsection 2.2, we introduce the NF-iVI algorithm in function spaces. In Subsections 2.3 and 2.4, we provide four examples of functional normalizing flow. In Subsection 2.5, we prove the discretization-invariance of the proposed functional normalizing flows. In Section 3, based on NF-iVI, we introduce the algorithmic process of CNF-iVI. In Subsection 3.1, we construct an additional conditional input component, allowing the parameters of functional normalizing flow to be determined by observational information. We also present the detailed training procedure for CNF-iVI. In Subsection 3.2, we describe a method to improve the results of conditional functional normalizing flow. In Sections 4 and 5, we apply the algorithms to two typical inverse problems, verifying the feasibility of both the NF-iVI and CNF-iVI algorithms. Additionally, in each numerical simulation, we demonstrate the mesh independence as expected for the

Bayesianize-then-discretize approach. In Section 6, we summarize our achievements, acknowledge some deficiencies, and explore further research directions.

2. Functional Normalizing Flow

In this section, we establish the theoretical framework of functional normalizing flow. To circumvent the obstacle posed by the singularity of measures in infinite-dimensional spaces, we introduce a novel theoretical framework. Building upon this foundation, four specific flow models are proposed and shown to satisfy the established theoretical criteria.

2.1. Bayesian Approach and Variational Inference

In this subsection, we introduce the foundational concepts of infinite-dimensional Bayesian inverse problems and the underlying principles of infinite-dimensional variational inference.

Let \mathcal{H}_u , \mathcal{H}_w be separable Hilbert spaces representing the parameter space and solution space, respectively, and N_d be a positive integer. Denote that $\mathcal{N}(u, \mathcal{C})$ is a Gaussian measure with mean u and covariance operator \mathcal{C} . The inverse problem can be described as follow:

$$\mathbf{d} = \mathcal{S}\mathcal{G}(u) + \boldsymbol{\epsilon}, \quad (2.1)$$

where $\mathbf{d} \in \mathbb{R}^{N_d}$ is the measurement data, $u \in \mathcal{H}_u$ is the interested parameter, \mathcal{G} is the PDE solving operator from \mathcal{H}_u to \mathcal{H}_w , \mathcal{S} is the observation operator from \mathcal{H}_w to \mathbb{R}^{N_d} , and $\boldsymbol{\epsilon}$ is a Gaussian random vector with zero mean and covariance matrix $\boldsymbol{\Gamma}_{\text{noise}} := \tau^{-1}\mathbf{I}$ (τ is a fixed positive number, and \mathbf{I} denotes the N_d -dimensional identity matrix), which means

$$\boldsymbol{\epsilon} \sim \mathcal{N}(0, \boldsymbol{\Gamma}_{\text{noise}}). \quad (2.2)$$

Based on the framework of infinite-dimensional Bayesian inference [47], we are able to preserve the fundamental Bayes' formula for the inverse problem:

$$\frac{d\mu}{d\mu_0}(u) = \frac{1}{Z_\mu} \exp(-\Phi(u)), \quad (2.3)$$

where $\Phi : \mathcal{H}_u \rightarrow \mathbb{R}$ is defined as

$$\Phi(u) = \frac{1}{2} \|\mathbf{d} - \mathcal{S}\mathcal{G}(u)\|_{\boldsymbol{\Gamma}_{\text{noise}}}^2, \quad (2.4)$$

where $\|\cdot\|_{\boldsymbol{\Gamma}_{\text{noise}}} := \|\boldsymbol{\Gamma}_{\text{noise}}^{-1/2} \cdot\|$ and Z_μ is a positive finite constant given by

$$Z_\mu = \int_{\mathcal{H}_u} \exp(-\Phi(u)) \mu_0(du).$$

Directly extracting quantitative information from the posterior distribution in Bayes' formula (2.3) is computationally prohibitive [15]. To circumvent this challenge, variational inference approximates the intractable posterior with a more tractable measure. We select a set of measures $\mathcal{M}(\mathcal{H}_u)$ on space \mathcal{H}_u as the approximating measure set. To ensure that the Radon-Nikodym (RN) derivative between measures is meaningful, we require that any measure within $\mathcal{M}(\mathcal{H}_u)$ is equivalent to the prior measure μ_0 [39]. For any $\nu \in \mathcal{M}(\mathcal{H}_u)$, the KL divergence between ν and posterior μ is given by

$$D_{\text{KL}}(\nu||\mu) = \int_{\mathcal{H}_u} \ln \left(\frac{d\nu}{d\mu}(u) \right) \nu(dx) = \int_{\mathcal{H}_u} \ln \left(\frac{d\nu}{d\mu_0}(u) \right) - \ln \left(\frac{d\mu}{d\mu_0}(u) \right) \nu(du).$$

The primary objective of variational inference is to identify a measure, denoted ν^* , that minimizes the KL divergence between an approximate distribution ν and the target posterior distribution μ :

$$\nu^* = \arg \min_{\nu \in \mathcal{M}(\mathcal{H}_u)} D_{\text{KL}}(\nu || \mu). \quad (2.5)$$

When solving the minimization problem (2.5), it will usually be convenient to parameterize the set $\mathcal{M}(\mathcal{H}_u)$ in a suitable way: Overly intricate measures can hinder optimization, while overly simplistic ones may compromise approximate accuracy. To address this trade-off, [38, 39] employed carefully designed Gaussian measures, whereas [23, 24, 44] opted for the mean-field approach.

2.2. Normalizing Flow in Function Space

In this paper, we draw inspiration from the ideas presented in Euclidean space [40]. A series of parametric transformations will be applied to a simple measure to generate a flexible set of complex measures. This collection of measures forms the approximating measure set $\mathcal{M}(\mathcal{H}_u)$ for variational inference as outlined in (2.5). Consistent with normalizing flow in Euclidean space [35, 40, 46], we refer to this set of models as functional normalizing flow.

The core of the model consists of two components: the pre-transformed measure and the transformations. The pre-transformed measure should be simple enough to enable efficient sampling, while the transformations must be flexible enough to convert this simple measure into a complex one that accurately approximates the target measure. We select the prior μ_0 of Bayes' formula (2.3) as the pre-transformed measure. The transformations are a series of parameterized operators, denoted as $f_{\theta_n}^{(n)}$, mapping from \mathcal{H}_u to \mathcal{H}_u . Here, $n = 1, 2, \dots, N$, and $\theta_n \in \Theta_n$ represents the parameters of $f_{\theta_n}^{(n)}$. The space Θ_n is a parameter space, whose specific form depends on the parameterization of $f_{\theta_n}^{(n)}$. For instance, in the context of functional planar flow illustrated in Subsection 2.4, the parameter space Θ_n is defined as follows:

$$\Theta_n = \{(w_n, u_n, b_n) \in \mathcal{H} \times \mathcal{H} \times \mathbb{R} \mid \langle u_n, w_n \rangle_{\mathcal{H}_u} > -1\},$$

where \mathcal{H} is the Cameron-Martin space of the prior μ_0 . Let $\theta = \{\theta_1, \theta_2, \dots, \theta_N\}$ denote the collection of parameters. The final complex measures are constructed by composing a series of transformations, which convert the pre-transformed measure into the post-transformed one. We write that

$$f_{\theta}(u) = f_{\theta_N}^{(N)} \circ \dots \circ f_{\theta_2}^{(2)} \circ f_{\theta_1}^{(1)}(u),$$

and denote $u_{\theta}^N := f_{\theta}(u_0)$ where u_0 is a sample from μ_0 . Then u_{θ}^N will be a sample from the measure $\mu_{f_{\theta}} = \mu_0 \circ f_{\theta}^{-1}$, where $\mu_0 \circ f_{\theta}^{-1}$ is the law of f_{θ} with respect to μ_0 [7]. By varying the parameters θ , the transformed measures $\mu_{f_{\theta}}$ form a set of measures on \mathcal{H}_u , denoted by

$$\mathcal{M}(\mathcal{H}_u) = \{\mu_{f_{\theta}} \mid \theta \in \Theta\},$$

where $\Theta = \Theta_1 \times \Theta_2 \times \dots \times \Theta_N$ denotes the space of all possible values of θ . We let the set $\mathcal{M}(\mathcal{H}_u)$ constitute the approximating measures for the variational inference defined in (2.5).

Functional normalizing flow gives us a way to specify the approximate measures required for variational inference. However, since all the measures in $\mathcal{M}(\mathcal{H}_u)$ should be equivalent to the prior μ_0 [39], the choice of the parametric transformations $\{f_{\theta_n}^{(n)}\}_{n=1}^N$ may pose significant challenges. The measures within the infinite-dimensional function space are inherently prone to be singular with each others. To elucidate this concept, we present two pertinent examples:

Example 2.1. Let μ_0 be a Gaussian measure on $L^2(\mathbb{R})$, and let $\mathcal{H}(\mu_0)$ be its Cameron-Martin space. Assume $m \notin \mathcal{H}(\mu_0)$, define $f_m(u) = u + m$, and let $\mu_m = \mu_0 \circ f_m^{-1}$. We know that μ_m is singular with respect to μ_0 .

Example 2.2. Let μ_0 be a Gaussian measure on $L^2(\mathbb{R})$, $f_2(u) = 2u$, and $\mu_2 = \mu_0 \circ f_2^{-1}$, then we know that μ_2 is singular with respect to μ_0 .

It is worth noting that although the transformations f_m and f_2 are quite simple, they will convert μ_0 into measures that are singular with respect to μ_0 , which contradicts the theoretical framework of infinite-dimensional variational inference. Consequently, the judicious selection of transformations is paramount for normalizing flow in function space, requiring both model flexibility and the preservation of measure equivalence. Here, we introduce a general theorem characterizing the transformations of functional normalizing flow. Assuming $\mathcal{F}_{\theta_n}^{(n)}$ is an operator mapping \mathcal{H}_u to itself for $n = 1, 2, \dots, N$, parameterized by θ_n , $D\mathcal{F}_{\theta_n}^{(n)}(u)$ represents the Fréchet derivative of $\mathcal{F}_{\theta_n}^{(n)}$, and $\theta = \{\theta_1, \theta_2, \dots, \theta_N\}$. We define transformations as follows:

$$f_{\theta_n}^{(n)}(u) = u + \mathcal{F}_{\theta_n}^{(n)}(u). \quad (2.6)$$

We now present the following theorem, which establishes conditions ensuring the equivalence of measures before and after the transformations defined in equation (2.6).

Theorem 2.3. Let \mathcal{H}_u be a separable Hilbert space equipped with the Gaussian measure $\mu_0 = \mathcal{N}(0, \mathcal{C})$, and $\mathcal{H} = \mathcal{H}(\mu_0)$ be the Cameron-Martin space of the measure μ_0 . For each $n = 1, 2, \dots, N$, let $f_{\theta_n}^{(n)}(u) = u + \mathcal{F}_{\theta_n}^{(n)}(u)$, where $\mathcal{F}_{\theta_n}^{(n)}$ is an operator from \mathcal{H}_u to \mathcal{H}_u . The composite transformation f_θ is given by $f_\theta(u) = f_{\theta_N}^{(N)} \circ f_{\theta_{N-1}}^{(N-1)} \circ \dots \circ f_{\theta_1}^{(1)}(u)$, and μ_{f_θ} denotes its corresponding push-forward measure by $\mu_{f_\theta} = \mu_0 \circ f_\theta^{-1}$. Assuming the following conditions hold for all $n = 1, 2, \dots, N$ and any value of θ_n :

- The space $\text{Im}(\mathcal{F}_{\theta_n}^{(n)}) \subset \mathcal{H}$, where $\text{Im}(\mathcal{F}_{\theta_n}^{(n)})$ denotes the image of $\mathcal{F}_{\theta_n}^{(n)}$.
- The operator $\mathcal{F}_{\theta_n}^{(n)}$ is a finite rank operator.
- For any $u \in \mathcal{H}_u$, all point spectrum of $D\mathcal{F}_{\theta_n}^{(n)}(u)$ are not in $(-\infty, -1]$.

Then we will know that μ_{f_θ} is equivalent with μ_0 (denoted by $\mu_{f_\theta} \sim \mu_0$).

Theorem 2.3 establishes the equivalence between transformed measures and the prior μ_0 . Consequently, the collection of transformed measures, denoted $\mathcal{M}(\mathcal{H}_u)$, constitutes a suitable set of approximating measures for variational inference.

Analyzing the KL divergence between the approximate measure μ_{f_θ} and the posterior μ necessitates the RN derivative of the transformed measure μ_{f_θ} with respect to the prior μ_0 . We present a theorem that provides an expression for this derivative.

Theorem 2.4. Let \mathcal{H}_u be a separable Hilbert space equipped with the Gaussian measure $\mu_0 = \mathcal{N}(0, \mathcal{C})$, and $\mathcal{H} = \mathcal{H}(\mu_0)$ be the Cameron-Martin space of the measure μ_0 . For each $n = 1, 2, \dots, N$, let $f_{\theta_n}^{(n)}(u) = u + \mathcal{F}_{\theta_n}^{(n)}(u)$, where $\mathcal{F}_{\theta_n}^{(n)}$ is an operator from \mathcal{H}_u to \mathcal{H}_u . The composite transformation f_θ is given by $f_\theta(u) = f_{\theta_N}^{(N)} \circ f_{\theta_{N-1}}^{(N-1)} \circ \dots \circ f_{\theta_1}^{(1)}(u)$, and μ_{f_θ} denotes its corresponding push-forward measure by $\mu_{f_\theta} = \mu_0 \circ f_\theta^{-1}$. Assuming the following conditions hold for all $n = 1, 2, \dots, N$ and any value of θ_n :

- The space $\text{Im}(\mathcal{F}_{\theta_n}^{(n)}) \subset \mathcal{H}$, where $\text{Im}(\mathcal{F}_{\theta_n}^{(n)})$ denotes the image of $\mathcal{F}_{\theta_n}^{(n)}$.
- The operator $\mathcal{F}_{\theta_n}^{(n)}$ is a finite rank operator.
- The operator $f_{\theta_n}^{(n)}$ is bijective.
- For any $u \in \mathcal{H}_u$, all point spectrum of $D\mathcal{F}_{\theta_n}^{(n)}(u)$ are not in $(-\infty, -1]$.

Then the RN derivative of μ_{f_θ} with respect to μ_0 is given by:

$$\frac{d\mu_{f_\theta}}{d\mu_0}(f_\theta(u)) = \prod_{n=1}^N \left| \det_1(Df_{\theta_n}^{(n)}(u_{n-1})) \right|^{-1} \exp \left(\frac{1}{2} \langle f_\theta(u) - u, f_\theta(u) - u \rangle_{\mathcal{H}} + \langle u, u - f_\theta(u) \rangle_{\mathcal{H}} \right),$$

where $u_n = f_{\theta_n}^{(n)} \circ f_{\theta_{n-1}}^{(n-1)} \circ \dots \circ f_{\theta_1}^{(1)}(u)$ for each $n = 1, 2, \dots, N$, and $\det_1(Df_{\theta_n}^{(n)}(u_{n-1}))$ is the Fredholm-Carleman determinant [7] of the linear operator $Df_{\theta_n}^{(n)}(u_{n-1})$ (A rigorous definition can be found in the Appendix).

Leveraging Theorem 2.4, we can compute the necessary KL divergence

$$\begin{aligned} D_{\text{KL}}(\mu_{f_\theta} \|\mu) &= \int_{\mathcal{H}_u} \ln \left(\frac{d\mu_{f_\theta}}{d\mu}(u) \right) d\mu_{f_\theta}(u) \\ &= \int_{\mathcal{H}_u} \ln \left(\frac{d\mu_{f_\theta}}{d\mu_0}(u) \right) d\mu_{f_\theta}(u) - \int_{\mathcal{H}_u} \ln \left(\frac{d\mu}{d\mu_0}(u) \right) d\mu_{f_\theta}(u) \\ &= E_{\mu_{f_\theta}} \ln \left(\frac{d\mu_{f_\theta}}{d\mu_0}(u) \right) - E_{\mu_{f_\theta}} \ln \left(\frac{d\mu}{d\mu_0}(u) \right), \end{aligned}$$

where $E_{\mu_{f_\theta}}$ and E_{μ_0} denote the expectation with respect to μ_{f_θ} and μ_0 , respectively. Furthermore,

$$\begin{aligned} E_{\mu_{f_\theta}} \ln \left(\frac{d\mu_{f_\theta}}{d\mu_0}(u) \right) &= E_{\mu_0} \ln \left(\frac{d\mu_{f_\theta}}{d\mu_0}(f_\theta(u)) \right) \\ &= E_{\mu_0} \ln \left(\prod_{n=1}^N \left| \det_1(Df_{\theta_n}^{(n)}(u_{n-1})) \right|^{-1} \exp \left(\frac{1}{2} \langle f_\theta(u) - u, f_\theta(u) - u \rangle_{\mathcal{H}} + \langle u, u - f_\theta(u) \rangle_{\mathcal{H}} \right) \right) \\ &= E_{\mu_0} \left(- \sum_{n=1}^N \ln \left(\left| \det_1(Df_{\theta_n}^{(n)}(u_{n-1})) \right| \right) + \frac{1}{2} \langle f_\theta(u) - u, f_\theta(u) - u \rangle_{\mathcal{H}} + \langle u, u - f_\theta(u) \rangle_{\mathcal{H}} \right). \end{aligned}$$

Consequently, the optimization problem (2.5) can be reformulated as follows:

$$\theta^* = \arg \min_{\theta \in \Theta} D_{\text{KL}}(\mu_{f_\theta} \|\mu).$$

Monte Carlo sampling allows us to estimate the KL divergence, which we can use as a loss function to optimize the transformation parameters θ . The full details of the algorithm are presented in Algorithm 1. The estimated gradient of θ_k in Algorithm 1 can be computed by the preconditioned stochastic gradient-based optimization methods such as RMSprop (Root Mean Square Propagation), AdaGrad (Adaptive Gradient), and Adam (Adaptive Moment Estimation). In this article, we adopt the Adam optimizer, with implementation details provided in Section 4.

Algorithm 1 Functional Normalizing Flow

- 1: Initialize the hyperparameter λ to λ_0 , set the sampling size to N , the iterative number to K , and the learning rate schedule to α_k . Then, initialize the iteration counter k to 0;
 - 2: **repeat**
 - 3: Sampling N functions $\{u_i\}_{i=1}^N$ from prior μ_0 ;
 - 4: Update the parameters $\theta_{k+1} = \theta_k - \alpha_k \nabla_{\theta_k} L(\theta_k)$ with
$$\nabla_{\theta_k} L(\theta_k) = \nabla_{\theta_k} D_{\text{KL}}(\mu_{f_{\theta_k}} || \mu) \approx \frac{1}{N} \sum_{i=1}^N \nabla_{\theta_k} \ln \left(\frac{d\mu_{f_{\theta_k}}}{d\mu_0}(f_{\theta_k}(u_i)) \right) - \frac{1}{N} \sum_{i=1}^N \nabla_{\theta_k} \ln \left(\frac{d\mu}{d\mu_0}(f_{\theta_k}(u_i)) \right).$$
Variants of stochastic gradient-based optimization method can be employed in this step;
 - 5: $k = k + 1$;
 - 6: **until** $k = K$.
 - 7: Return the final result $\theta = \theta_K$.
-

2.3. Linear Transformation

Subsection 2.2 presents a general theoretical framework that outlines the conditions for flow models in function space to be well-defined. In this subsection, we introduce two specific linear flow models and provide rigorous proofs that they satisfy these theoretical conditions. Theorem 2.4 requires $f_{\theta_n}^{(n)}$ to be bijective for all n and θ_n . To ensure this property for linear flow, Lemma 2.1 is introduced.

Lemma 2.1. Let \mathcal{H}_u be a separable Hilbert space, $f_{\theta_n}^{(n)} : \mathcal{H}_u \rightarrow \mathcal{H}_u$, and $f_{\theta_n}^{(n)}(u) = u + \mathcal{F}_{\theta_n}^{(n)}(u)$, where $\mathcal{F}_{\theta_n}^{(n)}$ is a bounded linear operator. Assuming the following conditions hold for all $n = 1, 2, \dots, N$ and any value of θ_n :

- The operator $\mathcal{F}_{\theta_n}^{(n)}$ is a finite rank operator.
- For any $u \in \mathcal{H}_u$, all point spectrum of $D\mathcal{F}_{\theta_n}^{(n)}(u)$ are not in $(-\infty, -1]$.

Then the operator $f_{\theta_n}^{(n)}$ is bijective.

2.3.1. Functional Householder Flow

The first model, termed functional Householder flow, is a generalization of the Householder flow in Euclidean space [35, 45]. Each layer of functional Householder flow employs the following transformation:

$$f_{\theta_n}^{(n)}(u) = u - 0.5v_n(\langle v_n, u \rangle_{\mathcal{H}_u} + b_n),$$

where $v_n \in \mathcal{H}_u$, $b_n \in \mathbb{R}$, and the parameters set is given by $\theta_n = \{v_n, b_n\}$. We can ensure that the model meets the conditions in Theorem 2.4 by setting some restrictions.

Theorem 2.5. Let \mathcal{H}_u be a separable Hilbert space equipped with the Gaussian measure $\mu_0 = \mathcal{N}(0, \mathcal{C})$, and $\mathcal{H} = \mathcal{H}(\mu_0)$ be the Cameron-Martin space of the measure μ_0 . For each $n = 1, 2, \dots, N$, let $f_{\theta_n}^{(n)}(u) = u - 0.5v_n(\langle v_n, u \rangle_{\mathcal{H}_u} + b_n)$, where $\mathcal{F}_{\theta_n}^{(n)}$ is an operator from \mathcal{H}_u to \mathcal{H}_u and $\theta_n = \{v_n, b_n\}$ be its parameters. The composite transformation f_{θ} is given by $f_{\theta}(u) = f_{\theta_N}^{(N)} \circ f_{\theta_{N-1}}^{(N-1)} \circ \dots \circ f_{\theta_1}^{(1)}(u)$, and $\mu_{f_{\theta}}$ denotes its corresponding push-forward measure, given by $\mu_{f_{\theta}} = \mu_0 \circ f_{\theta}^{-1}$. Assuming the following conditions hold for all $n = 1, 2, \dots, N$ and any value of θ_n :

- $v_n \in \mathcal{H}$.

- $\langle v_n, v_n \rangle_{\mathcal{H}_u} = 1$.

Then we have $\mu_{f_\theta} \sim \mu$ and

$$\frac{d\mu_{f_\theta}}{d\mu_0}(f_\theta(u)) = \prod_{n=1}^N \left| \det_1(Df_{\theta_n}^{(n)}(u_{n-1})) \right|^{-1} \exp \left(\frac{1}{2} \langle f_\theta(u) - u, f_\theta(u) - u \rangle_{\mathcal{H}} + \langle u, u - f_\theta(u) \rangle_{\mathcal{H}} \right),$$

where $u_n = f_{\theta_n}^{(n)} \circ f_{\theta_{n-1}}^{(n-1)} \circ \dots \circ f_{\theta_1}^{(1)}(u)$ for each $n = 1, 2, \dots, N$.

The parameters $\{v_n\}_{n=1}^N$ of the flow model, being functions themselves, require an efficient parameterization. This is essential not only for computational efficiency but also for ensuring compliance with the constraints outlined in the theorem. A novel parameterization method for the flow model is proposed here. We denote $\{\phi_i\}_{i=1}^M$ as the first M eigenvectors of the prior covariance operator. The parameterization process for v_n involves two steps. Firstly, an auxiliary vector \hat{v}_n is introduced and parameterized as

$$\hat{v}_n = \sum_{i=1}^M \alpha_i^n \phi_i. \quad (2.7)$$

Secondly, to ensure that the normalization is met, that is, $\langle v_n, v_n \rangle_{\mathcal{H}_u} = 1$, we parameterize v_n using \hat{v}_n as shown in equation (2.7):

$$v_n = \frac{\hat{v}_n}{\|\hat{v}_n\|_{\mathcal{H}_u}}.$$

As the image of $\mathcal{F}_{\theta_n}^{(n)}$ is one-dimensional, the model's expressive power is limited. To accurately approximate target distributions that are far from the prior, a deep network with multiple layers is often necessary. Detailed numerical results are presented in Section 4.

2.3.2. Functional Projected Transformation Flow

The second model is termed functional projected transformation flow. Let $\{\phi_i\}_{i=1}^M$ be the first M eigenvectors of the prior covariance operator, and we define two operators \mathcal{P} , \mathcal{Q} :

$$\mathcal{P}u = (\langle u, \phi_1 \rangle_{\mathcal{H}_u}, \langle u, \phi_2 \rangle_{\mathcal{H}_u}, \dots, \langle u, \phi_M \rangle_{\mathcal{H}_u})^T, \quad (2.8)$$

$$\mathcal{Q}d = \sum_{i=1}^M d_i \phi_i. \quad (2.9)$$

The transformation applied to each layer is defined as follows:

$$f_{\theta_n}^{(n)}(u) = u + \mathcal{Q}R_n(\mathcal{P}u + b_n),$$

where \mathcal{P} is defined in (2.8), \mathcal{Q} is defined in (2.9), R_n is a $M \times M$ matrix, $b_n \in \mathbb{R}^M$, and the parameters set is given by $\theta_n = \{R_n, b_n\}$. The following theorem guarantees the model's adherence to the theoretical framework proposed in Subsection 2.2.

Theorem 2.6. Let \mathcal{H}_u be a separable Hilbert space equipped with the Gaussian measure $\mu_0 = \mathcal{N}(0, \mathcal{C})$, and $\mathcal{H} = \mathcal{H}(\mu_0)$ be the Cameron-Martin space of the measure μ_0 . For each $n = 1, 2, \dots, N$, let $f_{\theta_n}^{(n)}(u) = u + \mathcal{Q}R_n(\mathcal{P}u + b_n)$, where $\mathcal{F}_{\theta_n}^{(n)}$ is an operator from \mathcal{H}_u to \mathcal{H}_u and $\theta_n = \{R_n, b_n\}$ be its parameters. The composite transformation f_θ is defined by $f_\theta(u) = f_{\theta_N}^{(N)} \circ f_{\theta_{N-1}}^{(N-1)} \circ \dots \circ f_{\theta_1}^{(1)}(u)$, and μ_{f_θ} denotes its corresponding push-forward measure given by $\mu_{f_\theta} = \mu_0 \circ f_\theta^{-1}$. Assuming the following conditions hold for all $n = 1, 2, \dots, N$ and any value of θ_n :

- The space $\text{Im}(\mathcal{Q}) \subset \mathcal{H}$.
- All the point spectrum of R_n are not in $(-\infty, -1]$.

Then we have $\mu_{f_\theta} \sim \mu$ and

$$\frac{d\mu_{f_\theta}}{d\mu_0}(f_\theta(u)) = \prod_{n=1}^N \left| \det_1(Df_{\theta_n}^{(n)}(u_{n-1})) \right|^{-1} \exp \left(\frac{1}{2} \langle f_\theta(u) - u, f_\theta(u) - u \rangle_{\mathcal{H}} + \langle u, u - f_\theta(u) \rangle_{\mathcal{H}} \right),$$

where $u_n = f_{\theta_n}^{(n)} \circ f_{\theta_{n-1}}^{(n-1)} \circ \dots \circ f_{\theta_1}^{(1)}(u)$ for each $n = 1, 2, \dots, N$.

The point spectrum of $I + \mathcal{Q}R_n\mathcal{P}$ corresponds one-to-one with the eigenvalues of $I_M + R_n$. To ensure that the eigenvalues of R_n are strictly greater than -1 , we restrict R_n to be an upper triangular matrix with diagonal elements in $(-1, +\infty)$.

Note that the image of $\mathcal{F}_{\theta_n}^{(n)}$ is a M -dimensional space, functional projected transformation flow may exhibit greater expressive capacity than functional Householder flow. Detailed numerical results can be found in Section 4.

2.4. Nonlinear Transformation

In this subsection, we will explore two different nonlinear flow models. Theorem 2.4 requires that the function $f_{\theta_n}^{(n)}$ be invertible for all values of n and θ_n . To guarantee this property for our nonlinear flow, we introduce Lemma 2.2.

Lemma 2.2. Let \mathcal{H}_u be a separable Hilbert space, $f_{\theta_n}^{(n)} : \mathcal{H}_u \rightarrow \mathcal{H}_u$, and $f_{\theta_n}^{(n)}(u) = u + \mathcal{F}_{\theta_n}^{(n)}(u)$. Assuming the following conditions hold for all $n = 1, 2, \dots, N$ and any value of θ_n :

- The operator $\mathcal{F}_{\theta_n}^{(n)}$ is a finite rank operator.
- The image space of operator $\mathcal{F}_{\theta_n}^{(n)}$ is bounded in \mathcal{H}_u .
- For any $u \in \mathcal{H}_u$, all point spectrum of $D\mathcal{F}_{\theta_n}^{(n)}(u)$ are not in $(-\infty, -1]$.

Then the operator $f_{\theta_n}^{(n)}$ is bijective.

2.4.1. Functional Planar Flow

The first nonlinear model, termed functional planar flow, is a generalization of the planar flow in Euclidean space [40]. Each layer of functional Householder flow employs the transformation:

$$f_{\theta_n}^{(n)}(u) = u + u_n h(\langle w_n, u \rangle_{\mathcal{H}_u} + b_n), \quad (2.10)$$

where $u_n, w_n \in \mathcal{H}_u$, $b_n \in \mathbb{R}$, $h(x) = \tanh(x)$ and the parameters set is given by $\theta_n = \{u_n, w_n, b_n\}$. The following theorem guarantees the model's adherence to the theoretical framework proposed in Subsection 2.2.

Theorem 2.7. Let \mathcal{H}_u be a separable Hilbert space equipped with the Gaussian measure $\mu_0 = \mathcal{N}(0, \mathcal{C})$, and $\mathcal{H} = \mathcal{H}(\mu_0)$ be the Cameron-Martin space of the measure μ_0 . For each $n = 1, 2, \dots, N$, let $f_{\theta_n}^{(n)}(u) = u + u_n h(\langle w_n, u \rangle_{\mathcal{H}_u} + b_n)$, where $\mathcal{F}_{\theta_n}^{(n)}$ is an operator from \mathcal{H}_u to \mathcal{H}_u and $\theta_n = \{u_n, w_n, b_n\}$ be its parameters. The composite transformation f_θ is defined by $f_\theta(u) = f_{\theta_N}^{(N)} \circ f_{\theta_{N-1}}^{(N-1)} \circ \dots \circ f_{\theta_1}^{(1)}(u)$, and μ_{f_θ} denotes its corresponding push-forward measure given by $\mu_{f_\theta} = \mu_0 \circ f_\theta^{-1}$. Assuming the following conditions hold for all $n = 1, 2, \dots, N$ and any value of θ_n :

- $w_n, u_n \in \mathcal{H}$.
- $\langle u_n, w_n \rangle_{\mathcal{H}_u} > -1$.

Then we have $\mu_{f_\theta} \sim \mu$ and

$$\frac{d\mu_{f_\theta}}{d\mu_0}(f_\theta(u)) = \prod_{n=1}^N \left| \det_1(Df_{\theta_n}^{(n)}(u_{n-1})) \right|^{-1} \exp \left(\frac{1}{2} \langle f_\theta(u) - u, f_\theta(u) - u \rangle_{\mathcal{H}} + \langle u, u - f_\theta(u) \rangle_{\mathcal{H}} \right),$$

where $u_n = f_{\theta_n}^{(n)} \circ f_{\theta_{n-1}}^{(n-1)} \circ \dots \circ f_{\theta_1}^{(1)}(u)$ for each $n = 1, 2, \dots, N$.

Given that the parameters u_n and w_n of our flow model are functions, efficient parameterization is paramount to both computational efficiency and ensuring compliance with the theorem's constraints. To address this, we propose a novel parameterization method for the flow model. Let $\{\phi_i\}_{i=1}^M$ represent the first M eigenvectors of the prior covariance operator. Our parameterization of u_n and w_n involves a two-step process. Firstly, auxiliary vectors \hat{u}_n, \hat{w}_n are introduced and parameterized as

$$\hat{u}_n = \sum_{i=1}^M \alpha_i^n \phi_i, \quad \hat{w}_n = \sum_{i=1}^M \beta_i^n \phi_i. \quad (2.11)$$

Secondly, considering the conditions of Theorem 2.7, i.e. $\langle u_n, w_n \rangle_{\mathcal{H}_u} > -1$, we parameterize u_n and w_n using \hat{u}_n and \hat{w}_n as follows:

$$w_n = \hat{w}_n, \quad (2.12)$$

$$u_n = \hat{u}_n + [q(\langle \hat{u}_n, \hat{w}_n \rangle_{\mathcal{H}_u}) - \langle \hat{u}_n, \hat{w}_n \rangle_{\mathcal{H}_u}] \frac{\hat{w}_n}{\|\hat{w}_n\|_{\mathcal{H}_u}}, \quad (2.13)$$

where $q(x) = \ln(1 + e^x) - 1$.

Like the functional Householder flow, the image of $\mathcal{F}_{\theta_n}^{(n)}$ is constrained to a one-dimensional space, which limits the model's expressive capabilities. To effectively approximate target measures that are significantly different from the prior, a deep network architecture with multiple layers is often necessary. The effectiveness of this approach is demonstrated through numerical experiments in Section 4.

2.4.2. Functional Sylvester Flow

The second nonlinear model we are exploring, known as functional Sylvester flow, is an extension of Sylvester flow, a concept traditionally applied in Euclidean space [46]. Each layer of functional Sylvester flow utilizes the following transformation:

$$f_{\theta_n}^{(n)}(u) = u + \mathcal{A}_n h(\mathcal{B}_n u + b_n),$$

where \mathcal{A}_n is a bounded linear operator mapping from \mathcal{H}_u to \mathbb{R}^M , \mathcal{B}_n is a bounded linear operator mapping from \mathbb{R}^M to \mathcal{H}_u , $b_n \in \mathbb{R}^M$, $h(x) = \tanh(x)$, and the parameter set is given by $\theta_n = \{\mathcal{A}_n, \mathcal{B}_n, b_n\}$. The following theorem ensures that this model adheres to the theoretical framework we outlined in Subsection 2.2.

Theorem 2.8. Let \mathcal{H}_u be a separable Hilbert space equipped with the Gaussian measure $\mu_0 = \mathcal{N}(0, \mathcal{C})$, and $\mathcal{H} = \mathcal{H}(\mu_0)$ be the Cameron-Martin space of the measure μ_0 . For each $n = 1, 2, \dots, N$, let $f_{\theta_n}^{(n)}(u) = u + \mathcal{A}_n h(\mathcal{B}_n u + b_n)$, where $\mathcal{F}_{\theta_n}^{(n)}$ is an operator from \mathcal{H}_u to \mathcal{H}_u and $\theta_n = \{\mathcal{A}_n, \mathcal{B}_n, b_n\}$ be its parameters. The composite transformation f_θ is defined by $f_\theta(u) = f_{\theta_N}^{(N)} \circ f_{\theta_{N-1}}^{(N-1)} \circ \dots \circ f_{\theta_1}^{(1)}(u)$,

and μ_{f_θ} denotes its corresponding push-forward measure given by $\mu_{f_\theta} = \mu_0 \circ f_\theta^{-1}$. Assuming the following conditions hold for all $n = 1, 2, \dots, N$ and any value of θ_n :

- The space $\text{Im}(\mathcal{A}_n) \subset \mathcal{H}$.
- The operator \mathcal{A}_n is a finite rank operator.
- All the point spectrum of $\mathcal{B}_n \mathcal{A}_n$ are not in $(-\infty, -1]$.

Then we have $\mu_{f_\theta} \sim \mu$ and

$$\frac{d\mu_{f_\theta}(f_\theta(u))}{d\mu_0} = \prod_{n=1}^N \left| \det_1(Df_{\theta_n}^{(n)}(u_{n-1})) \right|^{-1} \exp \left(\frac{1}{2} \langle f_\theta(u) - u, f_\theta(u) - u \rangle_{\mathcal{H}} + \langle u, u - f_\theta(u) \rangle_{\mathcal{H}} \right),$$

where $u_n = f_{\theta_n}^{(n)} \circ f_{\theta_{n-1}}^{(n-1)} \circ \dots \circ f_{\theta_1}^{(1)}(u)$ for any $n = 1, 2, \dots, N$.

Given that the parameters \mathcal{A}_n and \mathcal{B}_n of the flow model are operators, efficient parameterization is essential for both computational efficiency and ensuring compliance with the theorem's constraints. We select the first M eigenvectors of the prior covariance operator, denoted as $\{\phi_i\}_{i=1}^M$. The parameterization of \mathcal{B}_n involves two steps:

- The first step is defined by the operator $\mathcal{B}_n^{(1)}$ as follows:

$$p_{\mathcal{B}} = \mathcal{B}_n^{(1)} u := \begin{pmatrix} \langle u, \phi_1 \rangle_{\mathcal{H}_u} \\ \langle u, \phi_2 \rangle_{\mathcal{H}_u} \\ \vdots \\ \langle u, \phi_M \rangle_{\mathcal{H}_u} \end{pmatrix}.$$

- The second step is defined by the operator $\mathcal{B}_n^{(2)}$ as follows:

$$\mathcal{B}_n^{(2)} p_{\mathcal{B}} := R_{\mathcal{B}}^n p_{\mathcal{B}}, \quad (2.14)$$

where $R_{\mathcal{B}}^n$ is a square matrix that maps $p_{\mathcal{B}}$ to the target.

The overall operator \mathcal{B}_n for $u \in \mathcal{H}_u$ is defined as $\mathcal{B}_n = \mathcal{B}_n^{(2)} \mathcal{B}_n^{(1)} u$, representing the composition of the two aforementioned steps.

The parameterization of \mathcal{A}_n is achieved through the following two steps:

- We map the vector d to $p_{\mathcal{A}} \in \mathbb{R}^M$ by a square matrix $R_{\mathcal{A}}^n$. This step is defined by the operator $\mathcal{A}_n^{(1)}$ as follows:

$$p_{\mathcal{A}} = \mathcal{A}_n^{(1)} d := R_{\mathcal{A}}^n d. \quad (2.15)$$

- The second step is defined as follows:

$$\mathcal{A}_n^{(2)} p_{\mathcal{A}} := \sum_{i=1}^M p_{\mathcal{A}}^i \phi_i,$$

where $p_{\mathcal{A}}^i$ is the value of the i -th position of the vector $p_{\mathcal{A}}$.

The overall operator \mathcal{A}_n is defined for $d \in \mathbb{R}^M$ as $\mathcal{A}_n = \mathcal{A}_n^{(2)} \mathcal{A}_n^{(1)} d$, representing the composition of the two aforementioned steps.

To satisfy the conditions imposed by Theorem 2.4, we establish the following result.

Theorem 2.9. Let \mathcal{H}_u be a separable Hilbert space, \mathcal{B} be a bounded linear operator from \mathcal{H}_u to \mathbb{R}^M , \mathcal{A} be a bounded linear operator from \mathbb{R}^M to \mathcal{H}_u . We have:

- The point spectrum of $I + \mathcal{A}\mathcal{B}$ corresponds one-to-one with the eigenvalues of $I_M + \mathcal{B}\mathcal{A}$.
- The Fredholm determinant of $I + \mathcal{A}\mathcal{B}$ is equal to the determinant of $I_M + \mathcal{B}\mathcal{A}$.

Based on Theorem 2.9, we have the following equality:

$$\det_1(I + \mathcal{A}_n \text{diag}(h'(\mathcal{B}_n u + b_n))\mathcal{B}_n) = \det(I_M + \text{diag}(h'(\mathcal{B}_n u + b_n))\mathcal{B}_n \mathcal{A}_n).$$

This allows us to efficiently compute the Fredholm determinant of the operator $Df_{\theta_n}^{(n)}(u) = I + \mathcal{A}_n \text{diag}(h'(\mathcal{B}_n u + b_n))\mathcal{B}_n$. Theorem 2.9 establishes the equivalence between the point spectrum of $I + \mathcal{A}_n \text{diag}(h'(\mathcal{B}_n u + b_n))\mathcal{B}_n$ and the eigenvalues of the matrix $I_M + \text{diag}(h'(\mathcal{B}_n u + b_n))\mathcal{B}_n \mathcal{A}_n$. In order to ensure that the eigenvalues of $\text{diag}(h'(\mathcal{B}_n u + b_n))\mathcal{B}_n \mathcal{A}_n$ are not in $(-\infty, -1]$, we set $R_{\mathcal{B}}^n$ in (2.14) as an upper triangular matrix, $R_{\mathcal{A}}^n$ in (2.15) as a lower triangular matrix, the diagonal elements of $R_{\mathcal{B}}^n$ are all 1, and the diagonal elements of $R_{\mathcal{A}}^n$ are all greater than -1 . Through this method, $\text{diag}(h'(\mathcal{B}_n u + b_n))\mathcal{B}_n \mathcal{A}_n$ is an upper triangular matrix, and the diagonal elements are all greater than -1 . Hence we can compute the determinant of $I_M + \text{diag}(h'(\mathcal{B}_n u + b_n))\mathcal{B}_n \mathcal{A}_n$ quickly.

Since the image of $\mathcal{F}_{\theta_n}^{(n)}$ is a M -dimensional space, functional Sylvester flow may exhibit a higher degree of expressive power compared to functional planar flow. We will delve into detailed numerical results in Section 4.

2.5. Discretization Invariance

The model, defined within a function space, inherently implies discretization invariance. In general, it can be summarized as the following three properties [29]:

- It operates on any discretization of the input function, meaning it can accept any set of points within the input domain.
- Its output can be evaluated at any point in the output domain.
- As the discretization becomes finer, the model converges to a continuous operator.

In this subsection, we investigate the discretization invariance of the operator $\mathcal{F}_{\theta_n}^{(n)}$ within the flow model $f_{\theta_n}^{(n)} = I + \mathcal{F}_{\theta_n}^{(n)}$. Following the approach outlined in [29], a formal definition of the discretization invariance is provided.

Definition 2.1. We call a discrete refinement of the domain $D \subset \mathbb{R}^d$ any sequence of nested sets $D_1 \subset D_2 \subset \dots \subset D$ with $|D_L| = L$ for any $L \in \mathbb{N}$ such that, for any $\epsilon > 0$, there exists a number $L = L(\epsilon) \in \mathbb{N}$ such that

$$D \subset \bigcup_{x \in D_L} \{y \in \mathbb{R}^d : \|y - x\| < \epsilon\}.$$

Definition 2.2. Given a discrete refinement $\{D_L\}_{L=1}^{\infty}$ of the domain $D \subset \mathbb{R}^d$, any member D_L is called a discretization of D .

Definition 2.3. Suppose \mathcal{H}_u is a Hilbert space of \mathbb{R}^m valued functions on the domain $D \subset \mathbb{R}^d$. For any θ_n , let $\mathcal{F}_{\theta_n}^{(n)} : \mathcal{H}_u \rightarrow \mathcal{H}_u$ be an operator, D_L be an L -point discretization of D , and operator $\hat{\mathcal{F}}_{\theta_n(L)}^{(n)} : \mathbb{R}^{Lm} \rightarrow \mathcal{H}_u$. For any $K \subset C(D)$ compact, we define the discretized uniform risk as

$$R_K(\mathcal{F}_{\theta_n}^{(n)}, \hat{\mathcal{F}}_{\theta_n(L)}^{(n)}) = \sup_{a \in K} \left\| \hat{\mathcal{F}}_{\theta_n(L)}^{(n)}(a|_{D_L}) - \mathcal{F}_{\theta_n}^{(n)}(a) \right\|_{\mathcal{H}_u}.$$

Definition 2.4. Given a discrete refinement $\{D_n\}_{n=1}^{\infty}$ of the domain $D \subset \mathbb{R}^d$. For any fixed θ_n , we say $\mathcal{F}_{\theta_n}^{(n)}$ is discretization-invariant if there exists a sequence of maps $\hat{\mathcal{F}}_{\theta_n(1)}^{(n)}, \hat{\mathcal{F}}_{\theta_n(2)}^{(n)}, \dots$ where $\hat{\mathcal{F}}_{\theta_n(L)}^{(n)} : \mathbb{R}^{Lm} \rightarrow \mathcal{H}_u$ such that, for any compact set $K \subset C(D)$,

$$\lim_{L \rightarrow \infty} R_K(\mathcal{F}_{\theta_n}^{(n)}, \hat{\mathcal{F}}_{\theta_n(L)}^{(n)}) = 0.$$

Under the proposed definition, the aforementioned four flow models can be shown to exhibit discretization invariance.

Theorem 2.10. Let $D \subset \mathbb{R}^d$ be a domain for some $d \in \mathbb{N}$. Suppose that \mathcal{H}_u can be continuously embedded in $C(D)$. Then for any $n \in \mathbb{N}$, the layers $\mathcal{F}_{\theta_n}^{(n)} : \mathcal{H}_u \rightarrow \mathcal{H}_u$ of functional planar flow, functional Householder flow, functional Sylvester flow, and functional projected transformation flow are discretization-invariant.

Next, we compare and contrast the functional normalizing flow framework with standard normalizing flow in Euclidean space. A key property contributing to the success of normalizing flow in computer vision is the tractability of the density of the post-transformed distribution. To achieve this, the transformation $\tilde{f}(z)$ of normalizing flow in Euclidean space must be invertible [18, 40]. In this case, the post-transformed density can be expressed as

$$p_1(z') = p_0(z) \left| \det \left(\frac{\partial \tilde{f}(z)}{\partial z} \right) \right|^{-1},$$

where $z' = \tilde{f}(z)$, $z, z' \in \mathbb{R}^L$ and \tilde{f} maps from \mathbb{R}^L to \mathbb{R}^L , the densities of the post-transformed and pre-transformed distributions are denoted by $p_1(z)$ and $p_0(z)$, respectively. This tractable form allows for the computation of the Kullback-Leibler divergence between the target distribution and the post-transformed distribution, which is used as the loss function.

In this paper, we demonstrate the applicability of similar ideas within the infinite-dimensional Hilbert space \mathcal{H}_u , aligning well with the Bayesianize-then-Discretize approach for inverse problem. Similar to the normalizing flow in Euclidean space, ensuring the invertibility of the transformation f_{θ} is crucial for the tractability of the RN derivative between the post-transformed and pre-transformed measures [7]. While various different approaches have been proposed to ensure the invertibility of normalizing flow transformations in Euclidean space [18, 40], we present general theorems (Lemmas 2.1 and 2.2) that establish conditions for the invertibility of transformations within the infinite-dimensional function space. This ensures the tractability of the RN derivative between the post-transformed measure and the prior, enabling the calculation of the KL divergence as the loss function.

Lastly, we demonstrate that, by picking a parameterization that is inconsistent in function space, the model we proposed will degenerate to the standard normalizing flow in Euclidean space. For illustrative purposes, we will consider a simple example using functional planar flow (2.10). Let u be a real-valued function defined on the domain $D \subset \mathbb{R}^m$, $\mathcal{H}_u = L^2(D)$, $x^1, x^2, \dots, x^L \in D$ be the

points at which the input function u is evaluated and denote $\mathbf{u} = (u(x^1), u(x^2), \dots, u(x^L)) \in \mathbb{R}^L$ the vector of evaluations. Let $w_n(x^i) = w_n^{(i)}$, $u_n(x^i) = u_n^{(i)}$ for $i = 1, \dots, L$ where $w_n^{(i)}, u_n^{(i)} \in \mathbb{R}$ are some constants. Employing a Monte Carlo approximation, the functional planar flow can be discretized as

$$\tilde{f}_{\theta_n}^{(n)}(\mathbf{u}) = \mathbf{u} + \mathbf{u}_n h \left(\frac{1}{L} \sum_{i=1}^L w_n^{(i)} u(x^i) + b_n \right). \quad (2.16)$$

This expression can be simplified to

$$\tilde{f}_{\theta_n}^{(n)}(\mathbf{u}) = \mathbf{u} + \mathbf{u}_n h(\langle \mathbf{w}_n, \mathbf{u} \rangle_{\mathbb{R}^L} + b_n), \quad (2.17)$$

where $\mathbf{u}_n = (u_n^{(1)}, \dots, u_n^{(L)})$, $\mathbf{w}_n = (w_n^{(1)}, \dots, w_n^{(L)})$, $b_n \in \mathbb{R}$ is constant, $h(x) = \tanh(x)$. Parameters θ_n can be regarded as $\theta_n = \{\mathbf{u}_n, \mathbf{w}_n, b_n\}$. The construction (2.16) can be generalized to arbitrary number of layers by composing several transformations together

$$\tilde{f}_{\theta}(\tilde{u}) = \tilde{f}_{\theta_N}^{(N)} \circ \tilde{f}_{\theta_{N-1}}^{(N-1)} \circ \dots \circ \tilde{f}_{\theta_1}^{(1)}(\tilde{u}). \quad (2.18)$$

The obtained model (2.18) is the planar flow defined in the Euclidean space [40]. It is evident that when employing the planar flow (2.17) in function spaces, the parameterization of w_n becomes contingent upon the specific discretization of the input \mathbf{u} . Likewise, the parameterization of u_n depends on the desired discretization of the output. Consequently, for varying discretization requirements, the entire model necessitates retraining, precluding the ability to generalize to arbitrary discretized inputs and outputs. Consequently, standard planar flow in Euclidean space are not consistent within the infinite-dimensional function space, and it is not discretization-invariant.

3. Conditional Normalizing Flow in Function Space

While Section 2 establishes the theoretical framework for functional normalizing flow, the practical application of Algorithm 1 is hindered by the computational cost of repeatedly solving forward problems. To address this limitation, strategies for reducing the algorithm's iteration are essential.

In order to mitigate the computational burden, we propose conditional functional normalizing flow, which involve pre-training a model to map measurement data and their corresponding measurement points to the parameters of a functional normalizing flow, enabling efficient estimation of posterior for new measurement.

Our objective is to learn the map from measurement information (measurement data \mathbf{d} and their corresponding measurement points \mathbf{x}) to the parameters of a functional normalizing flow model, enabling approximation of posterior corresponding to the given measurement information. Following model training, the conditional functional normalizing flow can efficiently generate approximate posterior for new measurement information. While this provides an initial estimate, further refinement can be achieved through fine-tuning the model on specific measurement information, leveraging the initial estimate as a starting point. This approach significantly reduces the number of iterations required compared with training from a random initialization.

3.1. Basic Setting of Conditional Normalizing Flow

Conditional functional normalizing flow aim to solve a class of inverse problems using a unified model. In constructing such a model, the position of the measurement points \mathbf{x} and the measurement data \mathbf{d} play an important role. When employing a conditional network for solving inverse

problems, both \mathbf{x} and \mathbf{d} are considered variable quantities. Therefore, we need to reformulate the framework proposed in Section 2. Let $\mathbf{x} = (x^1, x^2, \dots, x^{N_{\mathbf{d}}})$ represents the measurement points of the solution, and let $\mathbf{d} = (w(x^1), w(x^2), \dots, w(x^{N_{\mathbf{d}}}))$ denotes the measurement data, where w is the function $\mathcal{G}(u)$.

Let $\mathcal{G} : \mathcal{H}_u \rightarrow \mathcal{H}_w$ represents the solution operator of the corresponding PDE, where \mathcal{H}_u is the parameter space, and \mathcal{H}_w is the solution space. The measurement locations, denoted by \mathbf{x} , influence the observation operator $\mathcal{S}_{\mathbf{x}}$, formally defined as:

$$\mathcal{S}_{\mathbf{x}} : \mathcal{H}_w \rightarrow \mathbb{R}^{N_{\mathbf{d}}},$$

where $N_{\mathbf{d}}$ is the number of observed points. Specifically, the operator $\mathcal{S}_{\mathbf{x}}$ acts as follows:

$$\mathcal{S}_{\mathbf{x}}(w) = (w(x^1), w(x^2), \dots, w(x^{N_{\mathbf{d}}})).$$

Then, the problem can be formulated as

$$\mathbf{d} = \mathcal{S}_{\mathbf{x}}\mathcal{G}(u) + \epsilon,$$

where $\mathbf{d} \in \mathbb{R}^{N_{\mathbf{d}}}$ is the measurement data, $u \in \mathcal{H}_u$ is the interested parameter, and ϵ is a Gaussian random vector with zero mean and covariance matrix $\mathbf{\Gamma}_{\text{noise}} := \tau^{-1}\mathbf{I}$ (τ is a fixed positive number, \mathbf{I} denotes the $N_{\mathbf{d}}$ -dimensional identity matrix), which means

$$\epsilon \sim \mathcal{N}(0, \mathbf{\Gamma}_{\text{noise}}).$$

Our objective is to infer the possible values of the function parameter u based on measurement data \mathbf{d} and their corresponding measurement points \mathbf{x} . After incorporating the measurement points \mathbf{x} , the Bayes' formula is given by

$$\frac{d\mu_{(\mathbf{x}, \mathbf{d})}}{d\mu_0}(u) = \frac{1}{Z_{\mu}^{(\mathbf{x}, \mathbf{d})}} \exp(-\Phi_{(\mathbf{x}, \mathbf{d})}(u)), \quad (3.1)$$

where $\mu_{(\mathbf{x}, \mathbf{d})}$ is the posterior, the potential function $\Phi_{(\mathbf{x}, \mathbf{d})} : \mathcal{H}_u \rightarrow \mathbb{R}$ is defined as

$$\Phi_{(\mathbf{x}, \mathbf{d})}(u) = \frac{1}{2} \|\mathbf{d} - \mathcal{S}_{\mathbf{x}}\mathcal{G}(u)\|_{\mathbf{\Gamma}_{\text{noise}}}^2,$$

with $\|\cdot\|_{\mathbf{\Gamma}_{\text{noise}}} := \|\mathbf{\Gamma}_{\text{noise}}^{-1/2}\cdot\|$, and $Z_{\mu}^{(\mathbf{x}, \mathbf{d})}$ is the normalization constant given by

$$Z_{\mu}^{(\mathbf{x}, \mathbf{d})} = \int_{\mathcal{H}_u} \exp(-\Phi_{(\mathbf{x}, \mathbf{d})}(u)) \mu_0(du).$$

The goal of conditional functional normalizing flow is to approximate the posterior of Bayes' formulas corresponding to different measurement information (\mathbf{x}, \mathbf{d}) , but with the same forward operator \mathcal{G} . We hope that, after entering the measurement information (\mathbf{x}, \mathbf{d}) into the neural network, we can directly obtain an approximate measure of the posterior $\mu_{(\mathbf{x}, \mathbf{d})}$ of the corresponding Bayes' formula (3.1).

It is crucial to note that the measurement information (\mathbf{x}, \mathbf{d}) is dynamic and heterogeneous. Variations in the number, positions, and values of measurement points lead to varying dimensions and scales of the information. To enable the application of neural networks, we aim to transform this diverse data into a fixed-length vector.

We develop a method to integrate two pieces of information, i.e., measurement data \mathbf{d} and their corresponding locations \mathbf{x} . The adjoint operator of $\mathcal{S}_{\mathbf{x}}$, denoted $\mathcal{S}_{\mathbf{x}}^*$, maps vector in $\mathbb{R}^{N_{\mathbf{d}}}$ to functional in the dual space \mathcal{H}_w^* . Formally,

$$\mathcal{S}_{\mathbf{x}}^* : \mathbb{R}^{N_{\mathbf{d}}} \rightarrow \mathcal{H}_w^*.$$

The specific action of the adjoint operator is given by

$$\mathcal{S}_{\mathbf{x}}^* \mathbf{d}(u) = (\mathbf{d}, \mathcal{S}_{\mathbf{x}} u)_{\mathbb{R}^{N_d}} = \sum_{i=1}^{N_d} d_i u(x_i),$$

where d_i denotes the i -th value of the vector \mathbf{d} . The adjoint operator $\mathcal{S}_{\mathbf{x}}^*$ can be used to integrate measurement data \mathbf{d} and their corresponding measurement points \mathbf{x} into a functional $\mathcal{S}_{\mathbf{x}}^* \mathbf{d}$. However, neural networks typically require vectors input. To address this issue, we propose calculating the values of the functional on a set of fixed functions, resulting in a vector \mathbf{v} that can be directly input into the neural network. The entire process $\mathcal{W}(\mathbf{x}, \mathbf{d}) = \mathbf{v}$ can be divided into the following two steps:

- Basis selection: Choose a set of basis functions $\{\phi_i\}_{i=1}^n$ that span the relevant function space. Here we select the first M eigenvectors of the prior covariance operator $\{\phi_i\}_{i=1}^M$.
- Functional evaluation: For each basis function ϕ_i , compute $\mathcal{S}_{\mathbf{x}}^* \mathbf{d}(\phi_i)$, and collect these scalar values into a vector $\mathbf{v} = (\mathcal{S}_{\mathbf{x}}^* \mathbf{d}(\phi_1), \mathcal{S}_{\mathbf{x}}^* \mathbf{d}(\phi_2), \dots, \mathcal{S}_{\mathbf{x}}^* \mathbf{d}(\phi_n))$.

Under these circumstances, we can construct a neural network that maps the vector \mathbf{v} to the parameters of the functional normalizing flow. Notably, the parameters of the functional normalizing flow are denoted as $\theta = \{\theta_1, \theta_2, \dots, \theta_N\}$, where θ_n corresponds to the parameters of a transformation $f_{\theta_n}^{(n)}$ within the model for $n = 1, 2, \dots, N$. We construct a neural network $\mathcal{N}_{\lambda_n}^{(n)}(\mathbf{v})$ for each transformation, mapping the vector \mathbf{v} to the parameters θ_n . This neural network has its own parameters, denoted by λ_n . By training the network, we can effectively control the parameters θ_n of each transformation $f_{\theta_n}^{(n)}$ based on the measurement information \mathbf{x} and \mathbf{d} . The collection of all neural networks $\{\mathcal{N}_{\lambda_n}^{(n)}(\mathbf{v})\}_{n=1}^N$ can be compactly represented as $\mathcal{N}_{\lambda}(\mathbf{v}) = \theta$, where $\lambda = \{\lambda_1, \lambda_2, \dots, \lambda_N\}$ denotes the combined parameters of these neural networks.

Unlike functional normalizing flow introduced in Section 2, we propose a novel approach where the model parameters for each measurement information (\mathbf{x}, \mathbf{d}) are generated directly by a neural network $\mathcal{N}_{\lambda}(\mathbf{v})$, rather than being learned through training. In other words, once the parameters λ of the neural network $\mathcal{N}_{\lambda}(\mathbf{v})$ are trained, we can directly generate the parameters of the corresponding flow model for any given measurement information (\mathbf{x}, \mathbf{d}) . Next, we will delve into the details of training the parameters λ of the neural network $\mathcal{N}_{\lambda}(\mathbf{v})$.

Given a dataset $D_{train} = \{(\mathbf{x}_1, \mathbf{d}_1), (\mathbf{x}_2, \mathbf{d}_2), \dots, (\mathbf{x}_{N_{train}}, \mathbf{d}_{N_{train}})\}$, where $(\mathbf{x}_i, \mathbf{d}_i)$ represents a pair of measurement data \mathbf{d}_i and its corresponding measurement points \mathbf{x}_i for $i = 1, 2, \dots, N_{train}$, the neural network $\mathcal{N}_{\lambda}(\mathbf{v})$ can be trained. For a specific measurement information pair $(\mathbf{x}^*, \mathbf{d}^*)$, the parameters of the corresponding functional normalizing flow are given by $\theta^* = \mathcal{N}_{\lambda}(\mathbf{v}^*)$, where $\mathbf{v}^* = \mathcal{W}(\mathbf{x}^*, \mathbf{d}^*)$. As shown in (3.1), we denote the posterior corresponding to $(\mathbf{x}^*, \mathbf{d}^*)$ as $\mu_{(\mathbf{x}^*, \mathbf{d}^*)}$. We hypothesize that the flow model f_{θ^*} can transform the prior μ_0 into a measure $\nu_{\lambda}(\mathbf{v}^*)$ that closely approximates the posterior $\mu_{(\mathbf{x}^*, \mathbf{d}^*)}$. Consequently, we expect the Kullback-Leibler divergence $D_{\text{KL}}(\nu_{\lambda}(\mathbf{v}^*) || \mu_{(\mathbf{x}^*, \mathbf{d}^*)})$ to be small.

Let $\{\mathbf{v}_1, \mathbf{v}_2, \dots, \mathbf{v}_{N_{train}}\}$ be the corresponding vectors of the dataset D_{train} . We anticipate that for any $i = 1, 2, \dots, N_{train}$, $D_{\text{KL}}(\nu_{\lambda}(\mathbf{v}_i) || \mu_{(\mathbf{x}_i, \mathbf{d}_i)})$ will be small. The overall error function can be expressed as

$$q(\lambda) = \mathbb{E}_{(\mathbf{x}, \mathbf{d})} \{D_{\text{KL}}(\nu_{\lambda}(\mathbf{v}) || \mu_{(\mathbf{x}, \mathbf{d})})\} \approx \frac{1}{N_{train}} \sum_{i=1}^{N_{train}} D_{\text{KL}}(\nu_{\lambda}(\mathbf{v}_i) || \mu_{(\mathbf{x}_i, \mathbf{d}_i)}).$$

For a detailed description of the algorithm, please refer to Algorithm 2.

Algorithm 2 Conditional Functional Normalizing Flow

- 1: Initialize the neural network parameter λ to λ_0 , the learning rate schedule to α_k , the training steps to K , the sampling size to M , and the training dataset to $D_{train} = \{(\mathbf{x}_1, \mathbf{d}_1), (\mathbf{x}_2, \mathbf{d}_2), \dots, (\mathbf{x}_{N_{train}}, \mathbf{d}_{N_{train}})\}$. Then, initialize the iteration counter k to 0;
- 2: **repeat**
- 3: Randomly select M training data $\{(\mathbf{x}_{r_1}, \mathbf{d}_{r_1}), \dots, (\mathbf{x}_{r_M}, \mathbf{d}_{r_M})\}$ from dataset D_{train} , where $r_i \in \{1, 2, \dots, N_{train}\}$;
- 4: Calculate their corresponding vectors $\{\mathbf{v}_{r_1}, \mathbf{v}_{r_2}, \dots, \mathbf{v}_{r_M}\}$ with $\mathbf{v}_{r_i} = \mathcal{W}(\mathbf{x}_{r_i}, \mathbf{d}_{r_i})$;
- 5: Calculate the approximate measures $\{\nu_{\lambda_k}(\mathbf{v}_{r_1}), \nu_{\lambda_k}(\mathbf{v}_{r_2}), \dots, \nu_{\lambda_k}(\mathbf{v}_{r_M})\}$ with the neural network $\mathcal{N}_{\lambda_k}(\mathbf{v})$;
- 6: For each $i = r_1, r_2, \dots, r_M$, generate N_u functions from the measure $\nu_{\lambda_k}(\mathbf{v}_i)$, and denote them as $\{u_{i1}^{(\lambda_k)}, u_{i2}^{(\lambda_k)}, \dots, u_{iN_u}^{(\lambda_k)}\}$;
- 7: Updating the parameters $\lambda_{k+1} = \lambda_k - \alpha_k \nabla_{\lambda_k} q(\lambda_k)$ with

$$\begin{aligned} \nabla_{\lambda_k} q(\lambda_k) &= \nabla_{\lambda_k} E_{(\mathbf{x}, \mathbf{d})} \{D_{\text{KL}}(\nu_{\lambda_k}(\mathbf{v}) \parallel \mu_{(\mathbf{x}, \mathbf{d})})\} \\ &\approx \frac{1}{MN_u} \nabla_{\lambda_k} \sum_{i=1}^M \left(\sum_{j=1}^{N_u} \ln \left(\frac{d\nu_{\lambda_k}(\mathbf{v}_{r_i})}{d\mu_0}(u_{ij}^{(\lambda_k)}) \right) - \ln \left(\frac{\mu(\mathbf{x}_{r_i}, \mathbf{d}_{r_i})}{d\mu_0}(u_{ij}^{(\lambda_k)}) \right) \right). \end{aligned}$$

Variants of stochastic gradient-based optimization method can be employed in this step;

- 8: $k = k + 1$;
 - 9: **until** $k = K$;
 - 10: Return the final result λ_K ;
-

3.2. Further Training for Specific Data

In Subsection 3.1, we train a neural network $\mathcal{N}_\lambda(\mathbf{v})$ of the conditional functional normalizing flow. For a given measurement information pair $(\mathbf{x}^*, \mathbf{d}^*)$, the corresponding vector $\mathbf{v}^* = \mathcal{W}(\mathbf{x}^*, \mathbf{d}^*)$ is input to this trained network, yielding parameters $\theta^* = \mathcal{N}_\lambda(\mathbf{v}^*)$ for the functional normalizing flow. The flow model f_{θ^*} can then transform the prior μ_0 into an approximate measure $\nu_\lambda(\mathbf{v}^*)$ of the posterior $\mu(\mathbf{x}^*, \mathbf{d}^*)$. However, due to the inherent limitations of the neural network $\mathcal{N}_\lambda(\mathbf{v})$, this initial estimate may deviate from the true posterior. Consequently, the primary objective of this subsection is to develop a method for refining the approximate posterior $\nu_\lambda(\mathbf{v}^*)$ to align it more closely with the true posterior $\mu(\mathbf{x}^*, \mathbf{d}^*)$. This refinement process is crucial for enhancing the accuracy of our inference.

To refine the approximate posterior $\nu_\lambda(\mathbf{v}^*)$, we propose a retraining approach. For a specific measurement information pair $(\mathbf{x}^*, \mathbf{d}^*)$, the corresponding vector $\mathbf{v}^* = \mathcal{W}(\mathbf{x}^*, \mathbf{d}^*)$ serves as input to the trained neural network $\mathcal{N}_\lambda(\mathbf{v})$ to obtain initial parameters $\theta_0 = \mathcal{N}_\lambda(\mathbf{v}^*)$. Subsequently, the inverse problem corresponding to $(\mathbf{x}^*, \mathbf{d}^*)$ is retrained using Algorithm 1 with θ_0 as a starting point. For a detailed overview of the entire process, refer to Algorithm 3. Compared to the random initialization, this approach significantly reduces the number of iterations required for training a functional normalizing flow, as demonstrated numerically in Section 5.

Algorithm 3 Retraining Functional Normalizing Flow

- 1: For a new measurement information $(\mathbf{x}^*, \mathbf{d}^*)$, we change it into the corresponding vector $\mathbf{v}^* = \mathcal{W}(\mathbf{x}^*, \mathbf{d}^*)$, and put the vector into the trained neural network to get the parameters $\theta_\lambda = \mathcal{N}_\lambda(\mathbf{v}^*)$;
- 2: Let $\theta_0 = \theta_\lambda$ be the initial value of θ , set the sampling size N , the iterative number K , the learning rate schedule α_k , and initialize the iteration counter $k = 0$;
- 3: **repeat**
- 4: Sampling N functions $\{u_i\}_{i=1}^N$ from the prior μ_0 ;
- 5: Update the parameters $\theta_{k+1} = \theta_k - \alpha_k \nabla_{\theta_k} L(\theta_k)$ with

$$\begin{aligned} \nabla_{\theta_k} L(\theta_k) &= \nabla_{\theta_k} D_{\text{KL}}(\mu_{f_{\theta_k}} \parallel \mu(\mathbf{x}^*, \mathbf{d}^*)) \\ &\approx \frac{1}{N} \sum_{i=1}^N \nabla_{\theta_k} \ln \left(\frac{d\mu_{f_{\theta_k}}}{d\mu_0} (f_{\theta_k}(u_i)) \right) - \frac{1}{N} \sum_{i=1}^N \nabla_{\theta_k} \ln \left(\frac{d\mu(\mathbf{x}^*, \mathbf{d}^*)}{d\mu_0} (f_{\theta_k}(u_i)) \right). \end{aligned}$$

Variants of stochastic gradient-based optimization method can be employed in this step;

- 6: $k = k + 1$;
 - 7: **until** $k = K$.
 - 8: Return the final result $\theta = \theta_K$.
-

4. Numerical Examples of Functional Normalizing Flow

To demonstrate the effectiveness of our novel framework for solving inverse problems, we present two illustrative examples, i.e., the simple elliptic equation and the steady-state Darcy flow equation. These examples enable a straightforward visualization of the approximate posterior distribution and facilitate direct comparisons with benchmark results obtained from the well-established preconditioned Crank-Nicolson (pCN) algorithm [17]. All of the codes for the functional normalizing flow are available at: <https://github.com/jjx323/FunctionalNormalizingFlow>.

In the first example, given the linear nature of the inverse problem, we utilize functional Householder flow and functional projected transformation flow as our flow models. For the second example, which involves a nonlinear inverse problem, we employ functional planar flow and functional Sylvester flow. These flow models are specifically designed to capture intricate nonlinear relationships, enabling the transformation of a Gaussian distribution into a non-Gaussian distribution that more closely approximates the posterior distribution associated with the nonlinear inverse problem.

4.1. Simple Elliptic Equation

Consider the inverse source problem associated with the elliptic equation:

$$\begin{aligned} -\alpha \Delta w + w &= u, \quad \text{in } \Omega, \\ \frac{\partial w}{\partial \mathbf{n}} &= 0, \quad \text{on } \partial\Omega, \end{aligned} \tag{4.1}$$

where $\Omega = (0, 1) \subset \mathbb{R}$, $\alpha > 0$ is a positive constant, and \mathbf{n} denotes the outward unit normal vector. The forward operator is defined as

$$\mathcal{S}G u = (w(x^1), w(x^2), \dots, w(x^{N_d}))^T, \tag{4.2}$$

where \mathcal{G} is the PDE solution operator from $\mathcal{H}_u := L^2(\Omega)$ to $\mathcal{H}_w := H^2(\Omega)$, \mathcal{S} is the measurement operator from \mathcal{H}_w to \mathbb{R}^{N_d} , $u \in \mathcal{H}_u$, $w \in \mathcal{H}_w$ denotes the solution of the elliptic equation (4.1), and $x^i \in \Omega$ for $i = 1, 2, \dots, N_d$. With these notations, the problem can be written abstractly as

$$\mathbf{d} = \mathcal{S}\mathcal{G}u + \epsilon. \quad (4.3)$$

For clarity, we list the specific choices for some parameters introduced in this subsection as follows:

- Assume that 5% random Gaussian noise $\epsilon \sim \mathcal{N}(0, \mathbf{\Gamma}_{\text{noise}})$ is added, where $\mathbf{\Gamma}_{\text{noise}} = \tau^{-1}\mathbf{I}$, and $\tau^{-1} = (0.05\|\mathcal{S}\mathcal{G}u\|_{\infty})^2$.
- Let the domain Ω be an interval $(0, 1)$ with $\partial\Omega = \{0, 1\}$, and the measurement data are assumed to be $\{w(x^i)|i = 1, 2, \dots, 10\}$, where $x^i = \frac{i}{10}$.
- The covariance operator \mathcal{C}_0 associated with the prior measure μ_0 is defined as $\mathcal{C}_0 = (\mathbf{I} - \alpha\Delta)^{-2}$, where $\alpha = 0.1$ is a predetermined constant. The Laplace operator is defined on Ω with homogeneous Neumann boundary condition. Additionally, the mean of the prior measure μ_0 is set to zero.
- In order to avoid inverse crime [27], the data is generated on a fine mesh with the number of grid points equal to 10^4 . And we use different sizes of mesh $n = \{50, 75, 100, 200, 300\}$ in the inverse stage.

4.1.1. Functional Householder Flow

In this subsection, we will show the effectiveness of functional Householder flow and the discretization invariance of this model. We assume that the data produced from the underlying ground truth

$$u^\dagger = \exp(-50(x - 0.3)^2) - \exp(-50(x - 0.7)^2). \quad (4.4)$$

To demonstrate the superiority of our proposed algorithm, we conduct a comparative study with the pCN algorithm. It has been theoretically established that the pCN algorithm can generate samples from the true posterior distribution [17]. Consequently, we treat the samples obtained from pCN as benchmark results for comparison. However, as a Markov chain Monte Carlo (MCMC) method, pCN samples often exhibit high autocorrelation. To acquire a sufficient number of independent samples, numerous iterations are typically required, and the computational cost of pCN scales directly with the desired number of independent samples.

In contrast, the computational burden of NF-iVI primarily lies in the training of the flow model. Once trained, the generated samples are mutually independent, which enables efficient sampling. To quantify this advantage, we employ the effective sample size (ESS) as a metric. ESS is a statistical concept used to quantify the number of independent samples within a given dataset. For a more detailed explanation, refer to [43]. Assume we have a series of sample functions u_1, u_2, \dots, u_n , and we are interested in the values of $f(u_i)$, where f is a functional and $i = 1, 2, \dots, n$. For instance, if we focus on the value of function u_i at point x_0 , then $f(u_i) = u_i(x_0)$. ESS is calculated by the following formula:

$$\text{ESS} = \text{ESS}(f, \{u_k\}_{k=1}^n) = n \left[1 + 2 \sum_{k \geq 0} \gamma_k(f) \right]^{-1},$$

where n is the number of samples and $\gamma_k(f)$ denotes the autocorrelation function of the samples, which is estimated by:

$$\gamma_k(f) = \frac{c_k}{c_0}, \quad c_k = \frac{1}{n} \sum_{s=\max(1,-k)}^{\min(n-k,n)} [f(u_{s+k}) - \bar{f}][f(u_s) - \bar{f}],$$

where $\bar{f} = \frac{1}{n} \sum_{s=1}^n f(u_s)$. In the discussion of all simple smooth problems, when we discuss ESS, the corresponding functional f is defined as $f(u) = u(0.5)$.

For inverse problem (4.3), we employed the pCN algorithm with a step size $\beta = 0.01$, collecting 10^6 samples. Analyzing the trace plot, we discarded the initial 10^5 samples and computed the ESS of the remaining samples as

$$\text{ESS}_p = 76,$$

where ESS_p denotes the ESS of the samples generated by pCN algorithm. Despite collecting a large number of samples, the ESS_p was found to be relatively small. The results from the pCN algorithm were used as a benchmark. To ensure adequate sampling for pCN, we collected 3×10^6 samples, and the ESS of the samples can be computed as $\text{ESS}_p = 239$.

For comparison, we generate samples with the NF-iVI algorithm. Following Algorithm 1, we use 24 layers to illustrate the functional Householder flow, and the model are trained for 5000 iterations ($K = 5000$), with each iteration utilizing 30 samples ($N = 30$). We employ a step decay learning rate schedule with an initial learning rate $\alpha_0 = 0.01$ and a multiplicative factor $\tau = 0.8$ after every 500 iterations. We collected 1000 samples and calculated the ESS as

$$\text{ESS}_{\text{NF}} = 926.$$

Remarkably, even with only 1000 samples, the ESS of the samples proposed from NF-iVI still significantly exceeded that of pCN. Furthermore, additional samples can be easily generated without incurring substantial computational overhead. For example, once the training is finished, we can collect 10,000 samples using NF-iVI and compute the ESS as $\text{ESS}_{\text{NF}} = 9658$.

Firstly, we provide some discussions of the mean function of approximate posterior. In subfigure (a) of Figure 1, we compare the mean of the approximate posterior obtained by the NF-iVI method with the ground truth. The blue solid line represents the mean of NF-iVI estimate, while the red dashed line represents the ground truth. The shaded blue region denotes the 95% credibility interval of the approximate posterior. We observe that the 95% credibility interval encompasses the ground truth, reflecting the inherent uncertainty in the parameter estimation.

Subfigure (b) of Figure 1 presents a similar comparison between the mean of the estimated posterior measure obtained by the pCN algorithm and the ground truth. The blue shaded area again represents the 95% credibility interval of the estimated posterior. As illustrated in the comparison between (a) and (b), the mean of the approximate posterior generated by functional Householder flow closely resembles the mean of posterior obtained from the pCN algorithm.

To further support the effectiveness of estimating the mean of NF-iVI method, we provide numerical evidence. By comparing it with the pCN sampling algorithm, we calculate the relative error between their estimates:

$$\text{relative error} = \frac{\|u_N^* - u_p^*\|_{L^2}^2}{\|u_p^*\|_{L^2}^2} = 0.00131, \quad (4.5)$$

where u_N^* denotes the estimated mean from functional Householder flow and u_p^* represents the estimated mean from the pCN algorithm. Obviously, the small relative error suggests the effectiveness of the proposed algorithm.

As a result, combining visual (Figure 1) and quantitative (relative error given in (4.5)) evidences, the NF-iVI method provides a good approximation of the mean of posterior.

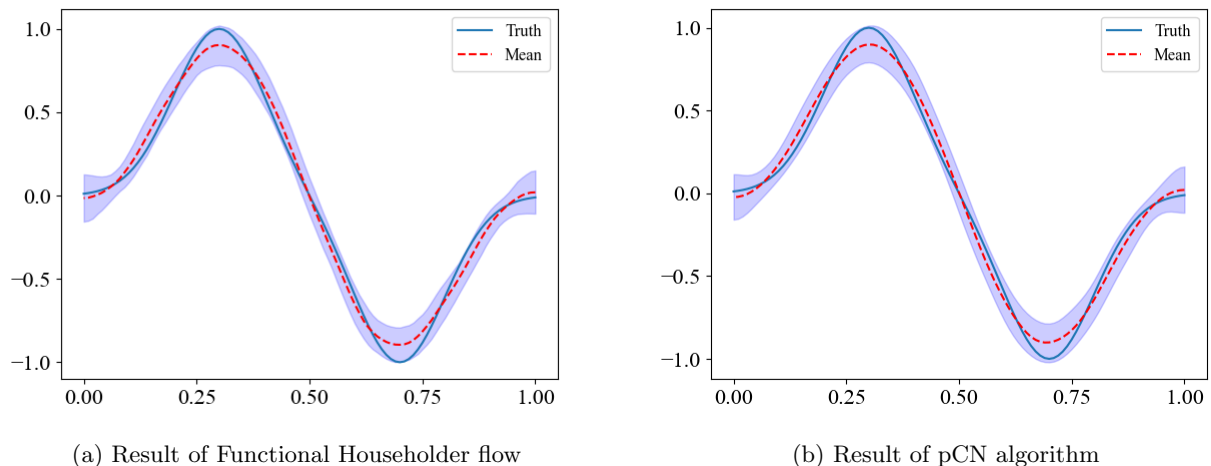


Figure 1: A comparison of the approximate posterior obtained by functional Householder flow with 24 layers and the posterior generated by the pCN algorithm. The blue shade area represents the 95% credibility region of estimated posterior. (a): Result of the approximate posterior generated by functional Householder flow compared with the background truth of u . (b): Result of the posterior generated by pCN algorithm compared with the background truth of u .

Secondly, we offer a discussion on the approximation of the posterior covariance function. Our emphasis is on presenting evidence that demonstrates the NF-iVI method's capability to provide a robust estimate of the covariance. To facilitate these comparisons, we need to introduce the definition of variance function and covariance function.

Consider a random field u on a domain Ω with mean \bar{u} and the covariance function $c(x, y)$ describing the covariance between $u(x)$ and $u(y)$:

$$c(x, y) = \mathbb{E}((u(x) - \bar{u}(x))(u(y) - \bar{u}(y))), \quad \text{for } x, y \in \Omega.$$

The corresponding covariance operator \mathcal{C} is

$$(\mathcal{C}\phi')(x) = \int_{\Omega} c(x, y)\phi'(y)dy,$$

where the function ϕ' is a sufficiently regular function defined on Ω .

The variance function, denoted by $\text{var}_u(x)$, can be estimated as follows:

$$\text{var}_u(x) \approx \frac{1}{m} \sum_{i=1}^m (u_i(x) - \bar{u}(x))^2,$$

where $x \in \Omega$ is a point residing in the domain Ω , \bar{u} is the mean function, and m is the sample

number. The covariance function can be estimated as follows:

$$\text{cov}_u(x_1, x_2) \approx \frac{1}{m-1} \sum_{i=1}^m (u_i(x_1) - \bar{u}(x_1))(u_i(x_2) - \bar{u}(x_2)),$$

where $x_1, x_2 \in \Omega$ and u, \bar{u} are defined as in $\text{var}_u(x)$. For simplicity, we compute these quantities on the mesh points and exhibit the results in Figure 2. In all of the subfigures in Figure 2, the estimates obtained by the pCN and NF-iVI are drawn in blue solid line and red dashed line, respectively. In Figure 2 (a), we show the variance function calculated on all of the mesh points, i.e., $\{\text{var}_u(x_i)\}_{i=1}^{N_g}$ (N_g is the number of mesh points, which equals to 101 in this problem). In Figure 2 (c) and (e), we show the covariance function calculated on the pairs of points $\{(x_i, x_{i+10})\}_{i=1}^{N_g-10}$ and $\{(x_i, x_{i+20})\}_{i=1}^{N_g-20}$, respectively. Subfigures (a), (b), and (c) in Figure 3 depict the matrix representations of the covariance operators \mathcal{C}_N and \mathcal{C}_p , as well as their difference. Here \mathcal{C}_N represents the covariance operator corresponding to the NF-iVI method, while \mathcal{C}_p represents the covariance operator corresponding to the pCN algorithm. The results confirm that the NF-iVI method provides an accurate estimate of the covariance function.

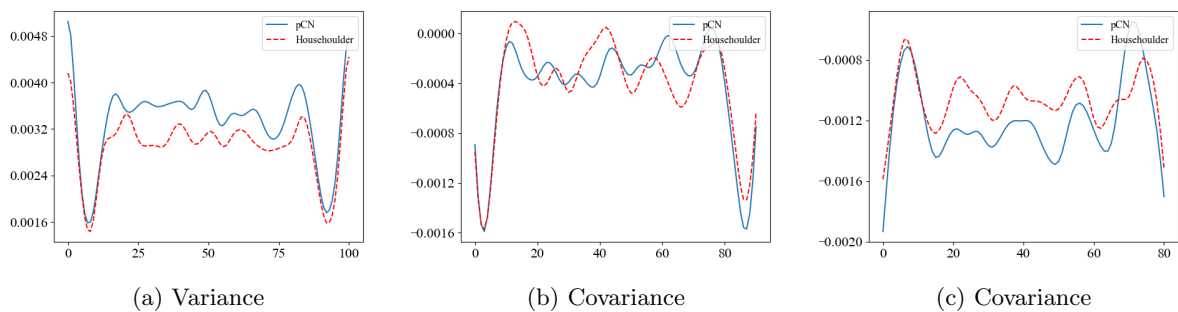


Figure 2: The estimated variance and covariance functions obtained by the pCN algorithm (blue solid line), and NF-iVI algorithm (red dashed line). (a): The covariance function $c(x, y)$ on all the mesh point pairs $\{(x_i, x_i)\}_{i=1}^{N_g}$; (b): The covariance function $c(x, y)$ on the mesh points $\{(x_i, x_{i+10})\}_{i=1}^{N_g-10}$; (c): The covariance function $c(x, y)$ on the mesh points $\{(x_i, x_{i+20})\}_{i=1}^{N_g-20}$.

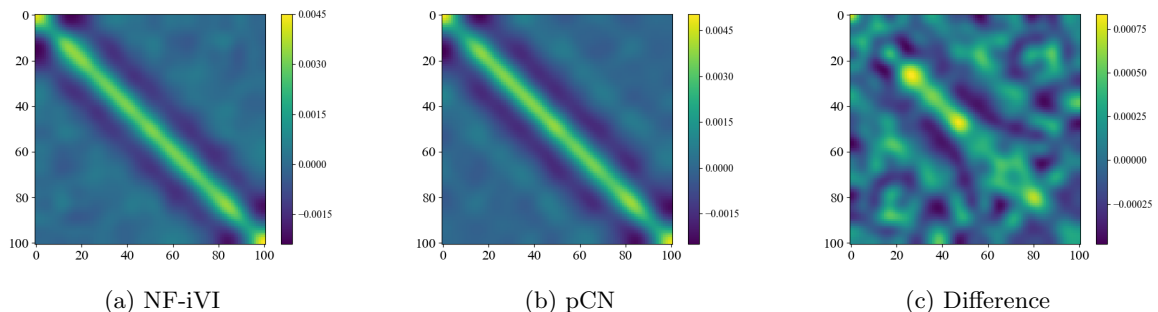


Figure 3: The comparison of covariance obtained by two method. (a): The covariance given by NF-iVI method; (b): The covariance given by the pCN method; (c): The difference between the covariance obtained by NF-iVI and pCN sampling methods.

Then we make numerical comparisons of the variance and covariance functions. We show the relative errors between the variance functions and the covariance functions:

$$\begin{aligned} \text{relative error of variance} &= \frac{\sum_{i=1}^{N_g} (c_N(x_i, x_i) - c_p(x_i, x_i))^2}{\sum_{i=1}^{N_g} (c_p(x_i, x_i))^2}, \\ \text{relative error of covariance} &= \frac{\sum_{i=1}^{N_g-k} (c_N(x_i, x_{i+k}) - c_p(x_i, x_{i+k}))^2}{\sum_{i=1}^{N_g-k} (c_p(x_i, x_{i+k}))^2}, \\ \text{total relative error } \mathbf{c} &= \frac{\sum_{i=1}^{N_g} \sum_{j=1}^{N_g} (c_N(x_i, x_j) - c_p(x_i, x_j))^2}{\sum_{i=1}^{N_g} \sum_{i=1}^{N_g} (c_p(x_i, x_j))^2}, \end{aligned}$$

where k is an integer, $c_p(x, y)$ is the covariance function generated from pCN algorithm, and $c_N(x, y)$ is the covariance function generated from NF-iVI method. The relative errors are shown in Table 1. In the table, the notation \mathbf{c} means the total relative error, and the notation $\{c(x_i, x_{i+k})\}_{i=1}^{N_g-k}$ means the covariance function values on the pair of mesh points $\{(x_i, x_{i+k})\}_{i=1}^{N_g-k}$ ($k = 0, 10, 20$). The numbers below this notation are the relative errors between the vectors obtained by pCN method and NF-iVI, respectively.

As depicted in Table 1, the relative errors are small, indicating that the posterior covariance functions obtained by the NF-iVI and pCN sampling algorithms are quantitatively similar.

Table 1: *The relative errors between variance function, and covariance functions.*

Relative Error	\mathbf{c}	$\{c(x_i, x_i)\}_{i=1}^{N_g}$	$\{c(x_i, x_{i+10})\}_{i=1}^{N_g-10}$	$\{c(x_i, x_{i+20})\}_{i=1}^{N_g-20}$
Householder Flow	0.1081	0.0588	0.0981	0.1593

Additionally, we will leverage this problem to demonstrate the discretization invariance of functional Householder flow. To assess the impact of discretization, we discretize the problem using 50, 75, 100, 200, and 300 grid points in a regular mesh. The final results are shown in Figure 4.

To further validate the discrete invariance of our model, we computed the L^2 -error between the mean functions of the approximate posterior and the true values across various discrete levels. In Table 2, the numbers above are different discrete level we used for NF-iVI, and the numbers below are the relative errors between the means function obtained by NF-iVI and the truth function, respectively. As detailed in Table 2, the L^2 -errors between the mean functions derived from our algorithm and the true values are consistent across different discretizations. Furthermore, Table 3 presents a comparison of the covariance functions of the approximate posterior for several discrete levels. In the table, the numbers above are different discrete level we used for NF-iVI, and the numbers below are the exact values of the covariance function evaluated at the points $(x_1, x_1), (x_1, x_2), (x_1, x_3), (x_2, x_2)$, where $x_1 = 0.3, x_2 = 0.5, x_3 = 0.7$.

Collectively, these findings substantiate the assertion that the approximate posteriors generated by our proposed algorithm are invariant to the different discrete levels.

By integrating the numerical findings presented in Figure 4 and Tables 2 and 3 with the theoretical results established in Theorem 2.10, we have successfully demonstrated the discretization invariance of the functional Householder flow.

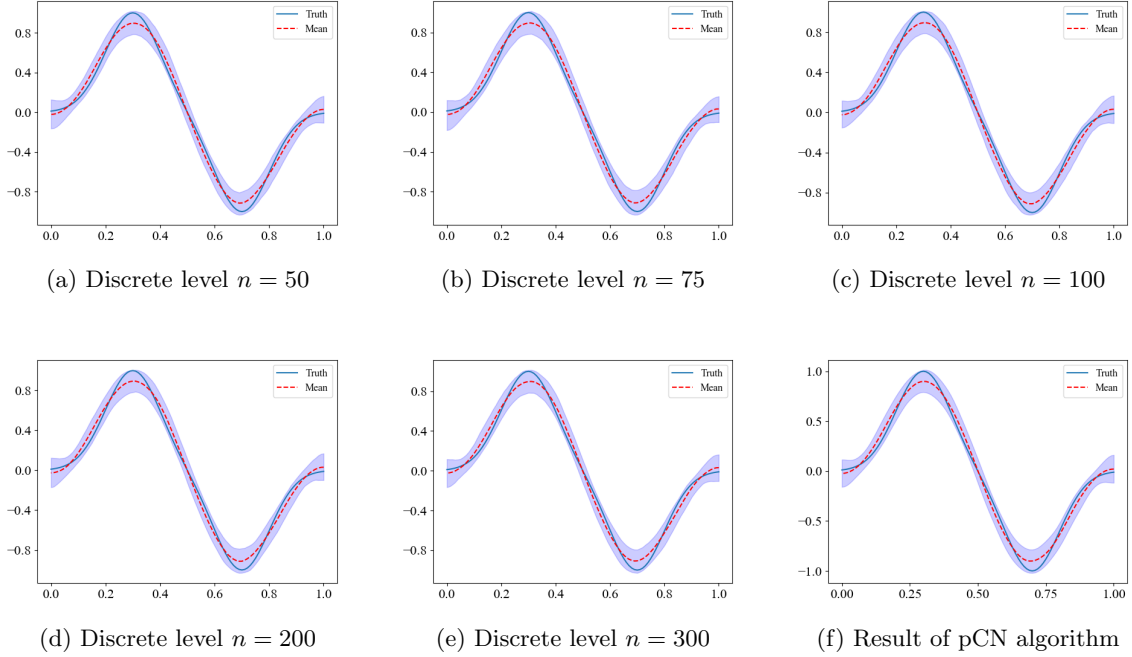


Figure 4: *The comparison of approximate posterior generated by functional Householder flow with different mesh size $n = \{50, 75, 100, 200, 300\}$ respectively. The blue shade area represents the 95% credibility region of approximate posterior.*

Table 2: *The L^2 -errors between the mean of approximate posterior and true function.*

Discrete Level	50	75	100	200	300
L^2 -Error	0.002697	0.002695	0.002755	0.002657	0.002756

Table 3: *The values of covariance function, where $x_1 = 0.3$, $x_2 = 0.5$, $x_3 = 0.7$.*

Discrete Level	50	75	100	200	300
$c(x_1, x_1)$	0.002886	0.003027	0.003010	0.002754	0.002865
$c(x_1, x_2)$	-0.0010431	-0.00107031	-0.000904	-0.0010427	-0.0010700
$c(x_1, x_3)$	0.000227	0.000212	0.000250	0.000225	0.000242
$c(x_2, x_2)$	0.003005	0.002938	0.003371	0.003377	0.003001

4.1.2. Functional Projected Transformation Flow

As discussed in Subsection 2.3, functional projected transformation flows are expected to exhibit superior approximation capabilities compared to functional Householder flows. To demonstrate this, we consider the same inverse problem defined in Equation (4.3). In this experiment, we set the dimension of $\text{Im}(\mathcal{F}_n)$ in the functional projected transformation flow to 20 ($M = 20$

in Subsection 2.4). By employing only five layers of functional projected transformation flow, we achieve satisfactory results in approximating the posterior. In contrast, using five layers of functional Householder flow would be insufficient to achieve similar performance.

To construct the flow models, we utilize five layers for the functional projected transformation flow and explore different configurations with 5, 9, 14, 18, and 21 layers for the functional Householder flow. Following Algorithm 1, all the functional normalizing flow models are trained for 5000 iterations ($K = 5000$) using 30 samples ($N = 30$) in each iteration. The initial learning rate is set to $\alpha_0 = 0.01$, with a step decay learning rate schedule of a multiplicative factor $\tau = 0.8$ after every 500 iterations.

Firstly, we compare the estimated mean of the pCN and NF-iVI methods. In subfigure (a) of Figure 5, we present the results obtained from the 5-layer functional projected transformation flow. We observe that these results are consistent with the posterior generated by the pCN algorithm, as shown in subfigure (b) of Figure 1, indicating the effectiveness of our proposed method. In subfigures (b)-(f) of Figure 5, we present the results obtained from the functional Householder flow with 5, 9, 14, 18, and 21 layers, respectively. We observe that when the number of layers is small, the functional Householder flow may not achieve satisfactory approximations.

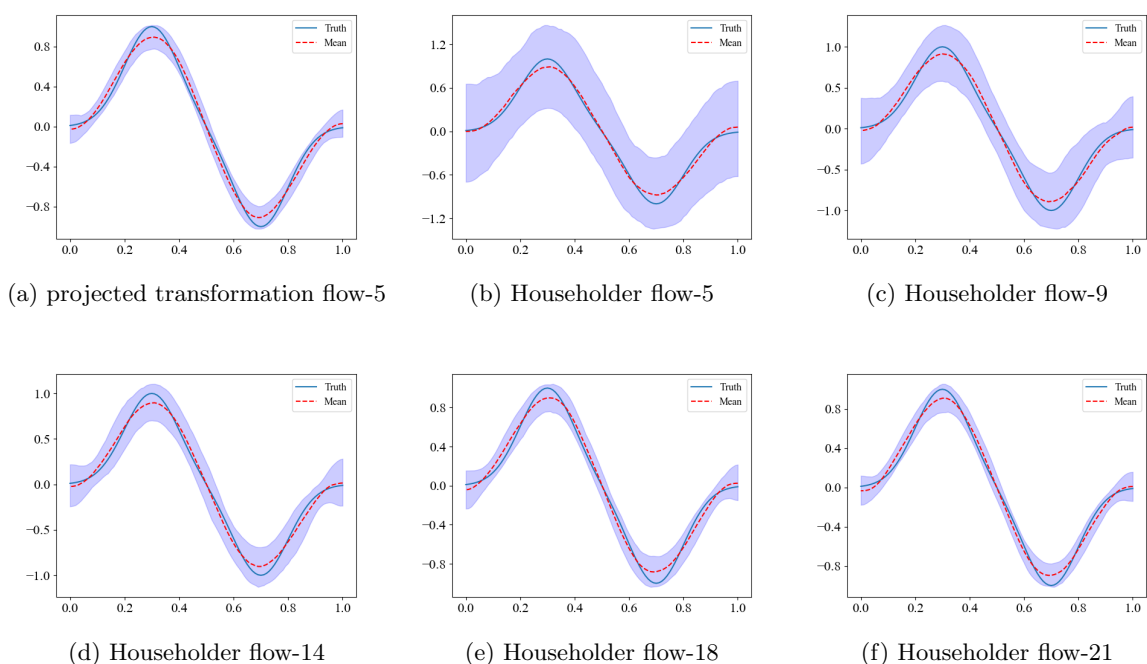


Figure 5: *The comparison of the approximation capabilities of functional Householder flow and functional projected transformation flow. The blue shade area represents the 95% credibility region of approximate posterior. (a): Result of functional projected transformation flow with 5 layers. (b)-(f): Result of functional Householder flow with 5, 9, 14, 18, and 21 layers, respectively.*

Secondly, we compare the variance and covariance functions generated by the two methods. For simplicity, we compute these quantities on the mesh points and present the results in Figure 7. In all the subfigures of Figure 7, the estimated posteriors obtained by the pCN method, the 5-layer functional Householder flow, and the 5-layer projected transformation flow are drawn in blue solid

line, red dashed line, and purple dashed line, respectively. In subfigures (a) and (d) of Figure 7, we show the variance function calculated on all of the mesh points, i.e., $\{\text{var}_u(x_i)\}_{i=1}^{N_g}$ ($N_g = 101$ is the number of mesh points). In subfigures (b) and (e) of Figure 7, we show the covariance function calculated on the pairs of points $\{(x_i, x_{i+10})\}_{i=1}^{N_g-10}$, and in subfigures (c) and (f) of Figure 7, we show the covariance function calculated on the pairs of points $\{(x_i, x_{i+20})\}_{i=1}^{N_g-20}$, respectively. We also show the matrix representations of the covariance operators \mathcal{C}_N and \mathcal{C}_p along with the difference in subfigures (a)-(c) of Figure 6. Here, \mathcal{C}_N is the covariance operator of the approximate posterior generated by the 5-layer projected transformation flow, and \mathcal{C}_p is the covariance operator of the estimated posterior generated by the pCN method. The results confirm that the NF-iVI provides a reliable approximation of the covariance function.

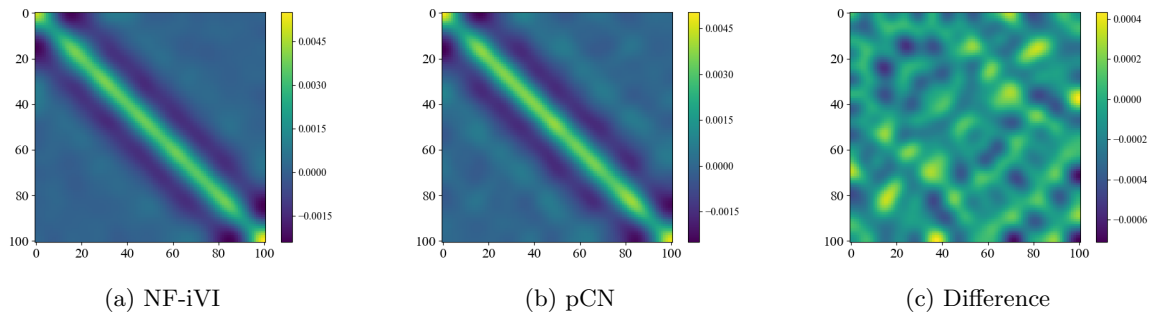


Figure 6: *The comparison of posterior covariance of u with the mesh size $n = 100$ respectively. (a): The covariance given by NF-iVI method; (b): The covariance given by the pCN sampling method; (c): The difference between the covariance obtained by NF-iVI and pCN sampling methods.*

Next, we make numerical comparisons of the variance and covariance functions. We use the 5-layer functional Householder flow and the 5-layer functional projected transformation flow to approximate the posterior, and we show the relative errors of the covariance functions in Table 4. In the table, the notation \mathbf{c} means the total relative error, and the notation $\{c(x_i, x_{i+k})\}_{i=1}^{N_g-k}$ means the covariance function values on the pair of mesh points $\{(x_i, x_{i+k})\}_{i=1}^{N_g-k}$ ($k = 0, 10, 20$). The numbers below this notation are the relative errors between the vectors obtained by pCN method and two different NF-iVI methods, respectively.

Table 4: *The relative errors between the variance function and covariance functions.*

Relative Error	\mathbf{c}	$\{c(x_i, x_i)\}_{i=1}^{N_g}$	$\{c(x_i, x_{i+10})\}_{i=1}^{N_g-10}$	$\{c(x_i, x_{i+20})\}_{i=1}^{N_g-20}$
Householder Flow	1588.736	630.159	12867.031	596.937
Projected Transformation	0.03057	0.00390	0.12691	0.03290

As depicted in Table 4, the relative errors of the 5-layer projected transformation flow are consistently smaller than those of the Householder flow. The variance and covariance functions obtained by the pCN method and the projected transformation flow demonstrate quantitative similarity. This indicates that the 5-layer projected transformation flow exhibits superior performance in approximating the covariance function of the posterior compared to the 5-layer Householder

flow.

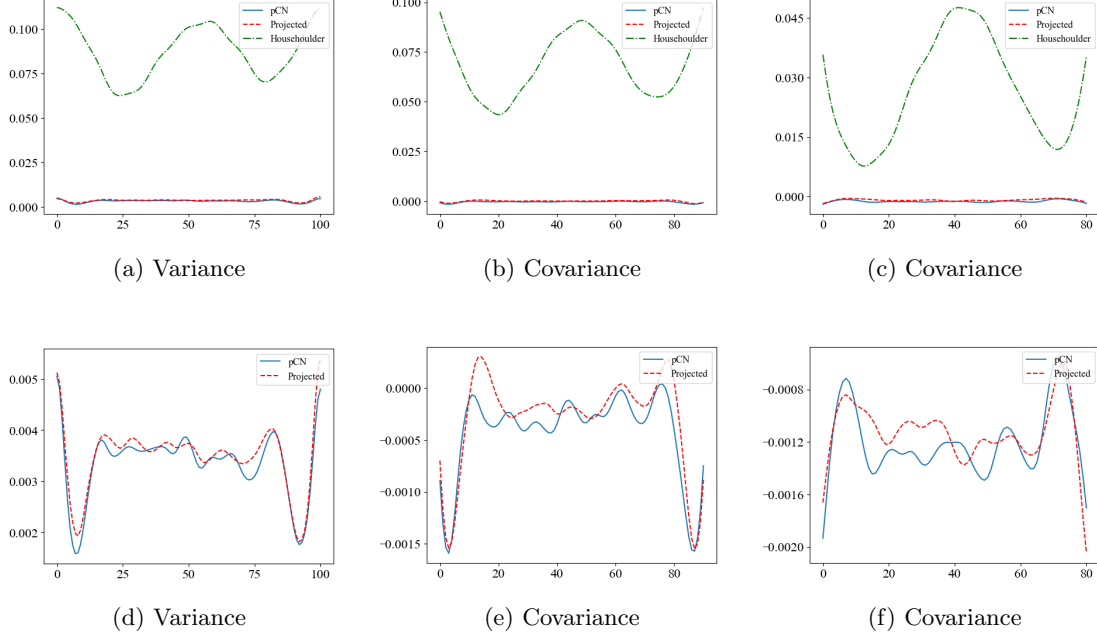


Figure 7: The estimated variance and covariance functions obtained by the pCN method (blue solid line), Householder NF-iVI method (green dashed line) and projected transformation NF-iVI (red dashed line). (a)(d): The covariance function $c(x, y)$ on all the mesh point pairs $\{(x_i, x_i)\}_{i=1}^{N_g}$; (b)(e): The covariance function $c(x, y)$ on the mesh points $\{(x_i, x_{i+10})\}_{i=1}^{N_g-10}$; (c)(f): The covariance function $c(x, y)$ on the mesh points $\{(x_i, x_{i+20})\}_{i=1}^{N_g-20}$.

The comparisons presented above highlight the superior approximation capabilities of the functional projected transformation flow, even when using a small number of layers. To demonstrate the discrete invariance of the functional projected transformation flow, we conduct a similar analysis to that performed for the functional Householder flow. We calculate the L^2 -errors between the mean of the approximate posterior and the true value under different discrete levels. In Table 5, the numbers above are different discrete level we used for NF-iVI, and the numbers below are the relative errors between the means function obtained by NF-iVI and the truth function, respectively. As detailed in Table 5, the L^2 -errors between the mean functions derived from our algorithm and the true values are consistent across different discretizations. As presented in the table, the L^2 -errors between the mean of the approximate posterior and the true value remains consistent across different discrete levels.

Furthermore, Table 6 presents a comparison of the covariance functions of the approximate posterior for several discrete levels. In the table, the numbers above are different discrete level we used for NF-iVI, and the numbers below are the exact values of the covariance function evaluated at the points $(x_1, x_1), (x_1, x_2), (x_1, x_3), (x_2, x_2)$, where $x_1 = 0.3, x_2 = 0.5, x_3 = 0.7$.

4.2. Steady-State Darcy Flow Equation

In this subsection, we focus on the inverse problem of estimating the permeability distribution in a porous medium from a discrete set of pressure measurements, as studied in [11]. Consider the

Table 5: The L^2 -errors between the mean of approximate posterior and true function.

Discreate Level	50	75	100	200	300
L^2 -Error	0.003156	0.003027	0.003117	0.003182	0.003041

Table 6: The values of covariance function, where $x_1 = 0.3$, $x_2 = 0.5$, $x_3 = 0.7$.

Discreate Level	50	75	100	200	300
$c(x_1, x_1)$	0.003670	0.003993	0.003926	0.003626	0.003948
$c(x_1, x_2)$	-0.001043	-0.001158	-0.001165	-0.001062	-0.001011
$c(x_1, x_3)$	0.000289	0.000349	0.000273	0.000207	0.000251
$c(x_2, x_2)$	0.003414	0.003521	0.003545	0.003805	0.003817

following steady-state Darcy flow equation:

$$\begin{aligned} -\nabla \cdot (e^u \nabla w) &= f, & x \in \Omega, \\ w &= 0, & x \in \partial\Omega, \end{aligned} \quad (4.6)$$

where $f \in H^{-1}(\Omega)$ is the source function, and $u \in \mathcal{H}_u := L^\infty(\Omega)$ is called log-permeability for the computational area $\Omega = (0, 1)^2$. The forward operator has the following form:

$$\mathcal{S}\mathcal{G}u = (w(x^1), w(x^2), \dots, w(x^{N_d}))^T,$$

where \mathcal{G} is the PDE solution operator from \mathcal{H}_u to \mathcal{H}_w , \mathcal{S} is the measurement operator from \mathcal{H}_w to \mathbb{R}^{N_d} , and $x^i \in \Omega$ for $i = 1, \dots, N_d$. With these notations, the problem can be written abstractly as:

$$\mathbf{d} = \mathcal{S}\mathcal{G}u + \boldsymbol{\epsilon}, \quad (4.7)$$

where $\boldsymbol{\epsilon} \sim \mathcal{N}(0, \boldsymbol{\Gamma}_{\text{noise}})$ is the random Gaussian noise, and \mathbf{d} is the measurement data.

In our experiments, the prior measure of u is a Gaussian probability measure μ_0 with mean zero and covariance \mathcal{C}_0 . For clarity, we list the specific choices for some parameters introduced in this subsection as follows:

- Assume that 5% random Gaussian noise $\boldsymbol{\epsilon} \sim \mathcal{N}(0, \boldsymbol{\Gamma}_{\text{noise}})$ is added, where $\boldsymbol{\Gamma}_{\text{noise}} = \tau^{-1} \mathbf{I}$, and $\tau^{-1} = (0.05 \|\mathcal{S}\mathcal{G}u\|_\infty)^2$.
- We assume that the data is produced from the underlying log-permeability:
$$u^\dagger = \exp(-20(x_1 - 0.3)^2 - 20(x_2 - 0.3)^2) + \exp(-20(x_1 - 0.7)^2 - 20(x_2 - 0.7)^2).$$
- Let the domain Ω be a bounded area $(0, 1)^2$. The measurement points $\{x^i\}_{i=1}^{N_d}$ are taken at the coordinates $\{\frac{i}{21}, \frac{j}{21}\}_{i,j=1}^{20}$.
- The operator \mathcal{C}_0 is given by $\mathcal{C}_0 = (\mathbf{I} - \alpha \Delta)^{-2}$, where $\alpha = 0.1$ is a fixed constant. Here, the Laplace operator is defined on Ω with zero Neumann boundary condition.

- To avoid the inverse crime, a fine mesh with the number of grid points equal to 500×500 is employed for generating the data. For the inversion, a mesh with a number of grid points equal to 20×20 is employed.

4.2.1. Functional Planar Flow

Given the nonlinear nature of the inverse problem, we employ a functional planar flow model to approximate the posterior distribution, constructing it with 24 layers. Following Algorithm 1, the functional planar flow is trained over 5000 iterations ($K = 5000$), with each iteration utilizing 30 samples ($N = 30$). We utilize a step decay learning rate schedule, starting with an initial learning rate of $\alpha_0 = 0.01$ and decreasing it by a multiplicative factor of $\tau = 0.8$ after every 500 iterations. For comparison, we also present the posterior generated by the pCN algorithm. In the discussion of all steady-state darcy flow problems, when we discuss ESS, the corresponding functional f is defined as $f(u) = u((0.5, 0.5))$. We generate 3×10^6 samples using the pCN algorithm, achieving an effective sample size of $\text{ESS}_p = 278$.

Firstly, in Figure 8, we present a comparative analysis of the mean function generated by the pCN algorithm and the approximate posterior obtained from functional planar flow. We observe that the mean of the approximate posterior closely resembles the ground truth, as shown in subfigures (a) and (b). Additionally, subfigures (d) and (e) of Figure 8 illustrate the mean function of the estimated posterior generated by the pCN algorithm. The similarity between these results further demonstrates the effectiveness of our proposed method in accurately estimating the mean function.

To further support the effectiveness of the NF-iVI method in estimating the mean function, we provide numerical evidence. The relative error between the mean of the approximate posterior u_N^* and the mean of the posterior u_p^* is given by:

$$\text{relative error} = \frac{\|u_N^* - u_p^*\|^2}{\|u_p^*\|^2} = 0.00124. \quad (4.8)$$

The estimated value is small, indicating the effectiveness of our algorithm.

Combining the visual evidence from Figure 8 and the numerical evidence provided by the relative error in (4.8), we conclude that the NF-iVI method effectively approximates the mean of the posterior.

Secondly, to further explore the approximate posterior, we analyze the covariance functions. In subfigure (c) of Figure 8, we present the point-wise variance field of the posterior measure obtained from the NF-iVI method. For comparison, subfigure (f) of Figure 8 depicts the point-wise variance field estimated using the pCN method. The similarity between these two plots indicates the effectiveness of the NF-iVI method in quantifying the uncertainties of the parameter u .

We also compare the covariance functions generated by these two methods. For simplicity, we compute these quantities at the mesh points and present the results in Figure 9. In all subfigures of Figure 9, the estimated covariance of posteriors obtained by the pCN and NF-iVI methods are represented by a blue solid line and a red dashed line, respectively. In subfigure (a) of Figure 9, we show the variance function calculated at all mesh points, i.e., $\{\text{var}_u(x_i)\}_{i=1}^{N_g}$ (N_g is the number of mesh points, which is 441 in this problem). In subfigures (c) and (e) of Figure 9, we show the covariance functions calculated on the pairs of points $\{(x_i, x_{i+40})\}_{i=1}^{N_g-40}$ and $\{(x_i, x_{i+80})\}_{i=1}^{N_g-80}$, respectively.

To numerically compare the variance and covariance functions generated by the two methods, we present the relative errors in Table 7. In the table, the notation \mathbf{c} means the total relative error,

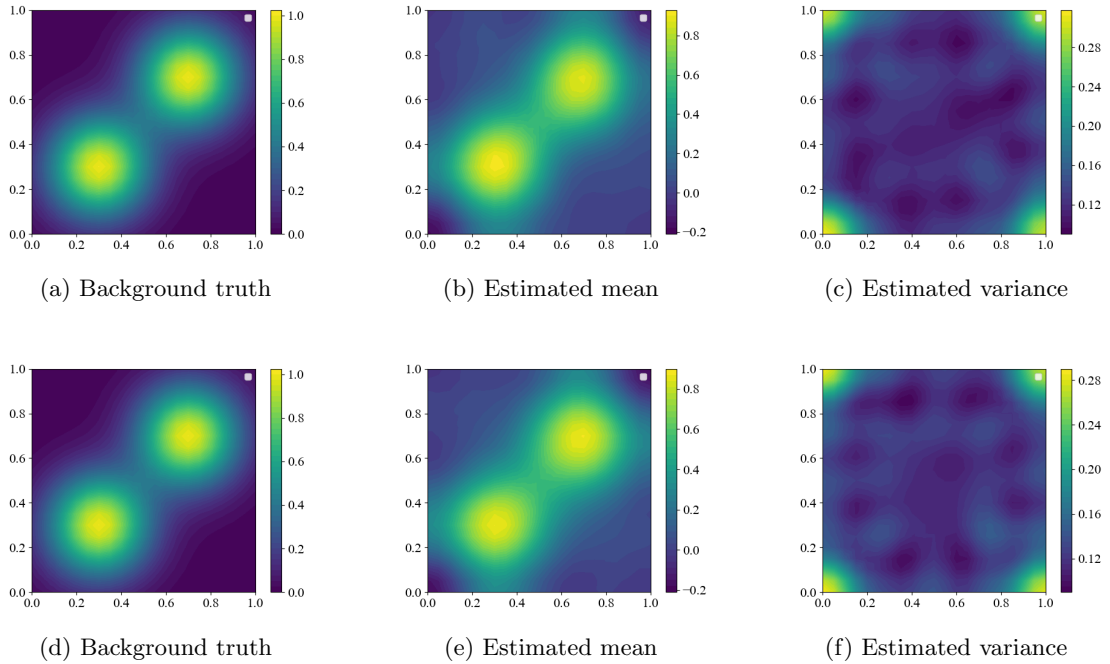


Figure 8: *The comparison of the approximate posterior obtained by functional planar flow with 24 layers and the background truth. (a)(d): The background truth of u . (b): The mean of approximate posterior obtained by functional planar flow with 24 layers. (c): The variance function of approximate posterior obtained by functional planar flow with 24 layers. (e): The mean function of posterior obtained by pCN algorithm. (f): The variance function of posterior obtained by pCN algorithm.*

and the notation $\{c(x_i, x_{i+k})\}_{i=1}^{N_g-k}$ means the covariance function values on the pair of mesh points $\{(x_i, x_{i+k})\}_{i=1}^{N_g-k}$ ($k = 0, 40, 80$). The numbers below this notation are the relative errors between the vectors obtained by pCN method and NF-iVI, respectively. The small relative errors indicate that the posterior covariance functions obtained by the NF-iVI and pCN sampling methods are quantitatively similar. Combining the visual evidence from Figures 8 and 9, and the numerical evidence from Table 7, we conclude that the NF-iVI method effectively approximates the covariance function of the posterior.

Table 7: *The relative errors between the variance function and covariance functions.*

Relative Error	\mathbf{c}	$\{c(x_i, x_i)\}_{i=1}^{N_g}$	$\{c(x_i, x_{i+40})\}_{i=1}^{N_g-40}$	$\{c(x_i, x_{i+80})\}_{i=1}^{N_g-80}$
planar	0.12252	0.03424	0.11531	0.16419

To demonstrate the discrete invariance of functional planar flow, we assess the impact of discretization by employing different grid sizes: 15×15 , 20×20 , 30×30 , 40×40 , and 50×50 points in a regular mesh. We calculate the L^2 -errors between the mean of the approximate posterior and the true value under these varying discrete levels. As presented in Table 8, the L^2 -errors remains consistent across different discrete levels. Additionally, Table 9 compares the values of the covariance function of the approximate posterior for various discrete levels, revealing a similar pattern. These

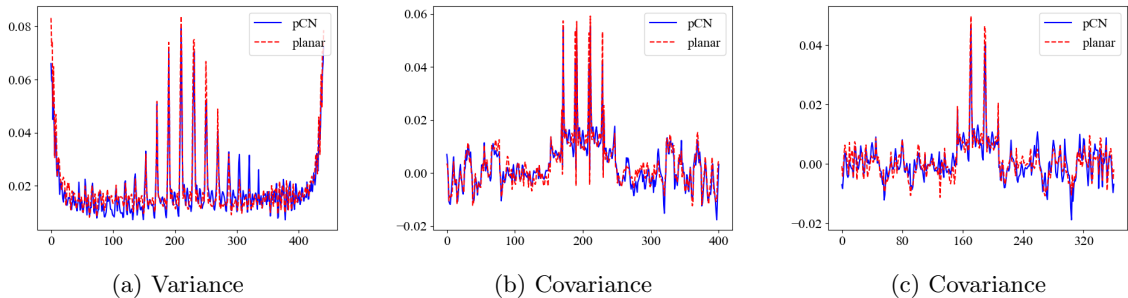


Figure 9: The estimated variance and covariance functions obtained by the pCN algorithm (blue solid line), and NF-iVI algorithm (red dashed line). (a): The covariance function $c(x, y)$ on all the mesh point pairs $\{(x_i, x_i)\}_{i=1}^{N_g}$; (b): The covariance function $c(x, y)$ on the mesh points $\{(x_i, x_{i+40})\}_{i=1}^{N_g-40}$; (c): The covariance function $c(x, y)$ on the mesh points $\{(x_i, x_{i+80})\}_{i=1}^{N_g-80}$.

results collectively support the claim that the approximate posteriors obtained by our algorithm are invariant to different discretizations.

Table 8: The L^2 -errors between the mean of approximate posterior and true function.

Discrete Level	15×15	20×20	30×30	40×40	50×50
L^2 -Error	0.009620	0.008446	0.007645	0.007913	0.008027

Table 9: The values of covariance function, where $x_1 = (0.3, 0.3)$, $x_2 = (0.5, 0.5)$, $x_3 = (0.7, 0.7)$.

Discrete Level	15×15	20×20	30×30	40×40	50×50
$c(x_1, x_1)$	0.015079	0.016000	0.014736	0.015205	0.015848
$c(x_1, x_2)$	-0.004403	-0.004122	-0.004202	-0.004557	-0.455003
$c(x_1, x_3)$	0.004367	0.004269	0.004529	0.004891	0.004290
$c(x_2, x_2)$	0.015369	0.014359	0.013761	0.014083	0.013925

4.2.2. Functional Sylvester Flow

As discussed in Subsection 2.4, the functional Sylvester flow is anticipated to exhibit superior approximation capabilities compared to the functional planar flow. To demonstrate this, we consider the same inverse problem defined in (4.7). In this experiment, we set the dimension of $\text{Im}(\mathcal{F}_n)$ in the functional Sylvester flow to 20 ($M = 20$ in Subsection 2.4). By employing only five layers of functional Sylvester flow, we achieve satisfactory results in approximating the posterior. In contrast, using five layers of functional planar flow would be insufficient to achieve similar performance.

We utilize five layers for both functional Sylvester flow and functional planar flow. Following Algorithm 1, all of the functional normalizing flow models are trained for 5000 iterations ($K =$

5000), using 30 samples ($N = 30$) in each iteration, with an initial learning rate of $\alpha_0 = 0.01$. The learning rate follows a step decay schedule with a multiplicative factor of $\tau = 0.8$ after every 500 iterations.

In subfigures (a) and (d) of Figure 10, we present the ground truth. Subfigures (b), (c), (e), and (f) of Figure 10 depict the mean function and the estimated point-wise variance field of the approximate posterior obtained from the 5-layer functional Sylvester flow. We observe that these results are consistent with those of the pCN algorithm shown in subfigures (e) and (f) of Figure 8, demonstrating the effectiveness of our approach.

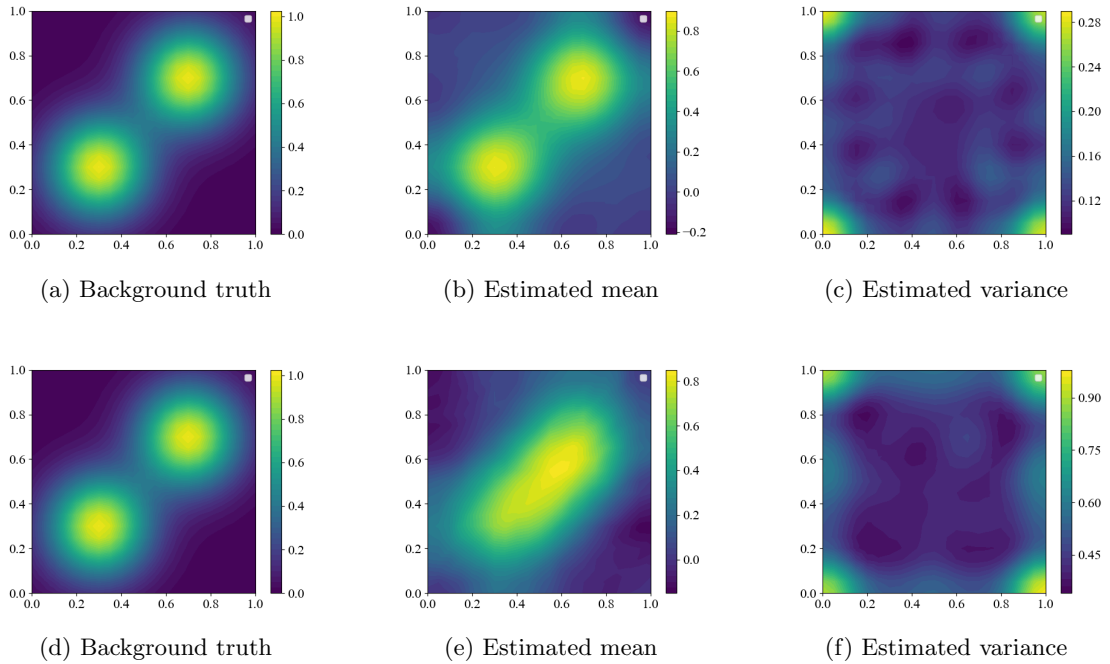


Figure 10: *The comparison of approximation ability between functional planar flow and functional Sylvester flow. We use 5 layers for both flow models to approximate the posterior. (a)(d): The background truth of u . (b): The mean of approximate posterior obtained by functional Sylvester flow. (c): The variance function of approximate posterior obtained by functional Sylvester flow. (e): The mean function of approximate posterior obtained by functional planar flow. (f): The variance function of approximate posterior obtained by functional planar flow.*

We also compare the variance and covariance functions generated by these two methods. We compute these quantities at the mesh points and present the results in Figure 11. In all subfigures of Figure 11, the estimates obtained by the pCN, functional planar flow, and functional Sylvester flow are drawn in blue solid line, orange solid line, and red dashed line, respectively. In subfigures (a) and (d) of Figure 11, we show the variance function calculated at all mesh points, i.e., $\{\text{var}u(x_i)\}_{i=1}^{N_g}$ ($N_g = 441$ being the number of mesh points). In subfigures (b) and (e) of Figure 11, we show the covariance functions calculated on pairs of points $\{(x_i, x_{i+40})\}_{i=1}^{N_g-40}$. Finally, in subfigures (c) and (f) of Figure 11, we show the covariance functions calculated on pairs of points $\{(x_i, x_{i+80})\}_{i=1}^{N_g-80}$.

To numerically compare the variance and covariance functions, we employ the 5-layer functional

planar flow and the 5-layer functional Sylvester flow to approximate the posterior. The relative errors between the variance functions and the covariance functions are presented in Table 10. As depicted in the table, the relative errors of functional Sylvester flow are consistently smaller than those of functional planar flow. Moreover, the variance and covariance functions obtained by the pCN method and functional Sylvester flow demonstrate quantitative similarity. This indicates that the 5-layer functional Sylvester flow exhibits superior performance in approximating the covariance function of the posterior compared to the 5-layer functional planar flow.

Table 10: *The relative errors between the variance function and covariance functions.*

Relative Error	\mathbf{c}	$\{c(x_i, x_i)\}_{i=1}^{N_g}$	$\{c(x_i, x_{i+40})\}_{i=1}^{N_g-40}$	$\{c(x_i, x_{i+80})\}_{i=1}^{N_g-80}$
planar	206.804	155.946	161.661	174.727
Sylvester	0.11846	0.05066	0.08278	0.15118

The comparisons presented above highlight the limitations of functional planar flow in achieving accurate approximations with a small number of layers. In contrast, functional Sylvester flow exhibits superior approximation capabilities.

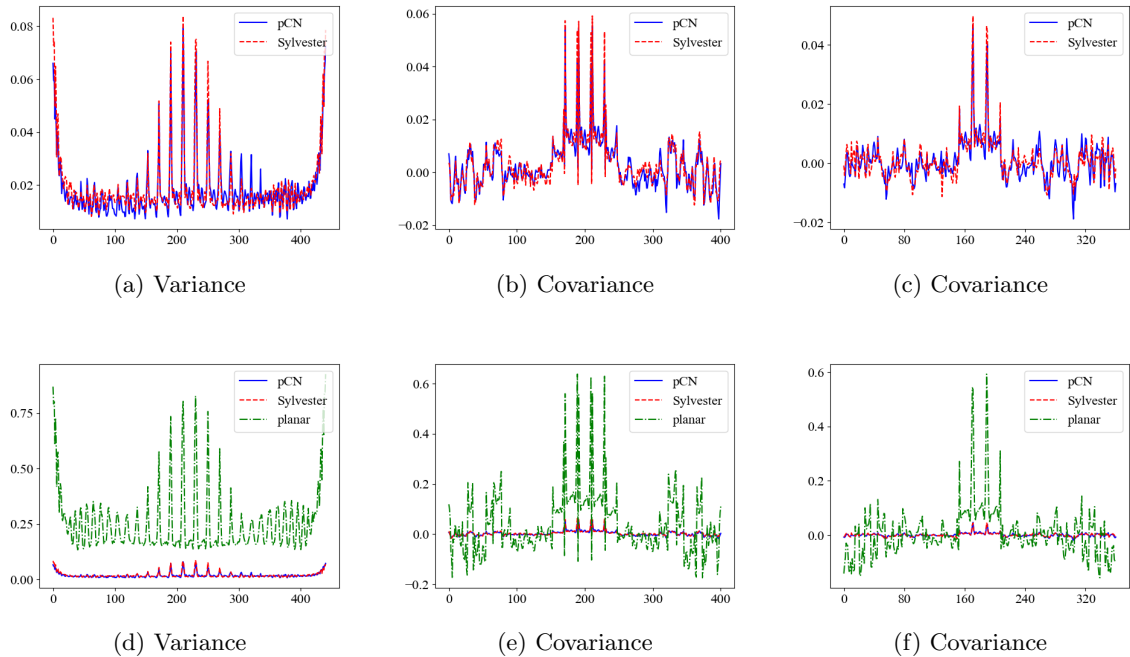


Figure 11: *The estimated variance and covariance functions obtained by the pCN method (blue solid line), planar NF-iVI method (green dashed line) and Sylvester NF-iVI (red dashed line). (a)(d): The covariance function $c(x, y)$ on all the mesh point pairs $\{(x_i, x_i)\}_{i=1}^{N_g}$; (b)(e): The covariance function $c(x, y)$ on the mesh points $\{(x_i, x_{i+40})\}_{i=1}^{N_g-40}$; (c)(f): The covariance function $c(x, y)$ on the mesh points $\{(x_i, x_{i+80})\}_{i=1}^{N_g-80}$.*

Next, we demonstrate the discrete invariance of functional Sylvester flow. We calculate the L^2 -errors between the mean of the approximate posterior and the true value under different discrete

levels. As presented in Table 11, the L^2 -errors remains consistent across different discrete levels. Additionally, Table 12 compares the values of the covariance function of the approximate posterior for various discrete levels, revealing a similar pattern. These results collectively support the claim that the approximate posteriors obtained by functional Sylvester flow are invariant to different discretizations.

Table 11: *The L^2 -errors between the mean of approximate posterior and true function.*

Discrete Level	15×15	20×20	30×30	40×40	50×50
L^2 -Error	0.005291	0.005371	0.005293	0.005355	0.005166

Table 12: *The values of covariance function, where $x_1 = (0.3, 0.3)$, $x_2 = (0.5, 0.5)$, $x_3 = (0.7, 0.7)$.*

Discrete Level	15×15	20×20	30×30	40×40	50×50
$c(x_1, x_1)$	0.015359	0.014409	0.014562	0.015302	0.014819
$c(x_1, x_2)$	-0.004174	-0.004598	-0.004539	-0.004566	-0.004515
$c(x_1, x_3)$	0.002194	0.001694	0.002079	0.001887	0.001986
$c(x_2, x_2)$	0.013898	0.013539	0.013355	0.013778	0.013336

5. Numerical Examples of Conditional Functional Normalizing Flow

In this section, we present the results of the conditional functional normalizing flow, as detailed in Subsection 3. For a given measurement information pair $(\mathbf{x}^*, \mathbf{d}^*)$, the trained network $\mathcal{N}_\lambda(\mathbf{v})$ can efficiently provides a rough estimate of its corresponding posterior distribution $\mu_{(\mathbf{x}^*, \mathbf{d}^*)}$. Additionally, for a specific measurement information pair, we can refine the results through a retraining process.

5.1. Conditional Functional Normalizing Flow

In this subsection, we demonstrate the process of training the conditional network and obtaining an initial rough approximation of the posterior distribution directly from the trained network. We focus on the inverse problem of estimating the permeability distribution in a porous medium from a discrete set of pressure measurements, as studied in [11]. Considering the steady-state Darcy flow equation (4.6), the primary objective of the inverse problem is to infer the possible values of the parameter u based on the measurement data $\mathbf{d} = (w(x^1), w(x^2), \dots, w(x^{N_d}))$ at the measurement points $\mathbf{x} = (x^1, x^2, \dots, x^{N_d})$ of the solution w . To approximate the posterior distribution, we employ a 5-layer functional Sylvester flow similar to the approach described in Subsection 4.2. To effectively train the conditional network, we generate the training dataset according to the following process:

- Draw a large number of samples from the prior μ_0 , denoted as $\{u_1, u_2, \dots, u_{N_{train}}\}$.

- Use these samples as parameters for the PDE equation (4.6), and generate their corresponding solutions $\{w_1, w_2, \dots, w_{N_{train}}\}$.
- Determine the measurement points $\{\mathbf{x}_1, \mathbf{x}_2, \dots, \mathbf{x}_{N_{train}}\}$ for each solution and calculate their corresponding measurement data $\{\mathbf{d}_1, \mathbf{d}_2, \dots, \mathbf{d}_{N_{train}}\}$.
- Combine the measurement points and data into pairs $(\mathbf{x}_i, \mathbf{d}_i)$ and form the training dataset $D_{train} = \{(\mathbf{x}_1, \mathbf{d}_1), (\mathbf{x}_2, \mathbf{d}_2), \dots, (\mathbf{x}_{N_{train}}, \mathbf{d}_{N_{train}})\}$.

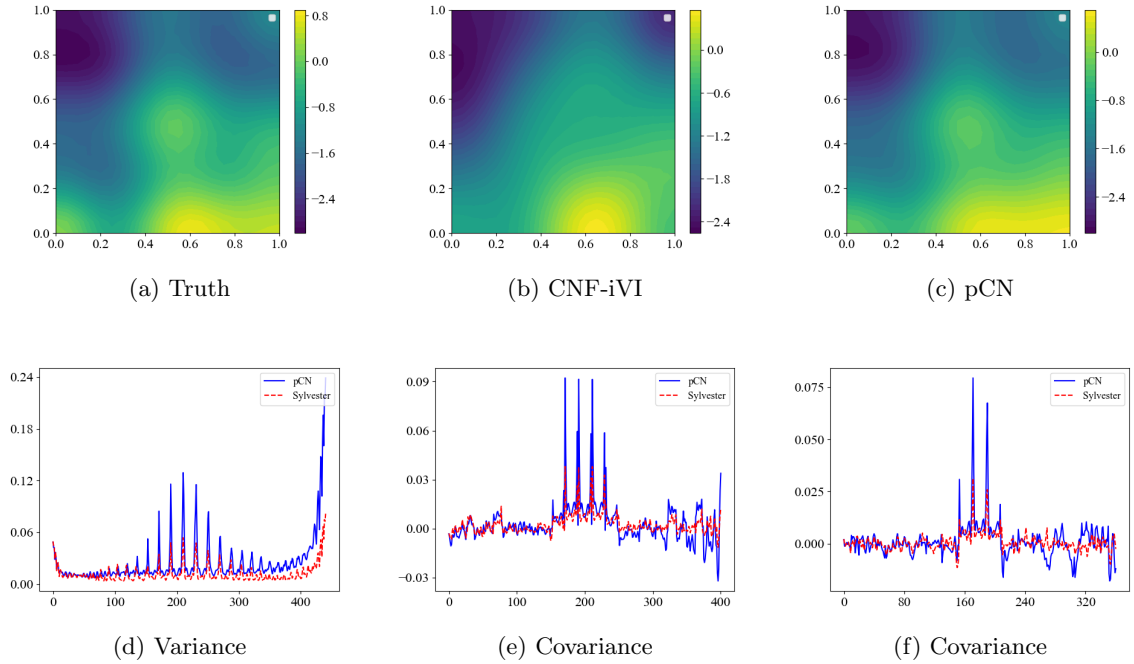


Figure 12: *The comparison of the approximate posterior obtained by CNF-iVI method and the pCN method. The estimated variance and covariance functions obtained by the pCN algorithm are drawn in blue solid line, and by CNF-iVI algorithm the red dashed line. (a): The background truth of u . (b): The mean of approximate posterior obtained by CNF-iVI method. (c): The mean of posterior obtained by pCN method. (d): The covariance function $c(x, y)$ on all the mesh point pairs $\{(x_i, x_i)\}_{i=1}^{N_g}$; (e): The covariance function $c(x, y)$ on the mesh points $\{(x_i, x_{i+40})\}_{i=1}^{N_g-40}$; (f): The covariance function $c(x, y)$ on the mesh points $\{(x_i, x_{i+80})\}_{i=1}^{N_g-80}$.*

Here, we briefly describe the symbols used in this context. The vector $\mathbf{x} = (x^1, x^2, \dots, x^{N_d})$ represents the measurement points, where each $x^i \in \Omega$ corresponds to a distinct measurement point. The notation \mathbf{x}_j refers to different measurement points associated with different measurement pairs $(\mathbf{x}_j, \mathbf{d}_j)$. For convenience, we select the measurement points $\mathbf{x}_1, \mathbf{x}_2, \dots, \mathbf{x}_{N_{train}}$ within a bounded domain Ω , which is defined as the region $(0, 1)^2$. These points are uniformly distributed across this domain, with coordinates given by $\{(\frac{i}{21}, \frac{j}{21})\}_{i,j=1}^{20}$.

Next, we introduce the training dataset D_{train} into Algorithm 2 for training. We set $M = 10$ and $N_u = 20$, with the number of training steps $K = 50000$ in Algorithm 2. The initial learning rate is set to $\alpha_0 = 0.001$, following a step decay learning rate schedule with a multiplicative factor

of $\tau = 0.95$ after every 1000 iterations. To evaluate the performance of the trained model, we generate a test dataset $D_{test} = \{(\mathbf{x}_1, \mathbf{d}_1), (\mathbf{x}_2, \mathbf{d}_2), \dots, (\mathbf{x}_{N_{test}}, \mathbf{d}_{N_{test}})\}$ with $N_{test} = 100$, following the same data generation process used for the training dataset D_{train} . For each pair $(\mathbf{x}_i, \mathbf{d}_i)$ in the test dataset D_{test} , we can calculate the corresponding approximate posterior $\nu_\lambda(\mathbf{v}_i)$ directly from the trained conditional network $\mathcal{N}_\lambda(\mathbf{v})$.

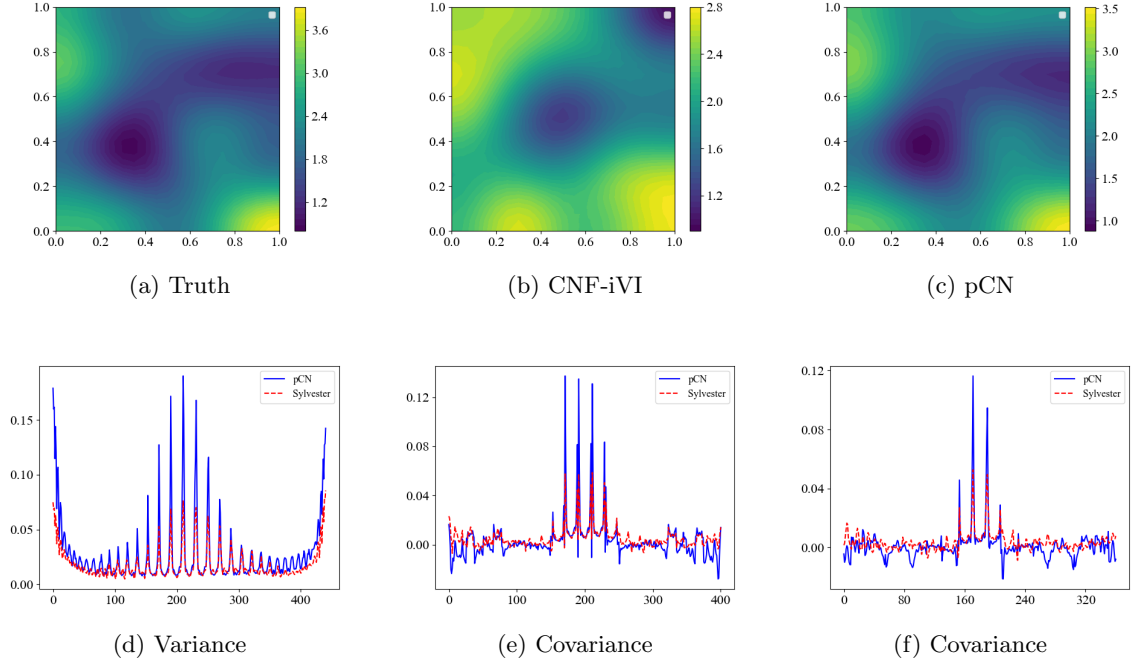


Figure 13: *The comparison of the approximate posterior obtained by CNF-iVI method and the pCN method. The estimated variance and covariance functions obtained by the pCN algorithm are drawn in blue solid line, and by CNF-iVI algorithm the red dashed line. (a): The background truth of u . (b): The mean of approximate posterior obtained by CNF-iVI method. (c): The mean of posterior obtained by pCN method. (d): The covariance function $c(x, y)$ on all the mesh point pairs $\{(x_i, x_i)\}_{i=1}^{N_g}$; (e): The covariance function $c(x, y)$ on the mesh points $\{(x_i, x_{i+40})\}_{i=1}^{N_g-40}$; (f): The covariance function $c(x, y)$ on the mesh points $\{(x_i, x_{i+80})\}_{i=1}^{N_g-80}$.*

Next, we compare the approximate posteriors obtained from the conditional network with the results generated by the pCN algorithm. For each pCN algorithm, we perform 3×10^6 sampling iterations. Due to the high computational cost of the pCN algorithm, we limit our comparison to the posteriors corresponding to three examples in test dataset. The ESS of the pCN samples of these three examples are $ESS_{p_1} = 267$, $ESS_{p_2} = 231$, and $ESS_{p_3} = 258$, respectively.

The conditional network provides a rough estimate, leading to a significant discrepancy between the mean of the approximate posterior and the mean of the true posterior. Consequently, the covariance function generated by the conditional network also significantly differs from the true posterior covariance. In the next subsection, we will present the results obtained after retraining the model using the same test dataset.

Figures 12, 13, and 14 present qualitative results of the approximate posterior inferred using the trained conditional network $\mathcal{N}_\lambda(\mathbf{v})$ for three different measurement information sets. To further

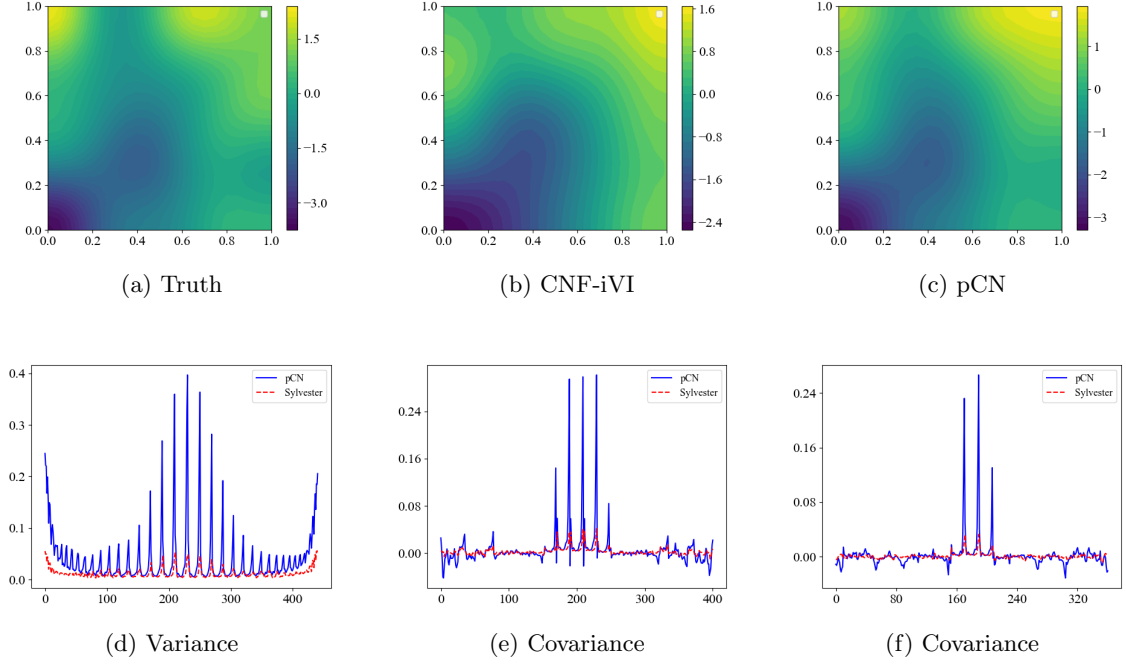


Figure 14: *The comparison of the approximate posterior obtained by CNF-iVI method and the pCN method. The estimated variance and covariance functions obtained by the pCN algorithm are drawn in blue solid line, and by CNF-iVI algorithm the red dashed line. (a): The background truth of u . (b): The mean of approximate posterior obtained by CNF-iVI method. (c): The mean of posterior obtained by pCN method. (d): The covariance function $c(x, y)$ on all the mesh point pairs $\{(x_i, x_i)\}_{i=1}^{N_g}$; (e): The covariance function $c(x, y)$ on the mesh points $\{(x_i, x_{i+40})\}_{i=1}^{N_g-40}$; (f): The covariance function $c(x, y)$ on the mesh points $\{(x_i, x_{i+80})\}_{i=1}^{N_g-80}$.*

quantitatively assess the effectiveness of the CNF-iVI method, we calculate the re-simulation error:

$$\begin{aligned}
\text{re-simulation error} &= E_{(\mathbf{x}, \mathbf{d})} (E_{\nu_{\lambda}(\mathbf{v}(\mathbf{x}, \mathbf{d}))} \|\mathcal{S}\mathcal{G}(u) - \mathcal{S}\mathcal{G}(u_{\text{truth}}^{(\mathbf{x}, \mathbf{d})})\|) \\
&\approx \frac{1}{N_{\text{test}} N_{\text{samples}}} \sum_{i=1}^{N_{\text{test}}} \sum_{j=1}^{N_{\text{samples}}} \|\mathcal{S}\mathcal{G}(u_{ij}) - \mathcal{S}\mathcal{G}(u_{\text{truth}}^{(\mathbf{x}_i, \mathbf{d}_i)})\| \quad (5.1) \\
&= 0.10834.
\end{aligned}$$

where $u_{\text{truth}}^{(\mathbf{x}, \mathbf{d})}$ represents the ground truth and $\mathbf{v}^{(\mathbf{x}, \mathbf{d})}$ denotes the vector corresponding to the measurement information (\mathbf{x}, \mathbf{d}) . We set $N_{\text{samples}} = 500$ for the evaluation.

The visual evidence presented in Figures 12, 13, and 14, combined with the quantitative results from the re-simulation error in (5.1), demonstrates the effectiveness of our proposed method in roughly capturing the properties of the true posterior, conditioned on the measurement information (\mathbf{x}, \mathbf{d}) . This highlights the efficiency of conditional functional normalizing flow in roughly inferring the posterior distribution.

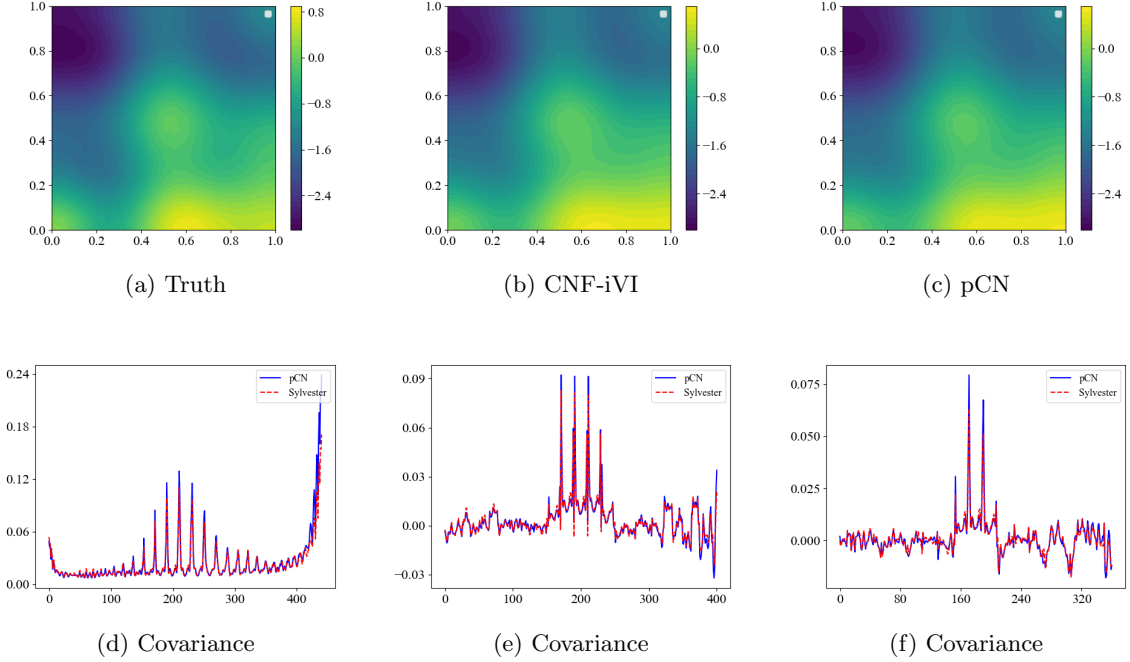


Figure 15: *The comparison of the approximate posterior obtained by retrained NF-iVI method and the pCN method. The estimated variance and covariance functions obtained by the pCN algorithm are drawn in blue solid line, and by retrained NF-iVI algorithm the red dashed line. (a): The background truth of u . (b): The mean of approximate posterior obtained by retrained NF-iVI method. (c): The mean of posterior obtained by pCN method. (d): The covariance function $c(x,y)$ on all the mesh point pairs $\{(x_i, x_i)\}_{i=1}^{N_g}$; (e): The covariance function $c(x,y)$ on the mesh points $\{(x_i, x_{i+40})\}_{i=1}^{N_g-40}$; (f): The covariance function $c(x,y)$ on the mesh points $\{(x_i, x_{i+80})\}_{i=1}^{N_g-80}$*

5.2. Further Training for Specific Data

For the inverse problem corresponding to specific measurement information, we can refine the approximate posterior obtained from the trained conditional network $\mathcal{N}_\lambda(\mathbf{v})$ using a retraining method (Algorithm 3). For the test dataset $\{(\mathbf{x}_1, \mathbf{d}_1), (\mathbf{x}_2, \mathbf{d}_2), \dots, (\mathbf{x}_{N_{test}}, \mathbf{d}_{N_{test}})\}$ used in Subsection 5.1, we convert each pair $(\mathbf{x}_i, \mathbf{d}_i)$ into its corresponding vector \mathbf{v}_i . These vectors are then input into the trained neural network $\mathcal{N}_\lambda(\mathbf{v})$ to obtain initial approximations $\{\nu_\lambda(\mathbf{v}_1), \nu_\lambda(\mathbf{v}_2), \dots, \nu_\lambda(\mathbf{v}_{N_{test}})\}$ of the posterior distributions. Subsequently, we refine these approximate posteriors by retraining them using Algorithm 3, resulting in a new set of refined posteriors $\{\hat{\nu}_1, \hat{\nu}_2, \dots, \hat{\nu}_{N_{test}}\}$.

We use Adam to retrain the approximate posterior. Following Algorithm 3, the functional Sylvester flow is retrained for 1000 iterations ($K = 1000$) using 30 samples ($N = 30$) in each iteration, with an initial learning rate of $\alpha_0 = 0.001$. The learning rate follows a step decay schedule with a multiplicative factor of $\tau = 0.9$ after every 200 iterations.

Figures 15, 16, and 17 present the results obtained from retraining the initial outputs from the trained conditional functional normalizing flow in Subsection 5.1. These inverse problems correspond to the same scenarios depicted in Figures 12, 13, and 14, respectively. We use the results from the trained conditional functional normalizing flow as initial values and retrain the

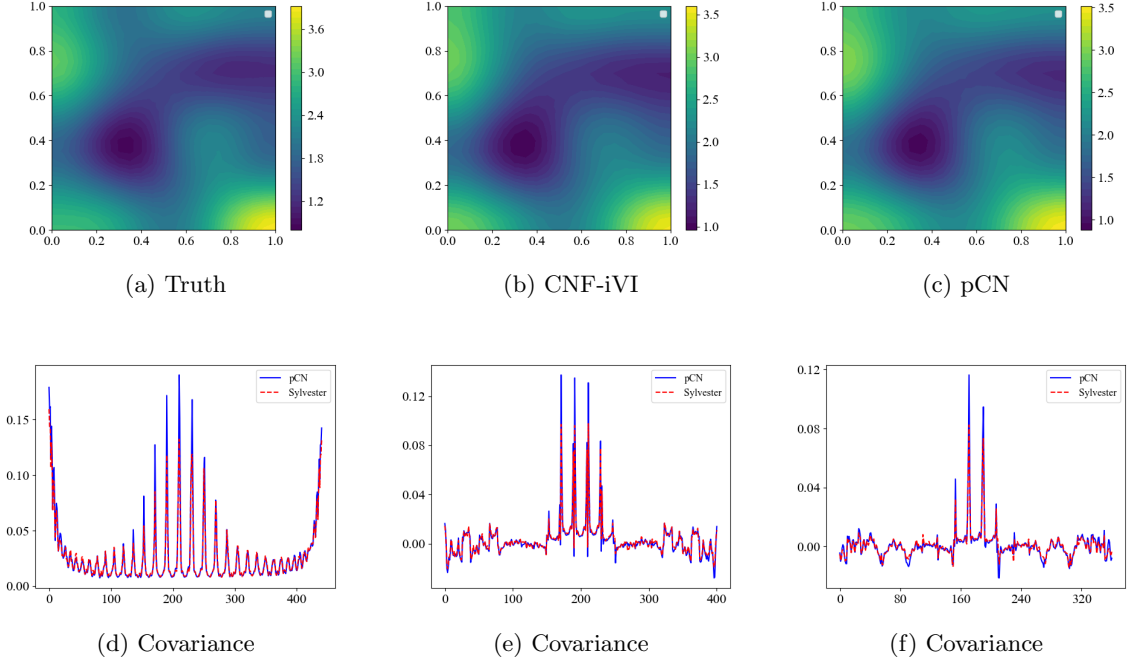


Figure 16: *The comparison of the approximate posterior obtained by retrained NF-iVI method and the pCN method. The estimated variance and covariance functions obtained by the pCN algorithm are drawn in blue solid line, and by retrained NF-iVI algorithm the red dashed line. (a): The background truth of u . (b): The mean of approximate posterior obtained by retrained NF-iVI method. (c): The mean of posterior obtained by pCN method. (d): The covariance function $c(x, y)$ on all the mesh point pairs $\{(x_i, x_i)\}_{i=1}^{N_g}$; (e): The covariance function $c(x, y)$ on the mesh points $\{(x_i, x_{i+40})\}_{i=1}^{N_g-40}$; (f): The covariance function $c(x, y)$ on the mesh points $\{(x_i, x_{i+80})\}_{i=1}^{N_g-80}$*

flow models using Algorithm 3. In subfigure (a) of Figures 15, 16, and 17, we present the true values. Subfigure (b) of Figures 15, 16, and 17 depict the mean values obtained by the pCN algorithm, while subfigure (c) of Figures 15, 16, and 17 show the mean values of the retrained models. Additionally, we conduct a detailed comparison of the covariance functions obtained by the two methods. We present the covariance function $c(x, y)$ on the mesh point pairs $\{(x_i, x_i)\}_{i=1}^{N_g}$, $\{(x_i, x_{i+40})\}_{i=1}^{N_g-40}$, $\{(x_i, x_{i+80})\}_{i=1}^{N_g-80}$ in subfigures (d), (e), and (f) of Figures 15, 16, and 17, respectively.

Furthermore, we provide numerical evidence to support the effectiveness of the retraining process. The re-simulation error of the retrained model is calculated as follows:

$$\begin{aligned}
\text{re-simulation error} &= E_{(\mathbf{x}, \mathbf{d})} (E_{\hat{\nu}_{(\mathbf{x}, \mathbf{d})}} \|\mathcal{S}\mathcal{G}(u) - \mathcal{S}\mathcal{G}(u_{truth}^{(\mathbf{x}, \mathbf{d})})\|) \\
&\approx \frac{1}{N_{train} N_{samples}} \sum_{i=1}^{N_{test}} \sum_{j=1}^{N_{samples}} \|\mathcal{S}\mathcal{G}(u_{ij}) - \mathcal{S}\mathcal{G}(u_{truth}^{(\mathbf{x}_i, \mathbf{d}_i)})\| \quad (5.2) \\
&= 0.02393,
\end{aligned}$$

where $u_{truth}^{(\mathbf{x}, \mathbf{d})}$ represents the ground truth and $\hat{\nu}_{(\mathbf{x}, \mathbf{d})}$ denotes the approximate posterior obtained

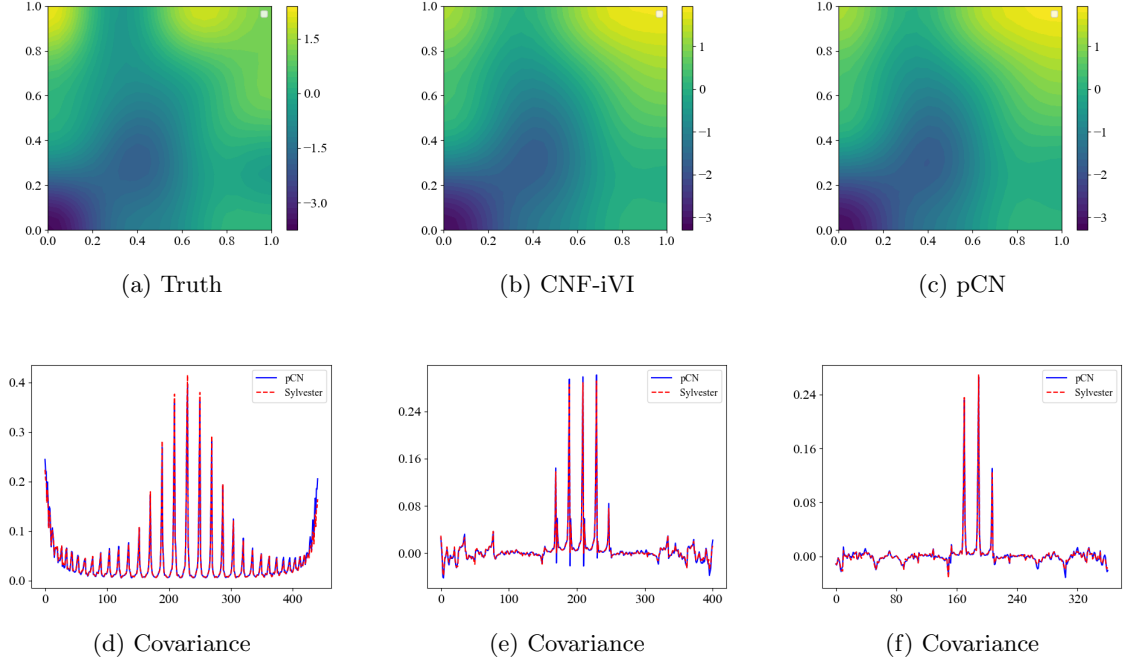


Figure 17: *The comparison of the approximate posterior obtained by retrained NF-iVI method and the pCN method. The estimated variance and covariance functions obtained by the pCN algorithm are drawn in blue solid line, and by retrained NF-iVI algorithm the red dashed line. (a): The background truth of u . (b): The mean of approximate posterior obtained by retrained NF-iVI method. (c): The mean of posterior obtained by pCN method. (d): The covariance function $c(x, y)$ on all the mesh point pairs $\{(x_i, x_i)\}_{i=1}^{N_g}$; (e): The covariance function $c(x, y)$ on the mesh points $\{(x_i, x_{i+40})\}_{i=1}^{N_g-40}$; (f): The covariance function $c(x, y)$ on the mesh points $\{(x_i, x_{i+80})\}_{i=1}^{N_g-80}$*

from the retrained flow models corresponding to the measurement information (\mathbf{x}, \mathbf{d}) . We set $N_{samples} = 500$ for the evaluation, similar to (5.1). This demonstrates a significant improvement compared to the re-simulation error obtained without retraining.

To numerically compare the covariance operator, we also compute the relative errors of the variance functions and the covariance functions between estimated posteriors generated by pCN algorithm and retrained NF-iVI method in Table 13. In the table, the notation \mathbf{c} means the total relative error, and the notation $\{c(x_i, x_{i+k})\}_{i=1}^{N_g-k}$ means the covariance function values on the pair of mesh points $\{(x_i, x_{i+k})\}_{i=1}^{N_g-k}$ ($k = 0, 40, 80$). The numbers below this notation are the relative errors between the vectors obtained by pCN method and retrained NF-iVI method for three different measurement information, respectively.

The visual evidence presented in Figures 15, 16, and 17, combined with the quantitative results from the re-simulation error in (5.2), demonstrates the effectiveness of Algorithm 3 in refining the posterior approximation obtained from conditional functional normalizing flow.

Table 13: *The relative errors between the covariance matrix, variance function, and covariance functions.*

Relative Error	\mathbf{c}	$\{c(x_i, x_i)\}_{i=1}^{N_g}$	$\{c(x_i, x_{i+40})\}_{i=1}^{N_g-40}$	$\{c(x_i, x_{i+80})\}_{i=1}^{N_g-80}$
Example1	0.0761	0.0565	0.0446	0.0923
Example2	0.0793	0.0334	0.0814	0.1239
Example3	0.0346	0.0054	0.0104	0.0081

6. Conclusion

In this paper, we introduce the NF-iVI and CNF-iVI methods within the infinite-dimensional space, providing an efficient computational framework for applying variational inference to inverse problems in function spaces. NF-iVI constructs a transformation that ensures measure equivalence while offering sufficient flexibility for the transformed measure. Building upon NF-iVI, CNF-iVI incorporates a conditional neural network to control the parameters of functional normalizing flow, significantly reducing computational costs.

The established NF-iVI and CNF-iVI approaches can be applied to PDE inverse problems with Gaussian priors, leading to explicit forms of the approximate posterior measure. We have successfully applied these methods to two inverse problems: the simple smooth equation and the steady-state Darcy flow problem. For all these inverse problems, NF-iVI provides an approximate posterior that closely resembles the ground truth generated by the pCN algorithm. While CNF-iVI may initially provides a rough estimate of the posterior, applying the adjusted Algorithm 3 can significantly improve its accuracy.

The current NF-iVI and CNF-iVI methods are based on transformations such as planar flow, Householder flow, Sylvester flow, and projected transformation flow. Future research could explore other types of neural networks that satisfy the general theorem proposed in infinite-dimensional space. For instance, in Euclidean spaces, the non-centered parameterisations formulation [36] has been employed as a transformation for normalizing flow. In this model, we could introduce different types of neural networks into each step of the transformation and carefully design each layer to enhance its complexity. Therefore, developing the NF-iVI method based on Non-centered parameterisations and combining it with other types of neural networks in function spaces, such as Fourier neural operators [33], is a promising avenue for future research.

7. Appendix

Since the parameter θ plays no explicit role in the discussion, we omit explicit reference to it. Consequently, we introduce the following abbreviations:

- The operator $f_{\theta_n}^{(n)}$ is simplified as $f^{(n)}$.
- The operator $\mathcal{F}_{\theta_n}^{(n)}$ is simplified as $\mathcal{F}^{(n)}$.
- The operator f_θ is simplified as f .

7.1. Functional Determinant

To obtain a precise expression for the Radon-Nikodym derivative between μ_f and μ_0 as discussed in Subsection 2.2, we will introduce the concept of the Fredholm-Carleman determinant. This determinant is applicable to operators of the form $I + \mathcal{K}$, where \mathcal{K} is a finite-dimensional operator mapping from a separable Hilbert space \mathcal{H}_u to itself, and I denotes the identity operator.

Definition 7.1. Let \mathcal{H}_u denotes a separable Hilbert space, and let \mathcal{K} be a finite-dimensional linear operator mapping from \mathcal{H}_u to \mathcal{H}_u , with its range being $\mathcal{K}(\mathcal{H}_u)$. We introduce the following notations:

$$\det_1(I + \mathcal{K}) = \det((I + \mathcal{K})|_{\mathcal{K}(\mathcal{H}_u)})$$

and

$$\det_2(I + \mathcal{K}) = \det((I + \mathcal{K})|_{\mathcal{K}(\mathcal{H}_u)}) \exp(-\text{trace}(\mathcal{K})),$$

where $(I + \mathcal{K})|_{\mathcal{K}(\mathcal{H}_u)}$ represents the matrix representation of the operator $I + \mathcal{K}$ restricted to the subspace $\mathcal{K}(\mathcal{H}_u)$.

We refer to $\det_1(I + \mathcal{K})$ as the Fredholm-Carleman determinant associated with the operator $I + \mathcal{K}$, and $\det_2(I + \mathcal{K})$ as the regularized Fredholm-Carleman determinant of the same operator. For further details, the reader is directed to Chapter 6.4 in the reference [7].

7.2. Proof of Theorem 2.3

Proof. The proof can be divided in two steps.

Step 1: Note that $f^{(n)} = I + \mathcal{F}^{(n)}$, we have

$$\begin{aligned} f^{(N)} \circ \dots \circ f^{(1)} &= (I + \mathcal{F}^{(N)}) \circ (I + \mathcal{F}^{(N-1)}) \circ \dots \circ (I + \mathcal{F}^{(1)}) \\ &= (I + \mathcal{F}^{(N-1)}) \circ \dots \circ (I + \mathcal{F}^{(1)}) + \mathcal{F}^{(N)} \circ (I + \mathcal{F}^{(N-1)}) \circ \dots \circ (I + \mathcal{F}^{(1)}) \\ &= I + \mathcal{F}^{(1)} + \mathcal{F}^{(2)} \circ (I + \mathcal{F}^{(1)}) + \mathcal{F}^{(3)} \circ (I + \mathcal{F}^{(2)}) \circ (I + \mathcal{F}^{(1)}) + \dots + \\ &\quad \mathcal{F}^{(N)} \circ (I + \mathcal{F}^{(N-1)}) \circ \dots \circ (I + \mathcal{F}^{(1)}) \\ &= I + \mathcal{T}, \end{aligned}$$

where $\mathcal{T} = \mathcal{F}^{(1)} + \mathcal{F}^{(2)} \circ (I + \mathcal{F}^{(1)}) + \mathcal{F}^{(3)} \circ (I + \mathcal{F}^{(2)}) \circ (I + \mathcal{F}^{(1)}) + \dots + \mathcal{F}^{(N)} \circ (I + \mathcal{F}^{(N-1)}) \circ \dots \circ (I + \mathcal{F}^{(1)})$. Since $\text{Im}(\mathcal{F}^{(n)}) \subset \mathcal{H}$, we have $\text{Im}(\mathcal{T}) \subset \mathcal{H}$.

Step 2: We can easily find that $I + \mathcal{T}$ is Fréchet differentiable and

$$\begin{aligned} D(I + \mathcal{T})(u) &= D(I + \mathcal{F}^{(N)}) \circ (I + \mathcal{F}^{(N-1)}) \circ \dots \circ (I + \mathcal{F}^{(1)})(u) \\ &= (I + D\mathcal{F}^{(N)})(u^{N-1}) \circ (I + D\mathcal{F}^{(N-1)})(u^{N-2}) \circ \dots \circ (I + D\mathcal{F}^{(1)})(u) \\ &= \Gamma^{(N)} \circ \Gamma^{(N-1)} \circ \dots \circ \Gamma^{(1)}. \end{aligned}$$

where $\Gamma^{(n)} = (I + D\mathcal{F}^{(n)})(u^{n-1})$, and $u^{n-1} = (I + \mathcal{F}^{(n-1)}) \circ \dots \circ (I + \mathcal{F}^{(1)})(u)$ for $n = 1, 2, \dots, N$. Since the point spectrum of $D\mathcal{F}^{(n)}(u)$ does not lie within the interval $(-\infty, -1]$ for all $u \in \mathcal{H}_u$, it follows that the mapping $\Gamma^{(n)}$ is injective for $n = 1, 2, \dots, N$ and $u \in \mathcal{H}_u$. Furthermore, since $D(I + \mathcal{T})(u) = \Gamma^{(N)} \circ \Gamma^{(N-1)} \circ \dots \circ \Gamma^{(1)}$, we conclude that $D(I + \mathcal{T})(u)$ is injective for all $u \in \mathcal{H}_u$.

Relying on Steps 1 and 2 and Example 10.27 of [8], we obtain that $\mu \sim \mu_0$ where $\mu = \mu_0 \circ (f^{(N)} \circ f^{(N-1)} \circ \dots \circ f^{(1)})^{-1}$. \square

7.3. Proof of Theorem 2.4

Proof. Firstly, we consider the case where $N = 1$, and regard $\mathcal{F}^{(1)}$ as \mathcal{F} . Let $\{e_1, e_2, \dots, e_M\}$ be a set of standard orthogonal bases of the space $\mathcal{F}(\mathcal{H}_u)$. From Theorems 5.8.3 and 6.6.7 and Corollary 6.6.8 of [7], we know that

$$\frac{d(\mu_0 \circ (I + \mathcal{F})^{-1})}{d\mu_0}((I + \mathcal{F})(u)) = \frac{1}{\Lambda_{\mathcal{F}}(u)},$$

where

$$\Lambda_{\mathcal{F}}(u) := \left| \det_2 (I + D\mathcal{F}(u)) \right| \exp \left[\delta\mathcal{F}(u) - \frac{1}{2} \|\mathcal{F}(u)\|_{\mathcal{H}}^2 \right],$$

and

$$\delta\mathcal{F}(u) = \text{trace} D\mathcal{F}(u) - \sum_{i=1}^M \widehat{e}_i(u) \mathcal{F}_i(u),$$

where for any $i \in \{1, 2, \dots, M\}$, $\mathcal{F}_i(u) = \langle \mathcal{F}(u), e_i \rangle_{\mathcal{H}}$, $\widehat{e}_i(u) = \langle u, e_i \rangle_{\mathcal{H}}$. By simplifying the calculation, we know that

$$\sum_{i=1}^M \widehat{e}_i(u) \mathcal{F}_i(u) = \left\langle \sum_{i=1}^M \widehat{e}_i(u) e_i, \sum_{i=1}^M \mathcal{F}_i(u) e_i \right\rangle_{\mathcal{H}} = \langle u, \mathcal{F}(u) \rangle_{\mathcal{H}}.$$

Hence, we obtain

$$\begin{aligned} \Lambda_{\mathcal{F}}(u) &= \left| \det_2 (I + D\mathcal{F}(u)) \right| \exp \left[\text{trace} D\mathcal{F}(u) - \frac{1}{2} \|\mathcal{F}(u)\|_{\mathcal{H}}^2 - \sum_{i=1}^M \widehat{e}_i(u) \mathcal{F}_i(u) \right] \\ &= \left| \det_2 (I + D\mathcal{F}(u)) \right| \exp \left[\text{trace} D\mathcal{F}(u) - \frac{1}{2} \|\mathcal{F}(u)\|_{\mathcal{H}}^2 - \langle u, \mathcal{F}(u) \rangle_{\mathcal{H}} \right] \\ &= \left| \det_1 (I + D\mathcal{F}(u)) \right| \exp \left[-\frac{1}{2} \|\mathcal{F}(u)\|_{\mathcal{H}}^2 - \langle u, \mathcal{F}(u) \rangle_{\mathcal{H}} \right]. \end{aligned}$$

Next, considering the case where $N \neq 1$, we denote $f = I + \mathcal{T}$ as in Subsection 7.2, and note that

$$\begin{aligned} Df(u) &= D(f_N \circ \dots \circ f_1)(u) \\ &= Df_N(f_{N-1} \circ \dots \circ f_1(u)) \circ Df_{N-1}(f_{N-2} \circ \dots \circ f_1(u)) \cdots \circ Df_1(u), \end{aligned}$$

we find that

$$\det_1(Df(u)) = \det_1(Df_N(u_{N-1})) \times \det_1(Df_{N-1}(u_{N-2})) \cdots \times \det_1(Df_1(u)),$$

where $u_k = f_k \circ \dots \circ f_1(u)$, $k = 1, 2, \dots, N-1$. Note that $\mathcal{T}(u) = f(u) - u$, from Corollary 6.6.8 of [7], we have

$$\begin{aligned} \frac{d\mu_0 \circ f^{-1}}{d\mu_0}(f(u)) &= \frac{1}{\Lambda_{\mathcal{T}}(u)} = \frac{1}{\left| \det_1 (I + D\mathcal{T}(u)) \right|} \exp \left[\frac{1}{2} \|\mathcal{T}(u)\|_{\mathcal{H}}^2 + \langle u, \mathcal{T}(u) \rangle_{\mathcal{H}} \right] \\ &= \prod_{k=1}^N \left| \det_1(Df_k(u_{k-1})) \right|^{-1} \exp \left(\frac{1}{2} \langle f(u) - u, f(u) - u \rangle_{\mathcal{H}} + \langle u, u - f(u) \rangle_{\mathcal{H}} \right). \end{aligned}$$

The proof of the theorem is completed. \square

7.4. Proof of Lemma 2.2

Proof. Since \mathcal{F} is compact and continuous, we obtain that f is a completely continuous field. Let us define

$$H(u, t) = t\mathcal{F}(u),$$

where $t \in [0, 1]$. For any bounded closed set \mathcal{M} in \mathcal{H}_u , we can conclude that

$$H : \mathcal{M} \times [0, 1] \rightarrow \mathcal{H}_u$$

is a compact continuous operator. Let us denote

$$h_t(u) = u + H(u, t),$$

it is straightforward to see that $h_0(u) = u$ and $h_1(u) = f(u)$.

For any $y \in \mathcal{H}_u$, let $\Omega = B(0, R) \subset \mathcal{H}_u$, where R is a large enough constant. Thus for any $q \in \partial\Omega$ and $t \in [0, 1]$, we have

$$\|h_t(q)\|_{\mathcal{H}_u} \geq \|q\|_{\mathcal{H}_u} - \|H(q, t)\|_{\mathcal{H}_u} > 0,$$

which ensures that $h_t(q) = q + H(q, t) \neq 0$. By the compact homotopy invariance of the Leray-Schauder degree [19], we obtain

$$\deg(f, \Omega, y) = \deg(I, \Omega, y) = 1.$$

Note that for any $u \in \mathcal{H}_u$, the eigenvalues of operator $Df(u)$ are strictly positive. By the definition of the Leray-Schauder degree, it is straightforward to know that

$$\sum_{z \in f^{-1}(y)} 1 = 1.$$

This implies that there is a unique point in $f^{-1}(y)$, and hence, the solution to $f(u) = y$ is unique within the ball $B(0, R)$. Given the arbitrary nature of R , we can conclude that f is a bijective mapping. \square

7.5. Proof of Theorems 2.7 and 2.8

Proof. To prove the theorem, it suffices to verify that the proposed method satisfies the four conditions outlined in Theorem 2.4. As functional planar flow is a special case of functional Sylvester flow, we will concentrate on the latter. We need to prove the corresponding operator

$$\mathcal{F}_{\theta_n}^{(n)}(u) = \mathcal{A}_n h(\mathcal{B}_n u + b_n)$$

satisfies the four conditions of Theorem 2.4, i.e.:

- The space $\text{Im}(\mathcal{F}_{\theta_n}^{(n)}) \subset \mathcal{H}$, where $\text{Im}(\mathcal{F}_{\theta_n}^{(n)})$ denotes the image of $\mathcal{F}_{\theta_n}^{(n)}$.
- The operator $\mathcal{F}_{\theta_n}^{(n)}$ is a finite rank operator.
- The operator $f_{\theta_n}^{(n)}$ is bijective.
- For any $u \in \mathcal{H}_u$, all point spectrum of $D\mathcal{F}_{\theta_n}^{(n)}(u)$ are not in $(-\infty, -1]$.

Since \mathcal{A}_n satisfies $\text{Im}(\mathcal{A}_n) \subset \mathcal{H}$, we know that $\mathcal{F}_{\theta_n}^{(n)} \subset \mathcal{H}$. At the same time, since the domain $D(\mathcal{A}_n)$ of operator \mathcal{A}_n has finite dimensions and \mathcal{A}_n is a linear operator, we can conclude that $\text{Im}(\mathcal{A}_n)$ has finite dimensions, which means that $\mathcal{F}_{\theta_n}^{(n)}$ is a finite rank operator. The above discussion verifies the first two conditions required by Theorem 2.4.

Because \mathcal{A}_n is a finite rank linear operator, it must be a bounded operator. Note that $h(x) = \tanh(x) \subset (-1, 1)$, so $h(\mathcal{B}_n u + b_n)$ is bounded in \mathbb{R}^M for any $u \in \mathcal{H}_u$. Consequently, $\mathcal{A}_n h(\mathcal{B}_n u + b_n)$ is bounded in \mathcal{H}_u , implies that the range of \mathcal{F}_n is bounded in \mathcal{H}_u . By Lemma 2.2, we know that $I + \mathcal{F}_{\theta_n}^{(n)}$ is bijective. This verifies the third condition required by Theorem 2.4.

Finally, we are able to determine that

$$D\mathcal{F}_{\theta_n}^{(n)}(u) = \mathcal{A}_n Dh(\mathcal{B}_n u + b_n)\mathcal{B}_n = \mathcal{A}_n \text{diag}(h'(\mathcal{B}_n u + b_n))\mathcal{B}_n,$$

and $\mathcal{A}_n \text{diag}(h'(\mathcal{B}_n u + b_n))\mathcal{B}_n$ has the same point spectrum with $\text{diag}(h'(\mathcal{B}_n u + b_n))\mathcal{B}_n \mathcal{A}_n$ (see Theorem 2.9 for details). Furthermore, we recognize that $\text{diag}(h'(\mathcal{B}_n u + b_n))$ is a diagonal matrix with diagonal elements within the interval $(0, 1)$. Therefore, combined with the conditions that the eigenvalues of $\mathcal{B}_n \mathcal{A}_n$ are not in $(-\infty, 1]$, we find that the eigenvalues of $\text{diag}(h'(\mathcal{B}_n u + b_n))\mathcal{B}_n \mathcal{A}_n$ are not in $(-\infty, 1]$, so the point spectrum of $\mathcal{A}_n \text{diag}(h'(\mathcal{B}_n u + b_n))\mathcal{B}_n$ is not in $(-\infty, 1]$. Thus, we have verified the final condition required by Theorem 2.4.

In conclusion, $\mathcal{F}_{\theta_n}^{(n)}(u) = \mathcal{A}_n h(\mathcal{B}_n u + b_n)$ satisfies all the conditions of Theorem 2.4, which completes the proof. \square

7.6. Proof of Theorems 2.5 and 2.6

Proof. To prove the theorem, it suffices to verify that the proposed method satisfies the four conditions of Theorem 2.4. As functional Householder flow is a special case of functional projected transformation flow, we will focus on the latter. We need to prove that the corresponding operator

$$\mathcal{F}_{\theta_n}^{(n)}(u) = \mathcal{Q}R_n(\mathcal{P}u + b_n)$$

satisfies the four conditions of Theorem 2.4. Similar to the approach used in Subsection 7.5, we are able to prove the first two conditions for functional projected transformation flow. The details are omitted here for brevity.

For the third condition, note that

$$D\mathcal{F}_{\theta_n}^{(n)}(u) = \mathcal{Q}R_n\mathcal{P},$$

and the operator $\mathcal{Q}R_n\mathcal{P}$ has the same eigenvalues with the matrix R_n , the point spectrum of $D\mathcal{F}_{\theta_n}^{(n)}(u)$ is not in $(-\infty, 1]$. Finally, Lemma 2.1 implies that $I + \mathcal{F}_{\theta_n}^{(n)}$ is invertible. Based on the above discussion, we can conclude that $\mathcal{F}_{\theta_n}^{(n)}(u) = \mathcal{Q}R_n(\mathcal{P}u + b_n)$ satisfies the conditions of Theorem 2.4, which completes the proof of the theorem. \square

7.7. Proof of Theorem 2.9

Proof. Note that both \mathcal{A} and \mathcal{B} are linear operators, and

$$\mathcal{B} : \mathcal{H}_u \rightarrow \mathbb{R}^M, \quad \mathcal{A} : \mathbb{R}^M \rightarrow \mathcal{H}_u.$$

Without losing generality, \mathcal{B} and \mathcal{A} can be written as

$$\mathcal{B}v = (\langle \phi_1, v \rangle_{\mathcal{H}_u}, \langle \phi_2, v \rangle_{\mathcal{H}_u}, \dots, \langle \phi_M, v \rangle_{\mathcal{H}_u})^T,$$

where $\phi_1, \phi_2, \dots, \phi_M \in \mathcal{H}_u$, and

$$\mathcal{A}d = d_1\psi_1 + d_2\psi_2 + \dots + d_M\psi_M,$$

where $\psi_1, \psi_2, \dots, \psi_M \in \mathcal{H}_u$ are mutually orthogonal.

Let λ be the point spectrum of $\mathcal{A}\mathcal{B}$, and v_λ be its corresponding eigenfunction. We have $\mathcal{A}\mathcal{B}v_\lambda = \lambda v_\lambda$. Obviously, since $\text{Im}(\mathcal{A}_n) \subset \text{span}\{\psi_1, \psi_2, \dots, \psi_M\}$, let $v_\lambda = \sum_{i=1}^M \alpha_i \psi_i$, then for any eigenpair (λ, v_λ) , we have

$$\sum_{k=1}^M \sum_{i=1}^M \langle \phi_k, \psi_i \rangle \alpha_i \psi_k = \lambda \sum_{i=1}^M \alpha_i \psi_i.$$

Hence, for any $r = 1, 2, \dots, M$, we obtain

$$\sum_{i=1}^M \langle \phi_r, \psi_i \rangle \alpha_i = \lambda \alpha_r. \quad (7.1)$$

Equality (7.1) can be expressed as

$$\begin{pmatrix} \langle \phi_1, \psi_1 \rangle & \cdots & \langle \phi_M, \psi_1 \rangle \\ \vdots & \ddots & \vdots \\ \langle \phi_1, \psi_M \rangle & \cdots & \langle \phi_M, \psi_M \rangle \end{pmatrix} \begin{pmatrix} \alpha_1 \\ \vdots \\ \alpha_M \end{pmatrix} = \lambda \begin{pmatrix} \alpha_1 \\ \vdots \\ \alpha_M \end{pmatrix},$$

which is just the equation $\mathcal{B}\mathcal{A}\alpha = \lambda\alpha$ with $\alpha = (\alpha_1, \alpha_2, \dots, \alpha_M)^T$. Therefore, the point spectrum of $\mathcal{A}\mathcal{B}$ is one-to-one correspondence with the eigenvalues of $\mathcal{B}\mathcal{A}$, which finishes the proof. \square

7.8. Proof of Theorem 2.10

Proof. For clarity, we show the discretization invariant when $\mathcal{H}_u = L^2(D)$. The proof can be easily adapted to other settings, e.g., $\mathcal{H}_u = H^s(D)$ with $s \geq 0$. We have

$$\mathcal{F}_{\theta_n}^{(n)} : \mathcal{H}_u \rightarrow \mathcal{H}_u,$$

and $\mathcal{F}_{\theta_n}^{(n)}$ has four different styles:

- Functional planar flow

$$\mathcal{F}_{\theta_n}^{(n)}(u) = u_n h(\langle w_n, u_n \rangle_{\mathcal{H}_u} + b_n).$$

- Functional Householder flow

$$\mathcal{F}_{\theta_n}^{(n)}(u) = -0.5v_n(\langle v_n, u \rangle_{\mathcal{H}_u} + b_n).$$

- Functional Sylvester flow

$$\mathcal{F}_{\theta_n}^{(n)}(u) = \mathcal{A}_n h(\mathcal{B}_n u + b_n).$$

- Functional projected transformation flow

$$\mathcal{F}_{\theta_n}^{(n)}(u) = \mathcal{Q}R_n(\mathcal{P}u + b_n).$$

It is worth noting that functional planar flow and functional Householder flow are special cases of functional Sylvester flow and functional projected transformation flow, respectively. So we only need to prove the discrete invariance of only the latter two flows.

Let K be a compact subset of $C(D)$, and $\{D_j\}_{j=1}^{\infty}$ a sequence of discrete refinements of D . To each discretization D_j associate partition $P_j^{(1)}, \dots, P_j^{(j)} \subset D$, each contains a single, unique point of D_j , each has positive Lebesgue measure, and

$$\bigcup_{k=1}^j P_j^{(k)} = D.$$

To establish the discretization invariance of the functional Sylvester flow, we aim to demonstrate the following: for any $\epsilon > 0$ and any $a \in K$, there exists an integer $L > 0$ (independent of a) such that for all $m > L$, the inequality

$$\|\mathcal{A}_n h(\mathcal{B}_n a + b_n) - \mathcal{A}_n h(\mathcal{B}_n^{(m)} a_{(m)}(x) + b_n)\|_{\mathcal{H}_u} < \epsilon$$

holds. Here, $a_{(m)}(x) = (a(x_1), \dots, a(x_m))$, and $\mathcal{B}_n^{(m)} a_{(m)}(x)$ is defined as

$$\mathcal{B}_n^{(m)} a_{(m)}(x) = R_{\mathcal{B}}^n \begin{pmatrix} \sum_{i=1}^m a(x_i) \phi_1(x_i) |P_j^{(i)}| \\ \vdots \\ \sum_{i=1}^m a(x_i) \phi_M(x_i) |P_j^{(i)}| \end{pmatrix}.$$

Note that \mathcal{A}_n is a bounded linear operator and $h(x)$ is a continuous function, the the only thing we need to prove is that for any $a \in K$ and $m > L$, we have

$$\|\mathcal{B}_n a - \mathcal{B}_n^{(m)} a_{(m)}\|_{\mathbb{R}^M} < \epsilon,$$

which equals to

$$\left| \sum_{i=1}^m a(x_i) \phi_r(x_i) |P_j^{(i)}| - \langle a, \phi_r \rangle_{\mathcal{H}_u} \right| < \epsilon,$$

for all $r = 1, \dots, M$. We will provide a proof of this claim at the end of the proof.

Similarly, to establish the discretization invariance of the functional projected transformation flow, we aim to demonstrate the following: for any $\epsilon > 0$ and any $a \in K$, there exists an integer $L > 0$ (independent of a) such that for all $m > L$, the inequality

$$\|\mathcal{Q} R_n \mathcal{P} a - \mathcal{Q} R_n \mathcal{P}_{(m)} a_{(m)}\|_{\mathcal{H}_u} < \epsilon$$

holds. Here, $a_{(m)}(x) = (a(x_1), \dots, a(x_m))$, and $\mathcal{P}_{(m)} a_{(m)}(x)$ is defined as

$$\mathcal{P}_{(m)} a_{(m)}(x) = \begin{pmatrix} \sum_{i=1}^m a(x_i) \phi_1(x_i) |P_j^{(i)}| \\ \vdots \\ \sum_{i=1}^m a(x_i) \phi_M(x_i) |P_j^{(i)}| \end{pmatrix}.$$

Note that \mathcal{Q} and R_n are both bounded linear operators, what we need to prove is that

$$\|\mathcal{P} a - \mathcal{P}_{(m)} a_{(m)}\|_{\mathbb{R}^N} < \epsilon.$$

To prove the desired result, it suffices to show that

$$\left| \sum_{i=1}^m a(x_i) \phi_r(x_i) \left| P_j^{(i)} \right| - \langle a, \phi_r \rangle_{\mathcal{H}_u} \right| < \epsilon$$

for all $r = 1, \dots, M$.

Thus, combining the proofs for the linear and nonlinear cases, the key of the theorem is to prove that for any $a \in K$, there exists an integer $L > 0$ independent of a , such that when $m > L$, we have

$$\left| \sum_{i=1}^m a(x_i) \phi_r(x_i) \left| P_j^{(i)} \right| - \langle a, \phi_r \rangle_{\mathcal{H}_u} \right| < \epsilon,$$

for all $r = 1, \dots, M$.

Note that $K \subset C(D)$ is compact, we can find $a_1, \dots, a_W \in K$ such that for any $a \in K$, there exists $w \in \{1, \dots, W\}$ satisfying

$$\|a - a_w\|_{C(D)} < \frac{\epsilon}{3|D| \sup_{r,i} |\phi_r(x_i)|}.$$

Since D_j is a discrete refinement, by convergence of the Riemann sum, for each $w = 1, \dots, W$, there exists a positive constant $p_w > 0$ such that when $t_w > p_w$, we have

$$\left| \sum_{i=1}^{t_w} a_w(x_i) \phi_r(x_i) \left| P_j^{(i)} \right| - \langle a_w, \phi_r \rangle_{\mathcal{H}_u} \right| < \frac{\epsilon}{3},$$

for all $r = 1, \dots, M$.

Note that $a, a_w \in K$ are all continuous function, we have

$$\left| \sum_{i=1}^{t_w} a_w(x_i) \phi_r(x_i) \left| P_j^{(i)} \right| - \sum_{i=1}^{t_w} a(x_i) \phi_r(x_i) \left| P_j^{(i)} \right| \right| < \|a - a_w\|_{C(D)} |D| \sup_{r,i} |\phi_r(x_i)| < \frac{\epsilon}{3}.$$

Now, let $L \geq \max\{p_1, \dots, p_W, p\}$. Then, for any $m > L$, we obtain

$$\begin{aligned} \left| \sum_{i=1}^m a(x_i) \phi_r(x_i) \left| P_j^{(i)} \right| - \langle a, \phi_r \rangle_{\mathcal{H}_u} \right| &\leq \left| \sum_{i=1}^m a(x_i) \phi_r(x_i) \left| P_j^{(i)} \right| - \sum_{i=1}^m a_w(x_i) \phi_r(x_i) \left| P_j^{(i)} \right| \right| \\ &\quad + \left| \sum_{i=1}^m a_w(x_i) \phi_r(x_i) \left| P_j^{(i)} \right| - \langle a_w, \phi_r \rangle_{\mathcal{H}_u} \right| \\ &\quad + |\langle a, \phi_r \rangle_{\mathcal{H}_u} - \langle a_w, \phi_r \rangle_{\mathcal{H}_u}| \\ &< \epsilon, \end{aligned}$$

which completes the proof. \square

References

- [1] S. Agapiou, O. Papaspiliopoulos, D. Sanz-Alonso, and A. M. Stuart, *Importance sampling: intrinsic dimension and computational cost*, Statist. Sci. **32** (2017), no. 3, 405–431. MR 3696003
- [2] Martin Benning and Martin Burger, *Modern regularization methods for inverse problems*, Acta Numer. **27** (2018), 1–111. MR 3826506

- [3] Alexandros Beskos, Mark Girolami, Shiwei Lan, Patrick E. Farrell, and Andrew M. Stuart, *Geometric MCMC for infinite-dimensional inverse problems*, J. Comput. Phys. **335** (2017), 327–351. MR 3612501
- [4] Alexandros Beskos, Ajay Jasra, Ege A. Muzaffer, and Andrew M. Stuart, *Sequential Monte Carlo methods for Bayesian elliptic inverse problems*, Stat. Comput. **25** (2015), no. 4, 727–737. MR 3360488
- [5] Christopher M. Bishop, *Pattern Recognition and Machine Learning*, Information Science and Statistics, Springer, New York, 2006. MR 2247587
- [6] David M. Blei, Alp Kucukelbir, and Jon D. McAuliffe, *Variational inference: a review for statisticians*, J. Amer. Statist. Assoc. **112** (2017), no. 518, 859–877. MR 3671776
- [7] Vladimir I. Bogachev, *Gaussian Measures*, American Mathematical Society, Providence, RI, 1998. MR 1642391
- [8] ———, *Differentiable Measures and the Malliavin Calculus*, Mathematical Surveys and Monographs, American Mathematical Society, Providence, RI, 2010. MR 2663405
- [9] Tan Bui-Thanh, Omar Ghattas, James Martin, and Georg Stadler, *A computational framework for infinite-dimensional Bayesian inverse problems Part I: The linearized case, with application to global seismic inversion*, SIAM J. Sci. Comput. **35** (2013), no. 6, A2494–A2523. MR 3126997
- [10] Tan Bui-Thanh and Quoc P. Nguyen, *FEM-based discretization-invariant MCMC methods for PDE-constrained Bayesian inverse problems*, Inverse Probl. Imaging **10** (2016), no. 4, 943–975. MR 3610747
- [11] Daniela Calvetti, Matthew Dunlop, Erkki Somersalo, and Andrew Stuart, *Iterative updating of model error for Bayesian inversion*, Inverse Problems **34** (2018), no. 2, 025008, 38. MR 3751052
- [12] Daniela Calvetti and Erkki Somersalo, *Bayesian Scientific Computing*, Springer, Cham, 2023. MR 4628023
- [13] Peng Chen and Omar Ghattas, *Stein variational reduced basis Bayesian inversion*, SIAM J. Sci. Comput. **43** (2021), no. 2, A1163–A1193. MR 4235177
- [14] Simon L. Cotter, Masoumeh Dashti, James C. Robinson, and Andrew M. Stuart, *Bayesian inverse problems for functions and applications to fluid mechanics*, Inverse Problems **25** (2009), no. 11, 115008, 43. MR 2558668
- [15] Simon L. Cotter, Gareth O. Roberts, Andrew M. Stuart, and David White, *MCMC methods for functions: modifying old algorithms to make them faster*, Statist. Sci. **28** (2013), no. 3, 424–446. MR 3135540
- [16] Masoumeh Dashti, Stephen Harris, and Andrew Stuart, *Besov priors for Bayesian inverse problems*, Inverse Probl. Imaging **6** (2012), no. 2, 183–200. MR 2942737
- [17] Masoumeh Dashti and Andrew M. Stuart, *The Bayesian approach to inverse problems*, Handbook of uncertainty quantification. Vol. 1, 2, 3, Springer, Cham, 2017, pp. 311–428. MR 3839555
- [18] Laurent Dinh, Jascha Sohl-Dickstein, and Samy Bengio, *Density estimation using Real NVP*, International Conference on Learning Representations, 2017.
- [19] Andrzej Granas and James Dugundji, *Fixed point theory*, Springer Monographs in Mathematics, Springer-Verlag, New York, 2003.
- [20] Nilabja Guha, Xiaqing Wu, Yalchin Efendiev, Bangti Jin, and Bani K. Mallick, *A variational Bayesian approach for inverse problems with skew-t error distributions*, J. Comput. Phys. **301** (2015), 377–393. MR 3402736
- [21] Junxiong Jia, Peijun Li, and Deyu Meng, *Stein variational gradient descent on infinite-dimensional space and applications to statistical inverse problems*, SIAM J. Numer. Anal. **60** (2022), no. 4, 2225–2252. MR 4469515
- [22] Junxiong Jia, Jigen Peng, and Jinghuai Gao, *Posterior contraction for empirical Bayesian approach to inverse problems under non-diagonal assumption*, Inverse Probl. Imaging **15** (2021), no. 2, 201–228. MR 4214068
- [23] Junxiong Jia, Yanni Wu, Peijun Li, and Deyu Meng, *Variational inverting network for statistical inverse problems of partial differential equations*, J. Mach. Learn. Res. **24** (2023), paper no. 201, 60. MR 4633590
- [24] Junxiong Jia, Qian Zhao, Zongben Xu, Deyu Meng, and Yee Leung, *Variational Bayes’ method for functions with applications to some inverse problems*, SIAM J. Sci. Comput. **43** (2021), no. 1, A355–A383. MR 4205093
- [25] Bangti Jin, *A variational Bayesian method to inverse problems with impulsive noise*, J. Comput. Phys. **231** (2012), no. 2, 423–435. MR 2872083
- [26] Bangti Jin and Jun Zou, *Hierarchical Bayesian inference for ill-posed problems via variational method*, J. Comput. Phys. **229** (2010), no. 19, 7317–7343. MR 2677781
- [27] Jari Kaipio and Erkki Somersalo, *Statistical and Computational Inverse Problems*, Applied Mathematical Sciences, Springer-Verlag, New York, 2005. MR 2102218
- [28] Andreas Kirsch, *An Introduction to the Mathematical Theory of Inverse Problems*, second ed., Applied Mathematical Sciences, Springer, New York, 2011. MR 3025302
- [29] Nikola Kovachki, Zongyi Li, Burigede Liu, Kamyar Azizzadenesheli, Kaushik Bhattacharya, Andrew Stuart, and Anima Anandkumar, *Neural operator: learning maps between function spaces with applications to PDEs*, J. Mach. Learn. Res. **24** (2023), paper no. 89, 97. MR 4582511
- [30] Alp Kucukelbir, Dustin Tran, Rajesh Ranganath, Andrew Gelman, and David M. Blei, *Automatic differentiation variational inference*, J. Mach. Learn. Res. **18** (2017), paper no. 14, 45. MR 3634881

- [31] Harold J. Kushner and G. George Yin, *Stochastic Approximation Algorithms and Applications*, Applications of Mathematics, Springer-Verlag, New York, 1997. MR 1453116
- [32] Matti Lassas and Samuli Siltanen, *Can one use total variation prior for edge-preserving Bayesian inversion?*, *Inverse Problems* **20** (2004), no. 5, 1537–1563. MR 2109134
- [33] Zongyi Li, Nikola Kovachki, Kamyar Azizzadenesheli, Burigede Liu, Kaushik Bhattacharya, Andrew Stuart, and Anima Anandkumar, *Fourier neural operator for parametric partial differential equations*, International Conference on Learning Representations, 2021.
- [34] Wenyuan Liao and Ou Wei, *A fourth-order compact numerical scheme for three-dimensional acoustic wave equation with variable velocity*, Recent advances in mathematical and statistical methods, Springer Proc. Math. Stat., Springer, Cham, 2018, pp. 279–289. MR 3879571
- [35] GuoJun Liu, Yang Liu, MaoZu Guo, Peng Li, and MingYu Li, *Variational inference with gaussian mixture model and householder flow*, *Neural Networks* **109** (2019), 43–55.
- [36] Omiros Papaspiliopoulos, Gareth O. Roberts, and Martin Sköld, *Non-Centered Parameterizations for Hierarchical Models and Data Augmentation*, Bayesian statistics, 7, Oxford Univ. Press, New York, 2003, pp. 307–326. MR 2003180
- [37] Natesh S. Pillai, Andrew M. Stuart, and Alexandre H. Thiéry, *Noisy gradient flow from a random walk in Hilbert space*, *Stoch. Partial Differ. Equ. Anal. Comput.* **2** (2014), no. 2, 196–232. MR 3249584
- [38] Frederick J. Pinski, Geoffrey Simpson, Andrew M. Stuart, and Harald Weber, *Algorithms for Kullback-Leibler approximation of probability measures in infinite dimensions*, *SIAM J. Sci. Comput.* **37** (2015), no. 6, A2733–A2757. MR 3424069
- [39] Frederick J. Pinski, Geoffrey Simpson, Andrew M. Stuart., and Harald Weber, *Kullback-Leibler approximation for probability measures on infinite dimensional spaces*, *SIAM J. Math. Anal.* **47** (2015), no. 6, 4091–4122. MR 3419882
- [40] Danilo Jimenez Rezende and Shakir Mohamed, *Variational inference with normalizing flows*, International Conference on Machine Learning **37** (2015), 1550–1558.
- [41] Herbert Robbins and Sutton Monro, *A stochastic approximation method*, *Ann. Math. Statistics* **22** (1951), 400–407. MR 42668
- [42] Christian P. Robert and George Casella, *Monte Carlo Statistical Methods*, Springer-Verlag, New York, 1999. MR 1707311
- [43] Daniel Rudolf and Björn Sprungk, *On a generalization of the preconditioned Crank-Nicolson metropolis algorithm*, *Found. Comput. Math.* **18** (2018), no. 2, 309–343. MR 3777781
- [44] Jiaming Sui and Junxiong Jia, *Non-centered parametric variational Bayes’ approach for hierarchical inverse problems of partial differential equations*, *Math. Comp.* **93** (2024), no. 348, 1715–1760. MR 4730247
- [45] Jakub M Tomczak and Max Welling, *Improving variational auto-encoders using householder flow*, *IEEE Transactions on Image Processing* **29** (2020), 2487–2499.
- [46] Rianne Van Den Berg, Leonard Hasenclever, Jakub M Tomczak, and Max Welling, *Sylvester normalizing flows for variational inference*, 34th Conference on Uncertainty in Artificial Intelligence, 2018, pp. 393–402.
- [47] Arthur B. Weglein, Fernanda V. Araújo, Paulo M. Carvalho, Robert H. Stolt, Kenneth H. Matson, Richard T. Coates, Dennis Corrigan, Douglas J. Foster, Simon A. Shaw, and Haiyan Zhang, *Inverse scattering series and seismic exploration*, *Inverse Problems* **19** (2003), no. 6, R27–R83. MR 2036527
- [48] Max Welling and Yee Whye Teh, *Bayesian learning via stochastic gradient langevin dynamics*, Proceedings of the 28th International Conference on Machine Learning, 2011, pp. 681–688.
- [49] Cheng Zhang, Judith Bütepage, Hedvig Kjellström, and Stephan Mandt, *Advances in variational inference*, *IEEE Trans. Pattern Analysis and Machine Intelligence* **41** (2018), no. 8, 2008–2026.
- [50] Qingping Zhou, Tengchao Yu, Xiaoqun Zhang, and Jinglai Li, *Bayesian inference and uncertainty quantification for medical image reconstruction with Poisson data*, *SIAM J. Imaging Sci.* **13** (2020), no. 1, 29–52. MR 4048008